CLASSICAL DYNAMICS STUDIES OF CONFORMATIONAL CHANGES IN POLYATOMIC MOLECULES IN THE GAS AND CONDENSED PHASES

By

ERIC PAUL-JOSEPH WALLIS

Bachelor of Science

Arkansas Tech University

Russellville, Arkansas

1987

Submitted to the Faculty of the
Graduate College of the
Oklahoma State University
in partial fulfillment of
the requirements for
the Degree of
DOCTOR OF PHILOSOPHY
May, 1992

CLASSICAL DYNAMICS STUDIES OF CONFORMATIONAL CHANGES IN POLYATOMIC MOLECULES IN THE GAS AND CONDENSED PHASES

Thesis approved:

Donald L. Thompson
Thesis Adviser

Lionel M. Raff

J. Paul Devlin

Richard C. Brasell

Thomas C. Collins
Dean of the Graduate College

To my mom

ACKNOWLEDGEMENT

I would like to thank my wife, Jill, for her support and understanding throughout my graduate career and during the time that my thesis was written. Jill, your cheerfulness and bright outlook during this stressful period helped make the long nights of work bearable. I would like to thank both of my families for their support. that was given to both Jill and myself during my graduate career.

My deep appreciation is extended to Tommy Sewell. After the first week in June of 1987, would you have thought things would have turned out like they have? I will never forget the pizza late at night as we frantically completed our homework, the "soft mellow" (Pink Floyd) tunes emanating from your stereo speakers, and the lunches and walks that we took and argued scientific ideas (and sometimes just augured)! It has been a memorable four years.

I would like to thank my friend Nick Morris for the late night coffee breaks at "Shortys". The long talks and great company will always be remembered. I would also like to thank the rest of my friends Tim, Qin, Karen, Dave, Jim, Candee, and Marty for making my graduate experience memorable.

I would like to thank my adviser Dr. Donald L. Thompson and my committee members Drs. J. Paul Devlin, Lionel M. Raff and R. Powell for taking the time to read this thesis and for their helpful comments.

Many thanks must be given to the Oklahoma State University Computer Center; specifically, J. Albert, Dan Carlile, and James Alexander for the generous allocation of computer time on the IBM3090 and Konrad Brandemuhl and Lorraine Goff for helping with the everyday problems of running on the IBM.

This work was supported by the U.S. Army Research Office. I would like to acknowledge the use of the Cray X-MP/48 at the Ballistics Research Laboratory for some of the calculations. I would like to thank Phillips Petroleum Co. for sponsoring a fellowship which supported some of my research.

TABLE OF CONTENTS

Chapter Page

LIST OF TABLES

LIST OF FIGURES

CHAPTER I

INTRODUCTION

The work presented in this thesis addresses conformational dynamics of polyatomic molecules in the gas and condensed phases. The two systems that we have chosen for study are hexahydro-1,3,5-trinitro-1,3,5-triazine (RDX) and nitrous acid (HONO). RDX is a cyclical nitramine used as a component in solid rocket fuels.

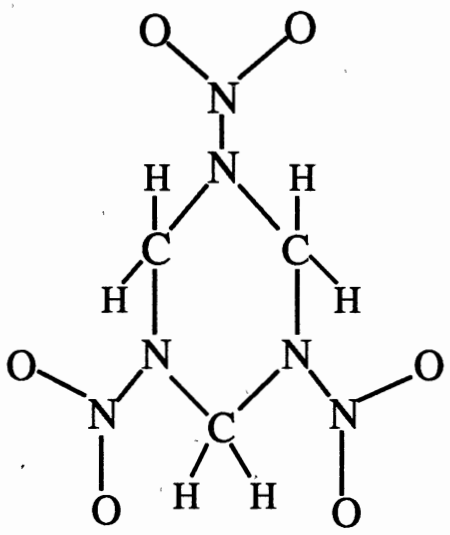

It can undergo both ring inversion and pseudorotations (for a more detailed discussion, see chapter II). Due to the low vapor pressure and inherent instability of RDX, little is know about it either experimentally or theoretically on a molecular level. HONO is one of the simplest molecules to undergo *cis—trans* isomerizations. It has been studied extensively both experimentally and theoretically so much is known about the potential-energy surface (for a more detailed discussion, see chapter II).

Molecular dynamics simulation methods[1-5] were employed in the studies presented here. Molecular dynamics simulations use classical mechanics to calculate trajectories by numerically solving Hamilton's equations of motion. Equilibrium properties of the system such as energy differences between local minima, conformational distributions, and average structures can be calculated. These properties combined with experimental data yield free-energies, enthalpies, and entropies. Also, dynamical processes such as flexibility of molecules about their minimum energy structures and rate constants for transitions between local minima can be obtained. Thus, molecular dynamics simulation methods can be used to develop and test potential-energy surfaces and also calculate properties of a system which cannot be measured using current experimental techniques.

Molecular dynamics simulations have been employed in the studies of equilibrium properties of simple liquids[6-8], macromolecules in the gas and condensed phases[9-26], and polymers in the solution and crystal phases[27-32] with much success. The effects of a solvent on activated processes, such as barrier crossing, have received much less attention. The study of activated processes in condensed phase is more computationally demanding since the reactant and products are separated by a potential-energy barrier. Few events occur in a reasonable amount of computer time for barrier much larger the κT, where κ is the Boltzmann constant and T is the temperature. With the aid of faster computers, barrier crossing processes are more tractable.

The importance of reactions in solution is fundamental to chemistry. Studies of simple chemical reactions such as, $A+BC \rightarrow AB+C$[33-36], S_n1 and S_n2[37], and intramolecular proton transfer[38], employing molecular dynamics simulations have helped elucidate the effects of the solvent on the rate of reaction. These studies have shown that for barriers in the range of 10-20 kcal mol^{-1}, a "frozen solvent" picture emerges, that is, once the molecule ascends the barrier, it undergoes almost free passage through the barrier region; the molecule spends a short time in the barrier region. For low barriers, (< 10 kcal mol^{-1}) a breakdown in the "frozen solvent" picture is observed due to the increased time that the

reacting molecule spends in the barrier region. The frequent collisions of the solvent with the reacting molecule can significantly retard the barrier crossing process.

Molecules which undergo isomerization processes comprise an interesting class of compounds. Since isomerizations usually involve low barriers between neighboring isomers, solvent effects can play an important role in the dynamics. Also, the problem of conformational dynamics readily lends itself to molecular dynamics simulations since periodic potential-energy functions are usually employed to describe the transition between the reactant and product states. The equilibrium and rate constant data for both the forward and reverse processes can be obtained from a single long trajectory.

To date, most studies of isomerization processes have been performed using model potential-energy surfaces which constrain the motions of the bonds and angles[32,39-42] or treat the reaction coordinate as a one-dimension oscillator[43-44]. Recent studies have suggested that internal flexibility can alter the barrier crossing process by modifying local modes[45-48]. With the advent of faster computers, studies of molecular systems employing more accurate potential-energy surfaces are needed for a more realistic comparison between theory and experiment.

Format of the Thesis

A review of the literature on the two molecules in this study and other studies relevant to the work performed in this thesis are reviewed in Chapter II and Chapter III. A brief introduction to the methods and theories is presented in Chapter IV. The details of the potential-energy surfaces employed and the computational methods employed in these calculations are presented in Chapter V. In Chapters VI-VIII, studies of the conformational dynamics and chair→boat/twist ring inversion of hexahydro-1,3,5-trinitro-1,3,5-triazine (RDX) in the gas and condensed phases which give insight into the flexibility of this cyclic nitramine and the effects of the environment on its conformational flexibility and inversion dynamics are described. In Chapter IX, studies of the *cis-trans* conformational dynamics

of HONO in liquid Ar are described. We employed a relatively accurate potential-energy surface which incorporates switching functions to connect the *trans* and *cis* isomers. The effects of a solvent on the equilibrium properties of HONO are discussed. Conclusions and some ideas for future work are discussed in Chapter X.

CHAPTER II

LITERATURE REVIEW OF RDX AND HONO

Hexahydro-1,3,5-trinitro-1,3,5-triazine

Nitramines have been studied experimentally[49-71] and theoretically[72-83] over the past few decades in an attempt to understand their conformational properties and decomposition pathways. Thompson and co-workers performed several calculations on the decomposition of gas-phase nitramines[75] and nitro compounds[76-77]. These studies have concentrated on smaller systems.

One of the more interesting nitramines is hexahydro-1,3,5-trinitro-1,3,5-triazine (RDX) which is used as a component in solid rocket fuels. Due to the low vapor pressure and inherent instability of RDX, most studies have been concerned with the reaction dynamics in the condensed phase. There have been only limited studies of RDX to elucidate its molecular properties, and thus, little is known about it at a molecular level.

RDX is a cyclic molecule comprised of three methylenenitramine (CH_2NNO_2) monomers. McCrone[58] first studied the crystal structure of RDX in 1950. Two polymorphs were observed, α-RDX and β-RDX, the former is stable at room temperature while the latter readily decomposes. In 1972, Choi and Prince[59] refined the crystal structure and showed that RDX has C_s symmetry with the six membered ring portion of the molecule in the chair conformation and two of the exocyclic nitro groups axial while the third nitro group is equatorial (see Fig. 1). Their work showed that strong intermolecular forces are present in the crystal lattice due to short intermolecular distances between O···H as well as O···C atoms. To further study these intermolecular interactions, Haller *et al.*[61]

Figure 1. α-RDX Crystal Structure Obtained From Neutron Diffraction. The triazine ring atoms adopt the chair configuration. Atom types are represented as follows: circles with lines represent carbon, circles with small dots represent nitrogen, circles with large dots represent oxygen, and open circles represent hydrogen.

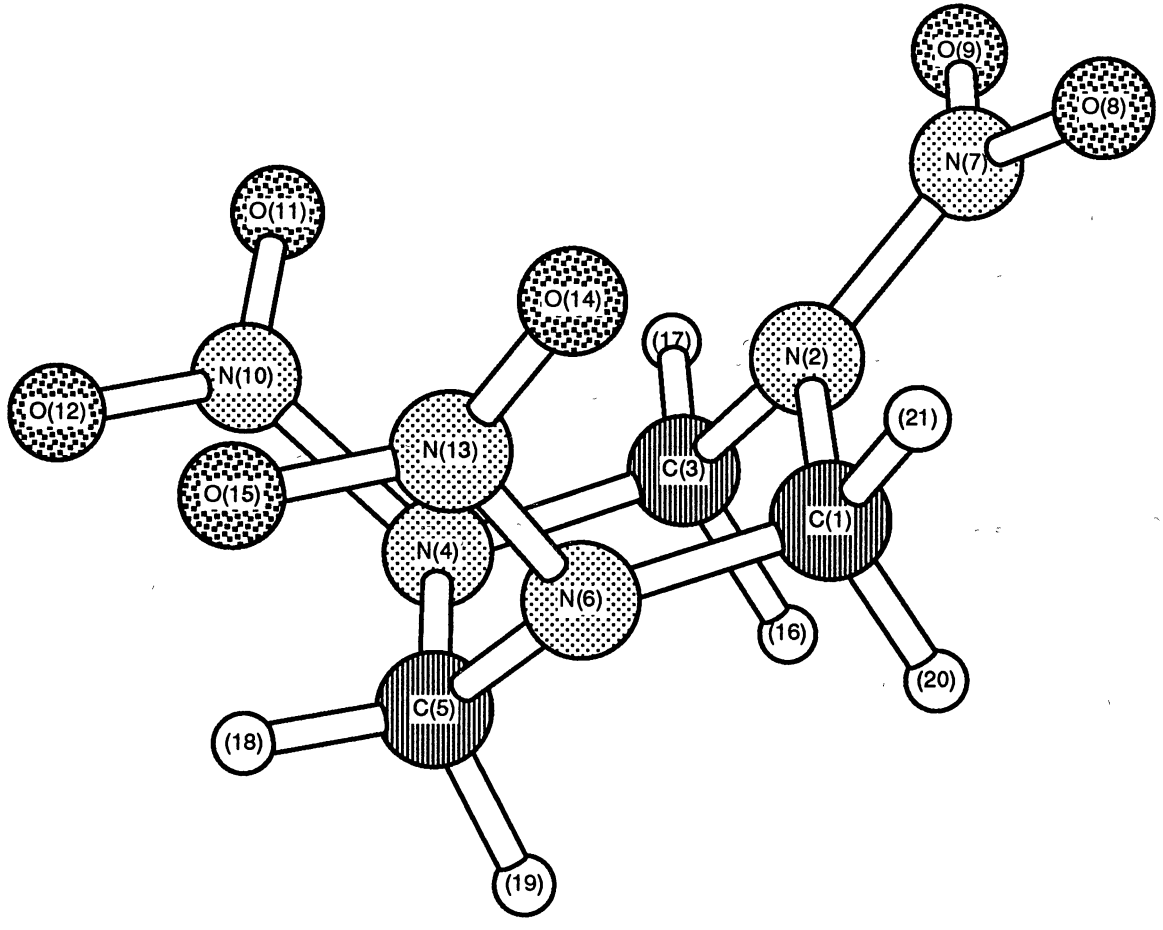

α-Crystal

obtained the crystal structure of a RDX:sulfolane ($C_3H_6N_6O_6 \cdot C_4H_8O_2S$) complex. Their results show that the nitro groups are not as restricted in the sulfolane complex as in the pure crystal and there are fewer short intermolecular contacts. The results of Haller *et al.*[61] concur with the results of Choi and Prince[59] which show that the axial nitro group of one RDX molecule resides in the 'basket' of the neighboring RDX molecule. Rey-Lefon and co-workers[62-64] have obtained a complete infrared spectrum of the α-RDX crystal and calculated a normal force field.

Due to the unstable nature of β-RDX, little is known about it. Karpowitz *et al.*[65] obtained a spectrum of β-RDX. A decrease in the number of frequencies as compared with the α-RDX crystal spectrum illustrates an increase in symmetry. They concluded that β-RDX exhibits C_{3v} symmetry. To date, no crystal structure for β-RDX has been reported.

Some experimental studies of RDX in the liquid and vapor phase have been performed in an attempt to elucidate the conformational properties of the RDX molecule in these different environments. Iqbal *et al.*[66] and Karpowicz and Brill[65] have used infrared spectroscopy to study RDX in solution and the vapor phases, and obtained spectra similar to the β-RDX crystal spectrum. Therefore, RDX is believed to poses C_{3v} symmetry in both the solution phase and the vapor phase with all thee nitro groups equivalent[65] (see Fig. 2).

Karpowicz and Brill[65] studied the the ring inversion using low temperature IR spectroscopy. The RDX molecule, which is similar to cyclohexane, can experience both ring inversion (R1 and R2) and pseudorotation (R3) as shown schematically below. The exocyclic nitro groups and hydrogen atoms have been omitted for clarity. (See Figs. 2 and 3 for RDX in the chair, boat, and twist structures).

Figure 2. Calculated C_{3v} Chair Structure of RDX. Atoms C(1), C(3), N(4), N(6) lie in the plane with the three nitro groups planar. The atom types are represented as in Figure 1.

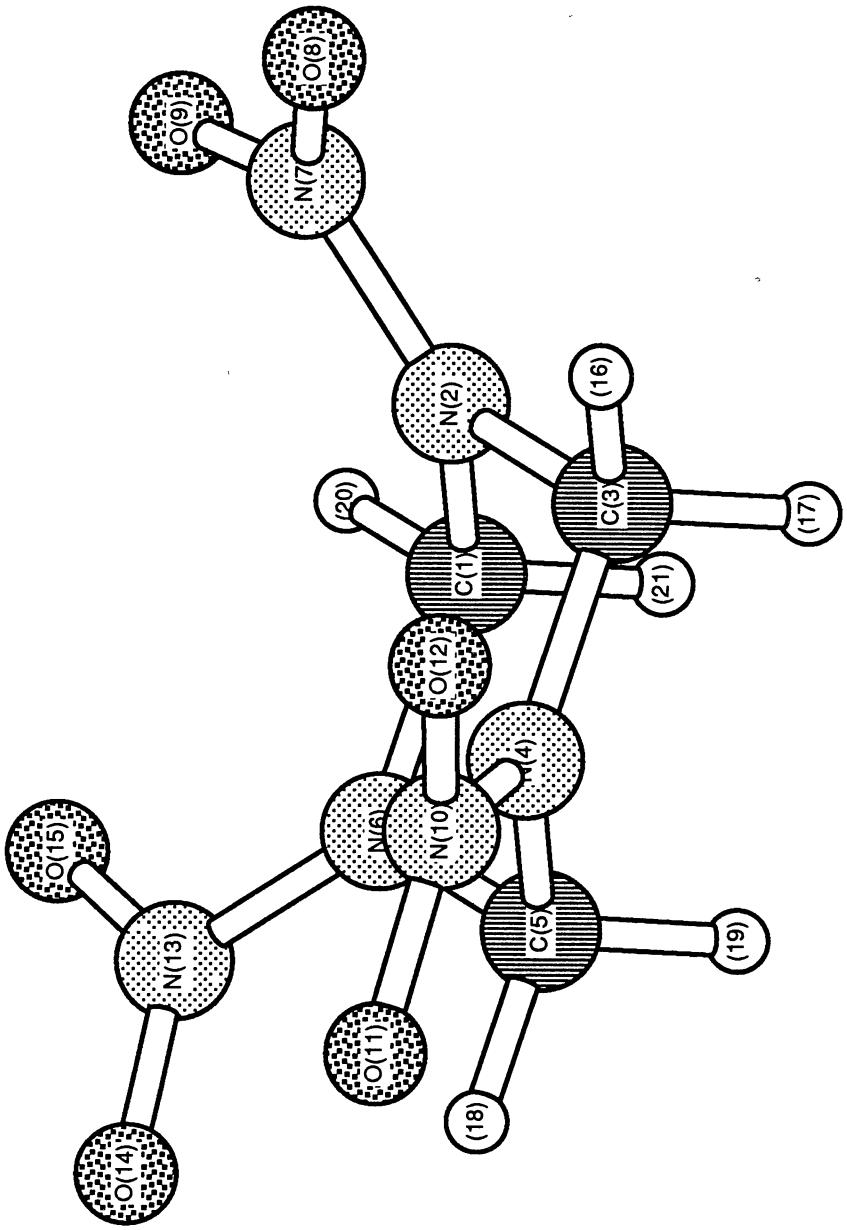

Chair

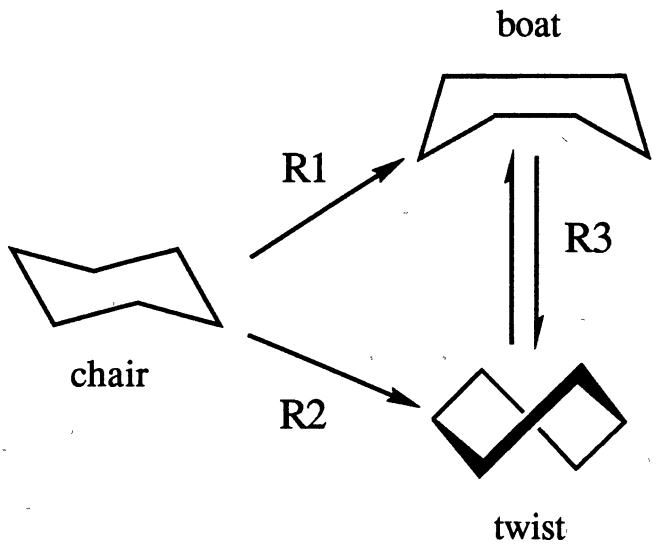

Their results show that even at very low temperatures the barrier to ring inversion is low, however, they could not obtain a value for it. A low barrier is in accord with an earlier study by Lehn *et al.*[67] on the rate of ring inversion for hexahydro-1,3,5-triazine with different exocyclic groups bonded to the nitrogen atoms of the triazine ring. This study showed that as the size of the exocyclic substituent increased or became more electronegative, the barrier for ring inversion decreased.

There have been few theoretical studies of the conformational properties of RDX. Orloff *et al.*[79] used the semi-emperical CNDO method to calculate the energy of the different conformers of RDX, i.e., chair and boat structures (see Fig. 2 and 3a). Their calculations showed the chair and the boat structures to be equal in energy. A barrier for the rotation of the exocyclic nitro group was calculated to be 10 kcal/mol. Filhol *et al.*[80] performed a semi-emperical INDO calculation to study the conformational properties of the exocyclic nitro groups. The most stable conformation was obtained when the nitro groups where in the plane of the C-N-C atoms of the ring (see Fig. 2). This planarity of the nitro group was also observed in smaller nitramines[81]. The dipole moment calculated by Filhol *et al.*[80] is 5.48 D. This is in good agreement with experimental values of 5.78 D[68], 7.0 D[69], 5.73 D[70] and 6.8 D[71]. Calderbank and Pierens[70] used parameters obtained from the

Figure 3. Boat and Twist Minumum Structures of RDX. (a) The calculated C_s boat structure. The boat structure is 1.3 kcal mol^{-1} higher in energy than the chair structure. Atoms C(1), C(3), N(4), and N(6) lie in a plane. (b) The calculated twist structure. The twist structure is 1.3 kcal mol^{-1} higher in energy than the chair structure. Atoms C(1), N(2), N(4), and N(6) lie in a plane. The atom types are the same as in Figure 2, but the molecules have been rotated for clarity.

a

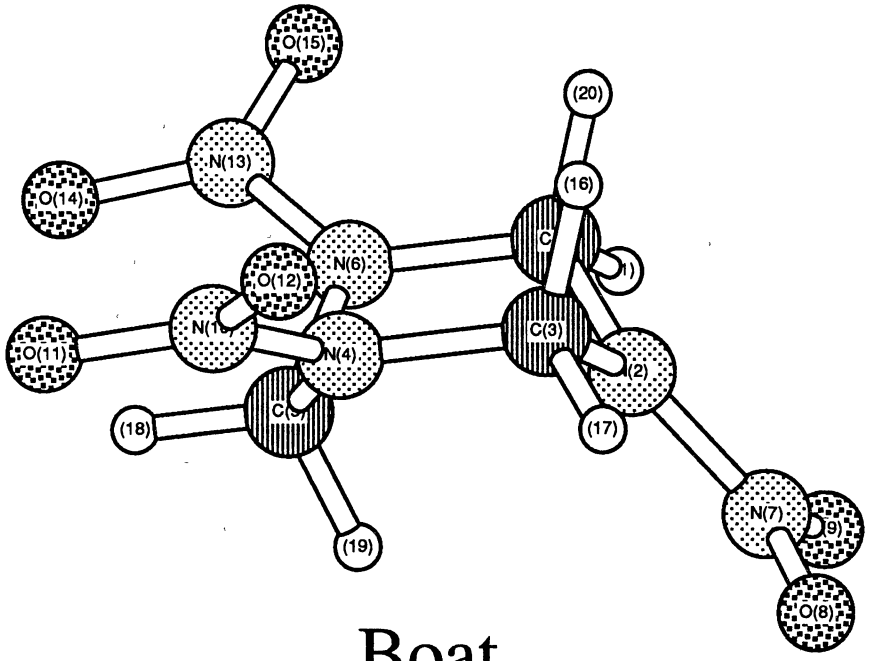

Boat

b

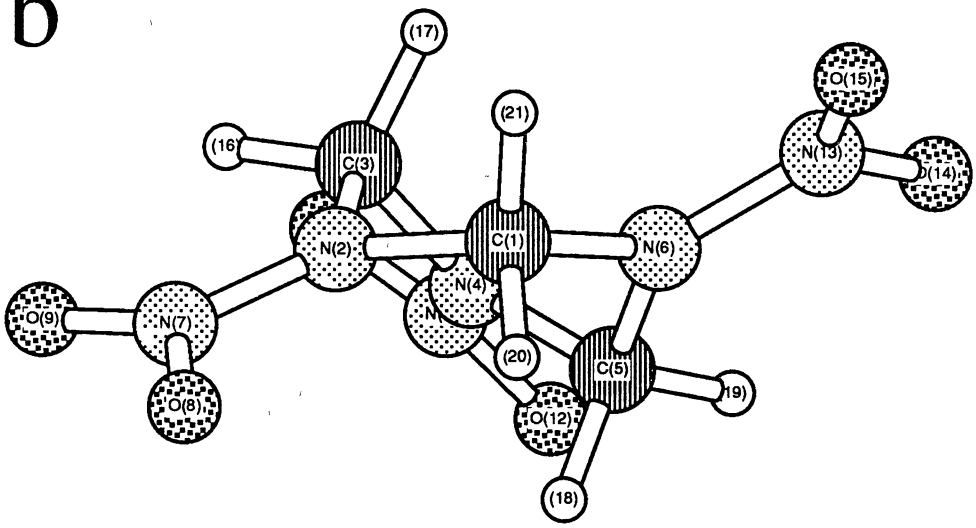

Twist

measured dipole moments and molar Kerr constants of some model compounds to calculate the dipole moment and molar Kerr constant for RDX in the different conformations, i.e., chair, boat, and twist (see Fig. 2, 3a, and 3b). The dipole moments obtained are 6.67 D, 1.74 D, and 2.11D for the chair, boat, and twist conformations, respectively. These values illustrate that no one static structure can reproduce the observed dipole moment (5.73 D[70]) but illustrate (using dipole considerations) that the chair conformation should dominate in any mixture by about 70%. Definitive conclusions cannot be made since a mixture comprised of 70% of the chair conformation gives a molar Kerr constant that is about 240% larger than the observed value. Vladimiroff[83] used molecular mechanics methods[84] to study conformational properties of RDX. The calculated heat of formation and the dipole moment are 47.7 kcal mol^{-1} and 9.9 D respectively. The heat of formation is in good agreement with the experimental value of 45.8 kcal mol^{-1} taken as the heat of formation of the solid[85] plus the heat of sublimation[86]. The dipole moment is a factor of 2 larger than the accepted value of 5.73 D[70].

Recently, Zhao, Hintsa, and Lee[57] studied the unimolecular decomposition of RDX using infrared multiphoton excitation techniques in a molecular beam. They show that the most favorable decomposition pathway is a concerted ring dissociation, in which three of the C-N bonds of the ring break to yield three methylene nitramine moieties, as opposed to the simple N-N bond fission. Sewell and Thompson[78] used classical mechanics to study the unimolecular decomposition of an isolated RDX molecule. They used a potential based on the one developed here; They modified it to include the reaction channels for the two decomposition pathways. Their results show good agreement with the experiment[57] in that the concerted ring dissociation pathway is favored. The studies mentioned above were at energies much higher than in the study presented here.

The goal of this work is to develop a potential-energy surface for gas-phase RDX that is accurate at thermal energies. We have studied the dynamics of conformational changes in the gas phase and obtained barriers for the ring inversion (R1 or R2) and

pseudorotation processes (R3). Also,both the conformational equilibrium and rate constant for the chair→boat/twist ring inversion as a function of the solvent concentration are discussed. Recently, it has been suggested that RDX is soluble in a Xe fluid. Thus, a Xe solvent was employed in this study.

Nitrous Acid

To continue the study of conformational dynamics of polyatomic molecules in condensed phase, we have performed molecular dynamic simulations on nitrous acid (HONO). HONO is a much smaller molecule than RDX and much is known about the potential-energy surface both experimentally and theoretically. HONO experiences conformational equilibrium between the *trans* and *cis* conformations as shown below (R4).

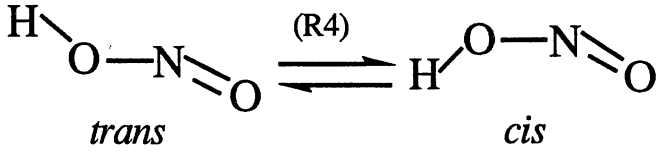

Both experiment[87-93] and theory[94-103] have shown that the *trans* isomer is slightly more stable than the *cis* isomer. Darsey and Thompson[101] have calculated an accurate potential-energy surface, using *ab initio* techniques, for the *trans*—*cis* isomerization. They calculated the *cis* isomer to be 0.6 kcal mol^{-1} higher in energy than the *trans* isomer with a barrier for the *trans*→*cis* isomerization of 9.6 kcal mol^{-1}. In a subsequent paper, Guan and Thompson[103] employed switching functions to smoothly vary the geometry between the *trans* and *cis* isomers. Switching functions will be discussed in more detail in chapter IX.

We have calculated the conformational equilibrium and the *cis*→*trans* and *trans*→*cis* isomerization rate constants for HONO in liquid Ar. Also, the dynamical structure of HONO is discussed.

CHAPTER III

REVIEW OF METHODS AND THEORIES

Molecular dynamics simulations are useful tools for developing and testing potential-energy surfaces and for calculating rate constants for barrier crossing processes. The purpose of this chapter it to briefly introduce the methods and theories relevant to this thesis.

Development of Potential-Energy Surfaces for Large Polyatomic Molecules

Mapping out a potential-energy surface, that is, constructing contour maps or calculating the potential energy of the molecule along a reaction coordinate, for a large molecule can be a formidable task. But finding stationary points on the potential-energy surface can be more tractable. A common methods for obtaining minimum-energy structures and barriers to rotation between minima is adiabatic mapping[9]. Adiabatic mapping assumes that the reaction coordinate is known. The system is moved along the reaction coordinate while periodically minimizing the potential energy by moving all the atoms not explicitly involved in the reaction coordinate. This method gives the potential energy as a function of the reaction coordinate and works well for systems in which the reaction coordinate easily defined. For systems with more complicated reaction coordinates, the contribution of each internal coordinate to the reaction coordinate is usually not well known. Also, with the adiabatic mapping method, dynamical effects are neglected. Molecular dynamics simulations make no assumptions about the stiffness of the molecule.

Unimolecular Reaction Theory

Three important classes of classical theories for calculating rate constants are: transition-state theory, unimolecular rate theory in gases, and the theory of diffusion controlled reactions.

Transition-State Theory

Transition-state theory assumes that a trajectory originating from the reactant well and achieving activation energy, proceeds to the transition state and then on to products. Furthermore, it is assumed that an equilibrium exists between the reactant and transition-state molecules. The transition-state theory rate constant expression in the thermodynamic formulation is given by[105],

$$k_{TST} = (\beta h)^{-1} \frac{Q^{\dagger}}{Q} \exp[-\beta \Delta G^{\dagger}] , \qquad \text{(III.1)}$$

where $\beta = (k_b T)^{-1}$, and k_b and T are the Boltzmann constant and temperature respectively, h is planck's constant, Q and $Q^{\dagger}$ are the partition functions for the reactant and transition state geometries respectively, and $\Delta G^{\dagger}$ is the activation free energy, that is, the free energy difference between the reactant well and the transition state. The rate constant is the equilibrium one way flux across the barrier. Thus, transition-state theory, in effect, assumes that collisions of the solvent molecules with the solute serve to maintain the assumed equilibrium between the reactant and transition-state structures but do not induce barrier recrossings. Barrier recrossings result from trajectories that ascend to the barrier region, cross the transition state, but then return to the reactant well instead of proceeding to the product well.

Lindemann Theory

Transition-state theory does not predict the correct behavior of the unimolecular rate constant at low pressure. The first generally accepted theory for thermal unimolecular reactions was postulated by Lindemann[105-113]. In the primary reaction,

$$A + M \xrightarrow{k_1} A^* + M, \qquad \text{(III.2)}$$

a fraction of reactant molecules, A, become energized to an energy in excess of the critical energy of reaction, E_0, through collisions M, another reactant molecule, inert bath gas atom, or a product molecule. The rate constant for this activation step is denoted by k_1. The energized molecule can either experience a deactivating collision, i.e., the reverse reaction of Eq. III.2,

$$A^* + M \xrightarrow{k_2} A + M, \qquad \text{(III.3)}$$

with rate constant k_2 or proceed to products via the transition state, $A^\dagger$,

$$A^* \xrightarrow{k_3} A^\dagger \xrightarrow{k_4} \text{products.} \qquad \text{(III.4)}$$

The rate of product formation from the transition state geometry is considered to be much faster than the rate for the energized molecules to attain that geometry. Therefore, the rate constant for the energized molecule to proceed to products is approximately k_3, i.e., $k_3 << k_4$, so $k_3 \approx k_3 + k_4$. Using the steady-state approximation for A^*, the overall rate for the change in the concentration of the reactant [A] is given by

$$-\frac{d[A]}{dt} = \frac{k_1 k_3 [A] [M]}{k_2[M] + k_3}. \qquad \text{(III.5)}$$

In the high pressure limit $k_2[M] >> k_3$ and the rate constant is given by,

$$-\frac{1}{[A]}\frac{d[A]}{dt} = \frac{k_1 k_3}{k_2} = k_\infty. \qquad \text{(III.6)}$$

At low pressure $k_2[M] << k_3$ and the rate constant is given by,

$$-\frac{1}{[A]}\frac{d[A]}{dt} = k_1\,[M]. \qquad \text{(III.7)}$$

Therefore, the Lindemann theory predicts that at low pressure, the unimolecular rate constant increases with increasing [M], i.e., $k_{uni} = k_1[M]$, while in the high pressure limit, the unimolecular rate constant is independent of [M], i.e., $k_{uni} = k_\infty$. This region is called the plateau region[108]. In this region, the rate of activation is much faster than the rate of reaction, so an equilibrium concentration of energized molecules is maintained. Thus, in the plateau region, Lindemann theory reduces to transition-state theory, i.e., $k_{TST} = k_\infty$.

Diffusion-Controlled Rate Theory

It has been shown that as the solvent density or viscosity increases, the rate constant for reaction decreases[109-111]. This is attributed to the frequent collisions between the reacting molecules and the solvent. The diffusion-controlled rate constant is proportional to the diffusion constant D,

$$k_D = 4\pi D\sigma \qquad \text{(III.8)}$$

where σ is the reactive radius.

Kramers Theory

The rate constant has been shown to increase with increasing solvent density until it reaches a maximum after which it becomes a decreasing function of pressure (Kramers turnover). Kramers[114] was the first to try and bridge the two models using a single theoretical model.

Kramers incorporated the dynamical influence of the solvent on the rate of barrier crossing. The effects of the dynamics of the solvent can cause a breakdown in transition-state theory by producing barrier recrossing[109-112,114]. Kramers theory, which is derived from a Langevin-Fokker-Plank type equation[109-112], models the reaction coordinate as one dimensional with a constant frictional term acting on this coordinate. The transmission coefficient κ is given by[114]

$$\kappa = \frac{k}{k_{TST}} = \sqrt{1+\left(\frac{\zeta}{2\omega_b}\right)^2} - \left(\frac{\zeta}{2\omega_b}\right), \qquad \text{(III.9)}$$

where ω_b is the frequency of the barrier, that is, the negative eigenvalue corresponding to the reaction coordinate at the transition-state geometry, and ζ is the friction constant per reduced mass acting on the reaction coordinate. The transmission coefficient κ is a measure of the dynamical effects of the solvent, that is, the extent to which the rate constant deviates from the transition-state theory rate constant due to the solute-solvent interactions. Since the friction is assumed constant, the solvent forces, both short-range and long-lived collective motions, act impulsively (Markovian approximation)[109-112].

Grote and Hynes[115-117] derived a statistical theory based on the assumption that the friction is frequency dependent. The theory employes a non-Markovian generalized Langevin equation[109-118] for the reaction coordinate. The Grote-Hynes equation for the transmission coefficient is

$$\kappa = \frac{k}{k_{TST}} = \sqrt{1+\left(\frac{\zeta(\lambda)}{2\omega_b}\right)^2} - \left(\frac{\zeta(\lambda)}{2\omega_b}\right), \qquad \text{(III.10)}$$

where

$$\zeta(\lambda) = \int dt\, \zeta(t) \exp[-\lambda t] \qquad \text{(III.11)}$$

is evaluated at the reactive frequency, λ, and $\zeta(t)$ is the correlation function of the random force,

$$\zeta(t) = \langle R(0)R(t) \rangle, \qquad \text{(III.12)}$$

where R(t) is related to $\zeta(t)$ by the fluctuation-dissipation theorem[119]. For a sharp barrier, there is little friction due to the short time that the molecule is in the transition-state region, $\zeta(\lambda=\omega_b)$ is small[115-117]. Therefore, $k = k_{TST}$ is a good approximation in the sharp barrier (low friction) regime[109]. For a low barrier, $\zeta(\lambda=\omega_b)$ can be large since the molecule can spend an appreciable amount of time in the barrier region and therefore k can deviate significantly from k_{TST}.

As was stated earlier, after the Kramers turnover, the rate constant becomes a decreasing function of the solvent density. It has been shown that at high solvent densities, the rate constant is again an increasing function of the solvent concentration. Deviations from Kramers theory at high solvent densities have been attributed to activated volume effects. The activation volume is given by[105,113]

$$\Delta V^{\dagger} = -\kappa T\left(\frac{\partial \ln k}{\partial P}\right), \qquad \text{(III.13)}$$

where P is the pressure. The activation volume is a measure of the difference in the volumes of the reactant plus solvent packing and transition-state geometry plus solvent packing[120-121]. A negative activation volume suggests a tighter or more compact transition state as compared with the equilibrium structure thus, facilitating solvent packing.

Molecular Dynamics Simulations

Assumptions concerning the interactions, i.e., Markovian or non-Markovian, between the solute and solvent atoms are inherent in statistical theories such as the ones

discussed in the preceding sections. Since the classical equations of motion are numerically solve in molecular dynamics simulations (see chapter V for a more detailed discussion of the molecular dynamics method), this method is useful in checking the reliability of statistical theories by comparing the rate constants obtained from the statistical theory with those obtained from molecular dynamics simulations.

Molecular dynamics simulations are computationally expensive due to the large number of interactions in a liquid system. To circumvent this problem, stochastic molecular dynamics simulations have been employed[122-123]. In this method, the solvent is not considered explicitly, instead the solvent is modeled by using impulsive forces which interact randomly with the solute molecule. Thus, the computational time is greatly reduced. The solute-solvent interaction frequency, α, (the frequency with which the random force interacts with the molecule) can be related to the viscosity of the solvent by $\alpha=c\eta$, where η is the viscosity and c is a constant that depends on the solute but is relatively independent of the solvent[124].

Another method which has been used to calculate the rate constant for activated processes is the reactive flux correlation function[125] which is based on the time correlation of the barrier crossing process and is given by,

$$k(t) = \langle \dot{q}(0)\, \delta[q(0) - q^{TS}]\, H[q(t)] \rangle , \qquad \text{(III.14)}$$

where q is the reaction coordinate, q^{TS} is the value of q at the transition state, $\dot{q}(0)$ is the initial velocity along the reaction coordinate, and H[q(t)] is unity for $0<q(t)<q^{TS}$ and zero otherwise. Reactive flux molecular dynamics simulations are useful for reactions which have activation barriers that are much greater the k_bT since the trajectory is initiated in the transition state region and followed both forwards and backwards in time.

Unfortunately, both of these methods require assumptions that may not be valid. The reactive flux method assumes that a canonical distribution exists in the transition-state

region. Recent studies have shown that this might not be true, that is, local non-equilibrium effects could be important in the region of the transition-state where barrier forces are large[43]. Also, the stochastic molecular dynamics method assumes that the interactions between the solute and solvent are Markovian; this has been disputed by Grote and Hynes[115-117].

The assumptions concerning solute-solvent interactions inherent in statistical theories are absent in *full* molecular dynamics simulations since the solvent is calculated explicitly. Also, by allowing the trajectories to evolve in time according to the potential-energy surface, the behavior of the system along the reaction coordinate and in the transition-state region can be obtained.

CHAPTER IV

LITERATURE REVIEW

The molecular dynamics simulation technique was first developed for simulating hard-spheres[6] and Ar atoms[7,8] in simple liquids. The method was then extended to molecular liquids such as water[126], alkanes[127], and alcohols[127]. With the advent of more powerful computers, molecular dynamics simulations have proven to be a very powerful tool for the study of time varying properties of proteins, nucleic acids, carbohydrates, and polymers in the gas and condensed phases[9-32]. The following review discusses work that is relevant to the studies presented in this thesis. The first section reviews the use of molecular dynamics simulations in the study of conformational flexibility in macromolecules. The last part of this chapter reviews some experimental and theoretical work which studies the effects of a solvent environment on the isomerization rate constant.

Molecular Dynamics Simulations of Conformational Changes in Macromolecules

Due to the high packing density of proteins, the atomic motion near the backbone has been shown to differ from the motion of the atoms near the surface. These different atomic motions give rise to a rich dynamical spectrum that ranges from the rapid local motions of the individual groups to the slow collective motions of larger regions within the molecule. Also, the surface atoms can act as a cage around the atoms near the core of the molecule.

In one of the first molecular dynamics simulations of a protein, McCammon *et al.*[11] studied bovine pancreatic trypsin inhibitor. Their results show that bovine pancreatic trypsin inhibitor is fluid-like at ordinary temperatures, that is, the dynamics of the atomic displacements are dominated by collisions with neighboring atoms. Also, the atomic motion was shown to be highly anharmonic. In an extension of this earlier work, Karplus and McCammon[12] extended the time of the simulation of bovine pancreatic trypsin inhibitor so as to include the collective mode motion. In this simulation, fluctuations in global properties, such as side-chain rotation and transitions between different minima in the neighborhood of the average structure, were observed. The existence of large fluctuations in the structures and energy components indicates that the properties of proteins result from the occupation of a variety of thermally accessible states even on times as short as 10-100 ps.

Studies of the anharmonicity of large biomolecules at room temperature have been performed[13-15]. The results of these studies identify two classes of significantly anharmonic atoms, namely, those which are usually located near the surface or near the ends of the side-chains, which is due to the relatively small structural constraints at such locations.

Post *et al.*[16] used molecular dynamics simulations on native and substrate-bound lysozyme to study the dynamical properties of enzymes and enzyme-substrate complexes. Since the binding of co-factors, substrates, and inhibitors can alter the enzyme conformation, an understanding of the structural rearrangement and changes in motional properties induced by the binding is therefore important for the analysis of enzymatic reactions[16]. They show that the substrate alters the motion of lysozyme and by observing the areas of different fluctuations, the effects of a binding substrate can be obtained.

Harvey and co-workers[17] studied phenylalanine transfer RNA. Their results are similar to earlier protein studies, in that the dynamically averaged structure resembles the

crystal structure even though phenylalanine transfer RNA is comprised of several local structures that are quite different than the relatively homogeneous structure of DNA.

Studied of polysacharides such as α-D glucose[22-24], β-D glucose[23], α-cyclodextrin[18], which is comprised of six (1-4)-linked α-glucose residues, and β-maltose[25], which is the (1-4) linked dimer of α-D glucose, have shown that the glucose ring exhibits considerable flexibility and even undergoes conformational transitions at room temperature. The conformational populations of the different side chain substituents are in fair agreement with the experimental values.

The studies mentioned above were performed *in vaccuo*. Thus, the effects of a solvent environment where neglected. Molecular dynamics simulations of proteins[19-20], nucleic acids[21] and polysacharides[26] in the condensed phase demonstrate that the most important influence of a solvent or crystal environment is on the dynamically averaged structure, i.e., the structure is considerably closer to the x-ray structure than that obtained in the vacuum. For a protein, this is due to the attractive external force which causes a decrease in its density[19]. The magnitudes of the fluctuations of atoms in the interior of the protein are little influenced by the environment. For atoms of side chains at the surface of the protein, the condensed phase environment alters both the magnitude and time course of the fluctuations. This modification in the conformational equilibrium behavior was also observed for the smaller molecules[21,26].

Noid and co-workers[27-31] used molecular dynamics simulations methods to study the conformational dynamics of polyethylene. The effects of anharmonicity in the polyethylene crystal were studied[27-29] and shown to play a large role in the dynamics even at low temperatures. A transition to a conformational disordered crystal, the condis state[27], could be observed using molecular dynamics techniques. Their results also show that "chaotic motion" becomes predominant at sufficiently low temperature and can damp out collective modes which are necessary for the generation of stable defects in the crystal[31].

Rebertus *et al.*[32] used molecular dynamics simulations to study the effects of a solvent on the equilibrium properties, namely the configurational probability distribution, of *n*-butane in CCl_4. The equilibrium constant for the *trans-gauche* isomerization was calculated and compared with the Boltzmann configurational distribution function for gas-phase *n*-butane. Their results show that the conformational distribution shifts towards the *gauche* conformer. They suggest that the shift in the equilibrium is directly related to the ability of the solvent molecules to "pack" around the *gauche* isomer as compared to the *trans* isomer[32]. It has been shown[32,128-131] that the *gauche* isomer is more "spherical" than the *trans* isomer. Therefore, the *gauche* isomer can be accommodated more readily by the solvent than can the *trans* isomer[32].

The studies discussed above have shown that dynamical flexibility is important in the equilibrium conformational dynamics of molecules. The global and local energy minima are usually unaffected by the dynamics but it is clear that conformational flexibility does play an important role in a number of aspects of protein and carbohydrate physical behavior by lowering barriers to transitions and, therefore, affect conformational changes across these different barriers. Both solvent packing effects and anharmonicity can modify the barrier for rotation between neighboring minima, thus substantially affecting the overall average value of any conformational dependent property.

Experimental Studies of the Solvent Effects on Isomerization Rate Constants

The effects of a solvent environment on the rate constant for reactions was discussed in Chapter III. Not only can a solvent environment affect the equilibrium conformational properties of the system, but it can also affect the rate of barrier crossing.

Experimentalist have shown that the rate is proportional to the viscosity (macroscopic measurement of the friction), $k \propto \eta^{-\alpha}$, where for the high viscosity limit of

Kramers equation, $\alpha = 1$, but experimentally, $\alpha < 1$ is generally the case[108,113]. Unfortunately, few molecules have been investigated over a complete viscosity range.

Cates and MacPhil[132] studied the dynamics of *n*-butane as a function of different solvents using Raman spectroscopy. Their results show that the torsional fluctuations are weakly coupled to the collective modes of the solvent and that the short-range solute-solvent interactions are the most important.

Fleming and co-workers[133-135] have studied the effects of different solvents on the isomerization of polyatomic molecules using flash photolysis and absorption spectroscopy. Their results show that molecules with slow isomerization rates require the frequency dependent friction model to explain the observed behavior while molecules with the fastest rates require the zero frequency friction limit, i.e., constant friction, to explain the results. This behavior can be linked to the intramolecular potential in that, molecules with large (sharp) barriers probe a higher frequency region of the solvent than molecules with low (flat) barriers[133].

Rothenberger *et al.*[136] used fluorescence spectroscopy to measure the isomerization rate of *trans*-stilben. Their results show a dramatic increase in the rate of isomerization in solution compared with the gas phase results. They have explained these results by observing which modes are excited in the two different phases. In the gas phase, optical modes are excited primarily and the rate of isomerization is directly related to the rate of energy transfer to the torsional mode by intramolecular coupling, whereas in solution, collisions excite more or less all vibrational states and therefore, the rate of isomerization depends on the efficiency of energy transfer from the solvent to the solute[136].

Millar and Eisenthal[137] studied the isomerization of 1,1'-binaphthyl in different alcohol solvents. They showed that the 1,1'-binaphthyl molecule is strongly coupled to the solvent and obeys Kramers theory over the entire friction regime, i.e., the friction acting on the reaction coordinate is constant. Flom *et al.*[138] studied the isomerization of alkenylantracen as a function of the solvent viscosity. The Grote-Hynes theory models the

experiment well but there is some discrepancy as to the correct $\zeta(\lambda)$ to use in the calculation.

The experiments discussed above show that intermolecular coupling between the solute and solvent can influence the dynamics of barrier crossing processes. The effects of the solvent on the thermodynamic activation parameters, $\Delta G^{\dagger}$, $\Delta H^{\dagger}$, and $\Delta S^{\dagger}$ can help elucidate information about the transition state and coupling between the molecule and solvent.

Hasa, Eguchi, and Jonas[139] have used ^1H NMR spectroscopy to study the ring inversion of cyclohexane in methylcyclohexane-d_{14}, carbon disulfide, and acetone-d_6. Their results show that the activation parameters are independent of the solvent and that the rate constant for ring inversion increased as the pressure increased. These results show that the activation volume and transmission coefficient correlate extremely well with the solvent viscosity, which is proportional to the collision frequency.

True and co-workers[140-149] have studied isomerization reactions using dynamic NMR[150]. Using this technique, pressure dependent rate data may be obtained if the system undergoes distinguishable unimolecular processes with moderate activation energies. Ross and True[140] studied the effects of a solvent environment on the ring isomerization of cyclohexane. They observed a gas-phase inversion rate constant that is 2 to 3 times slower than that in the liquid-phase. This corresponds to activation parameters that are higher in the gas phase than in the liquid phase. The positive difference between the gas-phase and liquid-phase $\Delta G^{\dagger}$ is consistent with a negative activation volume[105,113] (see Eq. III.13, chapter I). A negative activation volume suggests a tighter or more compact transition state than equilibrium structure which facilitates solvent packing[120-121]. Spring and True[141] studied SF_4 and found a negative activation volume, which suggests a tight transition state.

Chauvel and True[143] observed small solvent effects on the activation parameters for methyl nitrite. They suggest that dielectric effects are equal and opposite to the effects of the

solvent pressure on the conformational dynamics of methyl nitrite, where the dielectric effects are caused by the change in polarity between the syn and anti conformers.

Chu and True[145] studied Tetrahydropyran (TPH) ring inversion and the effect of a solvent environment on this cyclic polar molecule. The results show that like the non-polar cyclohexane, the activation parameters and rate constant for ring inversion of THP exhibit a phase dependence. The gas-phase unimolecular rate constant is ~ 4 times slower than the rate constant in the liquid phase. THP also exhibits a negative activation volume which corresponds, as in cyclohexane, to a tight transition-state structure[145].

Chu and True[146] studied cyclohexyl flouride (CF) and obtained the phase dependence of the activation parameters and rate constant for ring inversion. The gas-phase ring inversion rate is ~ 7 times slower and $\Delta G^{\dagger}$ is 10% higher than in the liquid-phase. This leads to a negative activation volume of -8 cm^3 mol^{-1}. The large negative activation volume is attributed to the importance of dielectric effects[146].

LeMasters *et al.*[147-149] has studied three six membered ring systems to complement the previously mentioned ring systems. These are hexahydro-1,3,5-trimethyl-1,3,5-triazine (THTRIZ)[147], N,N-dimethylpiperazine (DMPZ)[148], and N-methylmorpholine (MM)[149]. The experiments show that THTRIZ[147] differs from cyclohexane, THP, and CF, in that, an increase in the rate constant for ring inversion and a slightly lower $\Delta G^{\dagger}$ is observed in the gas phase as compared with its liquid counterpart, which is consistent with a positive activation volume. The activation volume for THTRIZ is ~ 1 cm^3 mol^{-1}. This could be due to the bulky exocyclic methyl groups and the possibility of a "loose" transition state due to the rapidly inverting ring nitrogens[151]. DMPZ[148] also has a lower $\Delta G^{\dagger}$ in the gas phase than in the liquid phase and yields a positive activation volume of 4 cm^3 mol^{-1}. The ring inversion rate constant for MM[149], which incorporates both N and O into the six membered ring, exhibits a phase dependence similar to cyclohexane, THP, and CF, i.e., slower rates and a higher activation free energy in the gas-phase as compared to the liquid-phase. The decrease in $\Delta G^{\dagger}$ gives a negative activation volume which was estimated to be -

9 cm^3 mol^{-1}. This is the largest negative activation volume in the series of six membered rings; cyclohexane[140] (-4 cm^3 mol^{-1}), THP[145] (-5 cm^3 mol^{-1}), CF[146] (-8 cm^3 mol^{-1}), but opposite to THTRIZ[147] (1 cm^3 mol^{-1}) and DMPZ[148] (4 cm^3 mol^{-1}).

The value of $\Delta S^{\dagger}$ for MM[149] is 0.8 cal mol^{-1} K^{-1} and is the lowest value of $\Delta S^{\dagger}$ for the series of six membered rings; cyclohexane[140] (5.7 cal $mol^{-1}K^{-1}$), THP[145] (6.0 cal $mol^{-1}K^{-1}$), CF[146] (3.3 cal $mol^{-1}K^{-1}$), THTRIZ[147] (2.8 cal $mol^{-1}K^{-1}$), and DMPZ[148] (6.1 cal $mol^{-1}K^{-1}$). Such large activation entropies suggests freely pseudorotating transition states which were predicted by Pickett and Strauss[152] for cyclohexane and related oxanes. The small $\Delta S^{\dagger}$ for MM suggest that pseudorotation in the transition state is significantly hindered which could be due to the asymmetry of the ring.

Theoretical Studies of the Solvent Effects on Isomerization Rate Constants

In the experimental study of the ring inversion of cyclohexane[139] in high-pressure liquids, the rate constant for ring inversion is observed to increase as the pressure increases. This result has been questioned since statistical calculations on simple models predict that the transmission coefficient should decrease with increasing liquid pressure for most isomerization reactions[111]. Thus, if the statistical calculations are to agree with experiments, it must mean that the transition-state theory rate constant is an increasing function of the solvent density and increasing at a much faster rate than the decrease in transmission coefficient. Therefore, to bring theory into accord with experiment, Chandler and co-workers[39-40,124] used the reactive flux correlation method to study the chair→boat ring inversion for cyclohexane. They show that the solvent contribution to the activation free-energy is positive but quite small and an increasing function of the pressure. Therefore, transition-state theory predicts a small (if any) decrease in the rate of ring inversion with increasing pressure. The stochastic molecular dynamics simulation shows that the transmission coefficient increases with increasing pressure. They attribute this

increase in the transmission coefficient to additional coupling to the solvent environment which enhances the rate of stabilization of the molecules after passing through the activated transition state. Their results show that quasiperiodic motion is important in the liquid phase isomerization of cyclohexane. Since the nonchaotic trajectories deplete the rate, the ability of the solvent to quench these trajectories leads to increased rates with increasing pressure or density.

Robinson and co-workers[41-43] have used full molecular dynamics simulations to study the solvent effects on model systems. Performing full molecular dynamics simulations provides information unavailable from the reactive flux method[125]. For example, if the reaction occurs under non-equilibrium or non-steady state conditions, dynamics distant from the transition state could be important[153-154]. Statman and Robinson[41] and Zhu, Lee, and Robinson[42] studied the frequency-dependent friction along the reaction coordinate for a model system with a symmetric double well potential. If the intramolecular potential solely determined the rates, the equilibrium constant should be unity. The equilibrium constant obtained from the molecular dynamics simulations deviated by a factor of 10, thus solvent effects must play a role in the isomerization dynamics.

The rate constants for isomerization, obtained from the molecular dynamics simulations, were compared with the rate constants obtained using Kramers[114] theory and the Grote-Hynes frequency-dependent friction model[115-117]. Neither of the statistical theories reproduce the rate constants obtained from the molecular dynamics calculations. Therefore, the entropic contribution to the rate constants due to the change in the hydrodynamic volume upon isomerization was calculated. The Flory-Huggings[155a] equation

$$k_b^{-1} (\Delta S)_v \approx \Delta V_B \left[\frac{1}{V_S} - \frac{1}{V_B} \right] - N_S \ln \left[1 + \frac{\Delta V_B}{N_S V_S} \right] \qquad \text{(IV.1)}$$

(where N_S is the number of solvent molecules, N_B is the number of isomerizing molecules, V_S is the volume of a single solvent molecule, and V_B is the volume of a single isomerizing molecule) was used to calculate the entropic contribution to the rate constant. Incorporation of the entropic term into the statistical rate constants partially resolves the difference between the statistical theories and molecular dynamics simulations.

Zhu and Robinson[43] have used molecular dynamics simulations to study ultrafast dynamics in a model quasi-diatomic system, i.e., a double well potential in which a reaction occurs between an inner well at a contracted bond distance and an outer well at an extended bond distance. If the condensed-phase barrier crossing reaction takes place rapidly with respect to the solvent motion, local non-equilibrium dynamics may exist[43]. They observe deviations from Maxwell-Boltzmann behavior. They show that the kinetic energy of the quasi-diatomic molecule along the reaction coordinate is not evenly distributed. On average, molecules with shorter bond lengths are relatively cool while those having bond lengths near the outer minimum are relatively hot. They suggest that once the molecule becomes excited, interaction with the heat bath becomes less efficient due to the disparity in the frequencies between the molecule and solvent bath. Therefore, the less efficient the interactions between the molecule and solvent, the more severe the distortion of the kinetic energy distribution along the reaction coordinate[43].

Straub *et al.*[44] studied the isomerization of a diatomic model similar to the model system of Zhu and Robinson[43]. Their results show that simple theories such as Kramers[114] theory and Grote-Hynes theory[115-117], predicts the correct rate constant as long as the frictional interaction between the solvent and the reaction coordinate and the potential of mean force are accurately known. Unfortunately, these quantities cannot be estimated with sufficient accuracy for many realistic systems. Thus, methods such as molecular dynamics simulations must be used to calculate them.

Marks *et al.*[156] studied the isomerization of methyl isocyanide in a dense argon fluid. Their results show that the isomerization rate constant increases as the solvent

density increased until it reaches the plateau region (the rate constant is independent of the bath gas concentration), as predicted by Lindemann theory (see Chapter III). As the concentration further increases, the magnitude of the rate constant exhibits a dramatic increase. This deviation from Lindemann theory was attributed to a negative activation volume (Eq.III.13)[156].

CHAPTER V

COMPUTATIONAL PROCEDURES

Introduction

Two generally accepted procedures for calculating equilibrium properties of molecules in the gas and condensed phases are Monte Carlo[1-2,157] and molecular dynamics[1-5]. Monte Carlo methods use pseudo-random configurations of the atoms which are selected from a canonical distribution. The average value of variable $\langle \mathcal{A} \rangle$ is obtained by solving the equation,

$$\langle \mathcal{A} \rangle = Z^{-1} \int \mathcal{A} \exp[-\beta V(\mathbf{q})] d\mathbf{q}, \tag{V.1}$$

where Z is the classical partition function given by,

$$Z = \int \exp[-\beta V(\mathbf{q})] d\mathbf{q}. \tag{V.2}$$

$V(\mathbf{q})$ is the potential energy at a configuration $\mathbf{q}(q_1, q_2, ..., q_n)$ and $\beta = 1/\kappa T$ where κ is the Boltzmann constant and T is the ensemble temperature. In the Monte Carlo solution of Eq. V.1, the average is expressed[1-2,157]

$$\langle \mathcal{A} \rangle = \lim_{N \to \infty} N^{-1} \sum_{i=1}^{N} \mathcal{A}_i. \tag{V.3}$$

The sum can be estimated using Metropolis[158] sampling methods. This is accomplished by performing a Markov walk. In each Markov step a new trial configuration is generated by moving an atom according to,

$$q_{trial} = q_{old} + (0.5 - \xi_1)\,\delta q\,, \qquad (V.4)$$

where ξ_1 is a random number distributed uniformly over the interval [0,1]. If the move lowers the energy of the system, than the trial configuration is saved as the new configuration. If the move raises the potential energy of the system, the move is accepted with a probability of $\exp[-\Delta V/\kappa T]$, where $\Delta V = V_{trail} - V_{old}$. This is accomplished by choosing a random number, ξ_2, and if $\xi_2 < \exp[-\Delta V/\kappa T]$, then the trial configuration is accepted; otherwise, the move is rejected and the system is returned to the old configuration. This procedure is repeated until convergence is achieved. The value of δq is chosen so that 40-50% of the trial moves are accepted. At each step in the Markov chain, the computed averages are updated.

Since the potential energy is a function of only the configuration of the molecule, the dynamical properties of the system are not considered.

The second method, molecular dynamics simulations[1-5], involves the solution of the classical equations of motion. The calculation of the equilibrium properties are then obtained by invoking the ergodic hypothesis which states that as the time of the trajectory approaches infinity, the time-average will approach the ensemble average (Eq. V.1). The advantage of molecular dynamics simulations compared with the Monte Carlo method is that the time varying properties of the system can be studied.

The molecular dynamics simulation technique was first developed for simulating hard-sphere[6] and Ar[7-8] atoms in simple liquids. The method was then extended to molecular liquids such as water[126], alkanes[127] and alcohols[127]. Molecular dynamics simulations have also proven to be a very powerful tool for the study of time varying

properties of proteins, nucleic acids, carbohydrates, and polymers in the gas, solution, and crystal phases[9-32].

Molecular dynamics simulations are performed by numerically integrating Hamilton's equations of motion,

$$\dot{\mathbf{p}} = -\frac{\partial H(\mathbf{p},\mathbf{q})}{\partial \mathbf{q}} \qquad \text{(V.5)}$$

and

$$\dot{\mathbf{q}} = \frac{\partial H(\mathbf{p},\mathbf{q})}{\partial \mathbf{P}}, \qquad \text{(V.6)}$$

where $H(\mathbf{p},\mathbf{q})$ is the Hamiltonian for the system, $\mathbf{q}(q_1,q_2, \ldots q_n)$ and $\mathbf{p}(p_1,p_2, \ldots p_n)$ are the coordinates and conjugate momenta of all the particles at some initial time t_o, respectively; and $\dot{\mathbf{q}}$ and $\dot{\mathbf{p}}$ are the time derviatives of the coordinates and momenta, respectively.

Since the number of particles included in an molecular dynamics simulation is small, usually between 10 - 10^3, the particles are confined to a "box" with periodic boundary conditions. (Some of the mechanics of periodic boundary conditions will be discussed later in this chapter.) The primary box of particles is than repeated to create an infinitely periodic system. This method reproduces equilibrium properties of liquids well if the number of solvent atoms is greater than ca. 100. Bunker *et al.*[159], in a calculation of the recombination of I_2 in Ar, showed that if fewer than 100 solvent atoms were incorporated, the dissociating iodine atoms could interact with a solvent atom and its periodic image.

Calculations for systems with 100 or more solvent atoms can require a considerable amount of computational time. Since activated events are usually localized events, i.e., relatively few solvent atoms participate directly in the dynamics of the solute, the effect of a solvent atom far way from the solute molecule is diminished. Therefore, it is desirable to

avoid detailed calculations of the trajectories of atoms distant from the activation site. Thus, a method which incorporates only the necessary number of atoms into the dynamical calculation and models the interactions between the reacting molecule and the bulk solvent through a potential of mean force is desirable.

Bunker *et al.*[159], Murrell and co-workers[160-163], and Stace[164] applied a technique developed by Lennard-Jones and Devonshire[165] for modeling rare gas fluids. This method uses a finite volume where the walls of the container, usually a sphere, are comprised of stationary solvent atoms. Inside the sphere, the solvent atoms are allowed to move according to the potential-energy function, while the atoms comprising the wall act as a potential of mean force on the solvent atoms inside the sphere. Murrell and co-workers[160-164] and Stace[164] used the Born-Meyer potential to model the solute-wall and solvent-wall interactions. It has been shown[156,160-164] that with about 8 to 32 solvent atoms, this model gives good qualitative results, and the computational time is decreased dramatically. It should be noted that, due to the absence of periodicity, the long range interactions and long time correlation effects observed in systems where periodic boundary conditions are employed would not be present using this model. Brooks and Karplus[166] have shown that this model should be representative of a dense gas.

Berkowitz and McCammon[167], retaining the boundaries of the finite volume method[165], incorporated stochastic boundary conditions in an attempt to decrease the surface effects. In their model, three regions are defined: a reaction region, which is the most inner area of the sphere; a bath region which surrounds the reaction region; and a reservoir region which is used to contain the particles in the reaction and bath regions. The atoms in the reaction and bath regions move according to Hamilton's equations of motion[1] and stochastic dynamics[125], respectively, while the reservoir atoms remain fixed. The particles of the reaction and bath regions are allowed to pass into the neighboring region. Thus, as a particle from the reaction region passes into the bath region, the dynamics of that particle switches from molecular dynamics (Hamilton's equations of motion) to stochastic

dynamics. The same occurs for a particle in the bath region that moves into the reaction region. This method reproduces the solvent structure and long time correlations well, but cannot quantitatively reproduce the results of a infinitely periodic system[167].

Brooks and Karplus[166] have extended the method of Berkowitz and McCammon[167] by introducing a deformable boundary rather than a predetermined configuration of particles for the reservoir region. Brooks and Karplus[166] assume that the forces on an atom in the reaction and bath regions due to particles beyond the boundary arise from the average structure of the bulk solution. Therefore, for a simple liquid, only knowledge of the pair distribution function is required. The molecular dynamics simulation is performed by conventional techniques with the addition of a deformable boundary force arising from the mean field interactions with particles beyond the boundary. They show that the structural, dynamics, and thermodynamic properties calculated are in satisfactory agreement with a conventional molecular dynamics simulation, but at a large reduction in computational time.

The problem of surface effects can be overcome by implementing periodic boundary conditions[1,168]. In this method, a cubic box is replicated throughout space to form an infinite system. In the course of the simulation, as a molecule moves in the primary box, its periodic image in each of the adjacent boxes moves in exactly the same manner. Therefore, as a molecule leaves the primary box, one of its periodic images enters through the opposite face. There are no walls at the boundary of the primary cell and therefore, no surface effects.

Potential-Energy Surface

The Hamiltonian for the system is given by,

$$H = \sum_{i=1}^{N} \frac{P_i^2}{2m_i} + V_{intra} + V_{inter} + V_{wall} \qquad (V.7)$$

where V_{intra} is the potential term for the molecule, V_{inter} is the potential term for the molecule-solvent and solvent-solvent interactions, and V_{wall} is the interaction of the molecule and the solvent with the boundary of the reaction sphere.

The intramolecular potential is given as follows,

$$V_{intra} = V_{bond} + V_{bend} + V_{wag} + V_{torsion} + V_{L\text{-}J}, \tag{V.8}$$

where the bonds are represented by harmonic or Morse potentials,

$$V_{harmonic} = \sum_i \frac{1}{2} k_s (r_i - r_i^o)^2 \tag{V.9}$$

or

$$V_{Morse} = \sum_i D_e (1 - e^{-\alpha(r_i - r_i^o)})^2, \tag{V.10}$$

with k_s, D_e and r^o being the harmonic force constant, dissociation energy, and equilibrium bond distance respectively. The curvature parameter, α, is given by,

$$\alpha = \sqrt{\frac{k_s}{2D_e}}. \tag{V.11}$$

The bond angles and wag angles are represented by harmonic potentials,

$$V_{bend} = \sum_i \frac{1}{2} k_b (\theta_i - \theta_i^o)^2 \tag{V.12}$$

and

$$V_{wag} = \sum_{i} \frac{1}{2} k_{\gamma}(\gamma_i - \gamma_i^o)^2, \qquad (V.13)$$

with k_b and Θ^o being the bond angle force constant and equilibrium bond-angle respectively, and k_γ and γ^o being the wag angle force constant and equilibrium wag angle respectively. The dihedral angles are represented by a three-term cosine series,

$$V_{torsion} = \sum_{i} \sum_{j=0}^{2} a_j \cos(j\tau_i). \qquad (V.14)$$

where the a_j's are fitting parameters. The non-bonded interaction, i.e. interactions between any two atoms not bonded to each other or to a common atom, are represented by Lennard-Jones 6-12 interactions,

$$V_{L\text{-}J} = \sum 4\varepsilon_{ij}\left\{\left(\frac{\sigma_{ij}}{r_{ij}}\right)^{12} - \left(\frac{\sigma_{ij}}{r_{ij}}\right)^{6}\right\}, \qquad (V.15)$$

where r_{ij} is the distance, σ_{ij} is the atomic radius, and ε_{ij} is the Lennard-Jones well depth between atoms i and j. The atomic radius and Lennard-Jones well depths are calculated using the Lorentz-Berthelot mixing rules[1],

$$\sigma_{ij} = [\sigma_i + \sigma_j] \qquad (V.16)$$

and

$$\varepsilon_{ij} = \sqrt{\varepsilon_i \varepsilon_j}, \qquad (V.17)$$

where σ_i and ε_i are the atomic radius and Lennard-Jones well depth for the ith atom.

The molecule-solvent and solvent-solvent interactions, V_{inter}, are also represented by the Lennard-Jones 6-12 potential given in Eq. V.15. All solvent-molecule and solvent-solvent interactions were included, that is, no explicit cutoff distance was used.

Finite Volume Method

For the finite volume method[160-164], a wall potential, V_{wall}, describing the molecule-wall and solvent-wall interactions is modeled using a modified Born-Meyer interaction of the form[156],

$$V_{wall} = \sum_i \frac{A\rho_i^2}{R^2} e^{-b(R-\rho_i)}, \qquad (V.18)$$

where R is the radius of the sphere and ρ_i is the distance of atom i from the center of the sphere. The ρ^2 term in the numerator guarantee the potential and first derivative go to zero at the center of the sphere (ρ=0). The parameters A and b are set so that the wall potential will be large enough to confine the solute and solvent atoms, yet 'soft' enough so that the integration step size will not have to be decreased appreciably to retain good energy conservation. On average, the kinetic energy of an atom is $3\kappa T/2$ and since only one component of the momenta is required to change sign for an atom to be reflected by the wall, an individual atom will be confined within $\rho < R$ if

$$V_{wall}(\rho(T)) \geq \frac{1}{2}\kappa T, \qquad (V.19)$$

where the equality gives the maximum distance from the center of the sphere ($\rho(T)$), on average, that an atom can achieve for a given temperature. The values of A and b are taken empirically as 100 kcal mol^{-1} and 9.5 $Å^{-1}$, respectively. The inequality in Eq. V.19 is shown in Figure 4 for the temperature range 400 to 1500 K using our choice of potential

Figure 4. Effective Radius Versus Temperature. The open circles represent the average maximum distance from the center of the sphere an atom will achieve at a particular temperature.

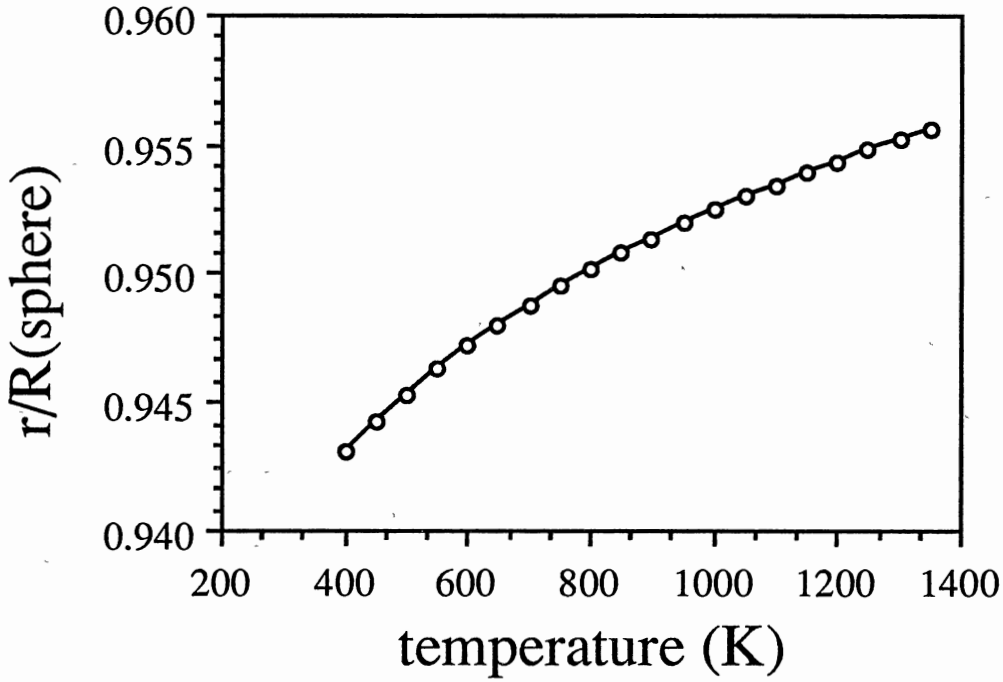
0.960
0.955
0.950
0.945
0.940
r/R(sphere)
200
400
600
800
1000
1200
1400
temperature (K)

parameters for V_{wall}. This shows that over a large range of temperatures, the average distance that a particle will experience from the center of the reaction sphere is ca. 0.945 to 0.955 R, where R is the radius of the sphere.

Periodic Boundary Method

The periodic boundary method simulates an infinitely periodic system. This is achieved by requiring that as a molecule leaves the primary box, one of its images enters the primary box through the opposite wall[1,168]. This can be achieved by following a particle in the primary box and switching attention to its periodic image when it leaves the box by adding or subtracting L to its x, y, or z coordinate (depending on the face the exiting particle passes through), where L is the length of the box.

The minimum image convention by Metropolis[158] was employed. In this scheme, molecule *i* is at the center of a region which has the same size and shape as the primary cell. Molecule *i* interacts with all the molecules whose centers lie within this region, that is, with the closest periodic images of the N-1 neighboring molecules. Using this convention produces a cutoff distance of $\frac{1}{2}$ L. Thus, the potential interaction between two particles separated by more than this distance is assumed to be zero. The error generated by this convention should be negligible if the length of the box is $\approx 6\sigma$, where σ is the atomic radius of the solvent atoms[1]. At a distance of 6σ, the potential interaction between two solvent atoms is ~0.0001ε, where ε is the Lennard-Jones well depth. Using the minimum image convention, there are $\frac{1}{2}$N(N-1) pairwise interactions.

In this work, the frame of reference is moved after each step of the simulation such that the center of mass of the solute molecule remains at the origin of the coordinate system[42].

Procedures

The initial configuration of the molecule is taken as the equilibrium structure and its center of mass is placed at the origin of the coordinate system. The initial configuration of the solvent is obtained by placing the solvent atoms in a fcc arrangement around the solute molecule. The edge of the lattice is calculated as,

$$L = \left(\frac{m_\alpha + m_\beta}{D}\right)^{1/3} \tag{V.20}$$

with m_α and m_β being the total mass of the solute and solvent respectively and D is the density of the solution.

It is desired for the initial configuration of the system to be at a low potential energy, but this is not always possible as the density increases. Therefore, an annealing trajectory is calculated to allow the system to relax away from the initial strained configuration. This is accomplished by zeroing the atomic momenta whenever the kinetic energy of the system becomes larger than the potential energy. Usually, about 1.0 to 2.0 ps of annealing is sufficient to remove any large potential energy due to the starting configuration.

The initial values for the momenta of each atom are selected randomly from a thermal distribution,

$$P_i = \xi\sqrt{m_i \kappa T_o}\ , \tag{V.21}$$

where ξ is a random number weighted by a Gaussian distribution, m_i is the mass of the ith atom, and κ and T_o are the Boltzmann constant and desired ensemble temperature, respectively. An initial warm up trajectory is calculated by numerically integrating Hamilton's equations of motion. Only one warm up trajectory is performed for each

ensemble of trajectories. During the warm up trajectory, the momenta were scaled periodically to the ensemble temperature T_0 using the scaling factor[20]

$$sf = \sqrt{\frac{2T_0}{\langle \mathcal{T} \rangle} - 1}, \tag{V.22}$$

where $\langle \mathcal{T} \rangle$ is the temperature averaged over a specified interval. The instantaneous temperature of the trajectory is given by,

$$\mathcal{T} = \frac{1}{ndf\,\kappa} \sum_{i=1}^{N} \frac{P_{x_i}^2 + P_{y_i}^2 + P_{z_i}^2}{m_i}, \tag{V.23}$$

where ndf is the number of degrees of freedom for the system (3N-6 for a gas-phase molecule and 3N for a solution), κ is the Boltzmann constant, N is the total number of atoms in the system, m_i is the mass of the ith atom, and P's are the Cartesian momenta for the ith atom. The warm up trajectory should be long enough to destroy any artifacts of the initial configuration of the system. Periodically during the warm up trajectory, configurations of the system are saved as initial configurations for subsequent trajectories for that ensemble.

Using one of the saved configurations from the warm up trajectory, a new set of momenta for each atom is sampled from a thermal distribution using Eq. V.21 and the trajectory is equilibrated by periodic temperature scaling. The equilibration time should be sufficient such that the mean fluctuations in the temperature are close to zero, the rotational and translational energy of the solute are $1.5\kappa\langle T \rangle$, where $\langle T \rangle$ is the time-averaged temperature of the trajectory respectfully, and the internal kinetic energy of the solute is close to $\frac{(3N_{solute}-6)}{2}\kappa\langle T \rangle$, where N_{solute} is the number of atoms in the solute. After the equilibration time, the trajectory is continued without further temperature scaling and phase-space points are saved periodically for subsequent analysis.

During each trajectory, the temperature and pressure of the system and the translational energy (E_{trans}), rotational energy (E_{rot}), and internal energy ($E_{internal}$) of the solute are calculated. The temperature is calculated using Eq. V.23. The average pressure[1] is calculated using,

$$\mathcal{P} = \frac{N\kappa\mathcal{T}}{V} - \frac{1}{3V}\left(\sum_{i=1}^{N}\sum_{j>i}^{N} r_{ij}\cdot\frac{\partial V(r_{ij})}{\partial r_{ij}}\right) \qquad (V.24)$$

where $\mathcal{T}$ and V are the instantaneous value of temperature and volume, N is the total number of atoms, and the term in the brackets is the intermolecular pair virial where $V(r_{ij})$ represents the molecule-solvent and solvent-solvent potential-energy terms (for a complete derivation, see Appendix A). The translational energy is given by[169],

$$E_{trans} = \frac{1}{2}M(V_x^2 + V_y^2 + V_z^2) \qquad (V.25)$$

where V_x, V_y, and V_z are the center-of-mass Cartesian velocities and M is the total mass of the solute. The rotational energy is given by[169],

$$E_{rot} = \frac{1}{2}\mathbf{L}^T\,\mathbf{I}^{-1}\,\mathbf{L} \qquad (V.26)$$

where **L** is the angular momentum vector,

$$\mathbf{L} = \sum_{i=1}^{N}[\,\mathbf{r}_i \times \mathbf{P}_i], \qquad (V.27)$$

with $\mathbf{r}_i$ and $\mathbf{P}_i$ being the position and momentum vector of the ith atom relative to the center-of-mass of the molecule, respectively, and **I** is the moment of inertia tensor for the solute molecule. The internal energy of the solute molecule is given by,

$$E_{internal} = E_{total} - (E_{trans} + E_{rot}) \qquad (V.28)$$

where E_{total} is,

$$E_{total} = E_{kin} + V_{intra}, \tag{V.29}$$

with E_{kin} being the internal kinetic energy given by

$$E_{kin} = \sum_{i=1}^{N_{solute}} \frac{P_{x_i}^2 + P_{y_i}^2 + P_{z_i}^2}{2m_i}, \tag{V.30}$$

(where the external rotational and translational energy of the solute has already been subtracted) and V_{intra} is given by Eq. V.8. All the other variable have their usual meaning. Using this definition for the total energy of the solute molecule, the energy due to coupling between the solute and solvent is neglected.

The time-averaged temperature is calculated by sampling the instantaneous temperature (Eq. V.23) during a trajectory. The ensemble-averaged temperature is then deduced from the mean of the individual trajectories comprising the ensemble. The time-average and ensemble-average values of the pressure ($\mathcal{P}$), E_{trans}, E_{rot}, $E_{internal}$, and E_{kin} are obtained in the same manner.

The gas-phase molecular dynamics calculations were performed using the general trajectory code, GenDyn[170] with modifications to include canonical initial conditions.

Minimum and Transition-State Structures

Mapping out the entire potential-energy surface is a formidable task, but calculating stationary points is slightly more tractable[171]. We have employed three different ways of calculating the stationary points on the potential-energy surface.

Minimum Structures

One method employed to obtain the minimum energy structure is the minimization routine STEPIT[172] which requires only the function to be minimized. Unfortunately, STEPIT is vary time consuming, especially when minimizing numerous structures far from the local minimum.

Another method employed for finding minimum structures is the variable metric method[171,173]. In this method, an approximation to the inverse Hessian, $\mathbf{H}^{-1}$, is constructed iteratively such that[171]

$$\lim_{i\to\infty} \boldsymbol{A}_i = \mathbf{H}^{-1} \tag{V.31}$$

where $\boldsymbol{A}_i$ is a sequence of matrices. If the potential-energy surface is approximated as a harmonic function,

$$V(\mathbf{q}) = V(\mathbf{q}_m) + \mathbf{g}^T(\mathbf{q} - \mathbf{q}_m) + \tfrac{1}{2}(\mathbf{q} - \mathbf{q}_m)^T\,\mathbf{H}\,(\mathbf{q} - \mathbf{q}_m), \tag{V.32}$$

where $V(\mathbf{q})$ is the potential-energy at configuration $\mathbf{q}$, $\mathbf{g}$ is the computed gradient, and $\mathbf{H}$ is the approximate Hessian, than the minimum configuration, $\mathbf{q}_m$, will satisfy,

$$\mathbf{H}\cdot\mathbf{q}_m = \mathbf{g} \tag{V.33}$$

while at any point, $\mathbf{q}_i$, Eq. V.33 becomes

$$\mathbf{H}\cdot\mathbf{q}_i = \frac{\partial V(\mathbf{q}_i)}{\partial \mathbf{q}_i} + \mathbf{g}\ . \tag{V.34}$$

Subtracting Eq. V.34 from Eq. V.33 and multiplying by $\mathbf{H}^{-1}$ yields,

$$\mathbf{q}_m - \mathbf{q}_i = \mathbf{H}^{-1}\left(-\frac{\partial V(\mathbf{q}_i)}{\partial \mathbf{q}_i}\right) \tag{V.35}$$

Thus, the LHS is the finite step needed to move from configuration $\mathbf{q}_i$ to the minimum configuration $\mathbf{q}_m$. Subtracting Eq. V.35 at configuration $\mathbf{q}_i$ from the same equation at a new configuration $\mathbf{q}_{i+1}$ gives

$$\mathbf{q}_{i+1} - \mathbf{q}_i = \mathbf{H}^{-1}\left(\frac{\partial V(\mathbf{q}_{i+1})}{\partial \mathbf{q}_{i+1}} - \frac{\partial V(\mathbf{q}_i)}{\partial \mathbf{q}_i} \right) \tag{V.36}$$

The requirement is now imposed that A_{i+1} satisfy Eq. V.36 as if it were truly $\mathbf{H}^{-1}$,

$$\mathbf{q}_{i+1} - \mathbf{q}_i = A_{i+1}\left(\frac{\partial V(\mathbf{q}_{i+1})}{\partial \mathbf{q}_{i+1}} - \frac{\partial V(\mathbf{q}_i)}{\partial \mathbf{q}_i} \right) \tag{V.37}$$

Therefore, a new point $\mathbf{q}_{i+1}$ is given by,

$$\mathbf{q}_{i+1} = \mathbf{q}_i + A_{i+1}\left(\frac{\partial V(\mathbf{q}_i)}{\partial \mathbf{q}_i} - \frac{\partial V(\mathbf{q}_i)}{\partial \mathbf{q}_i} \right) \tag{V.38}$$

where A_{i+1} is the inverse of the updated Hessian at the point $\mathbf{q}_{i+1}$, which can be obtained using the Broyden-Fletcher-Goldfarb-Shanno updating formula[171,173]. This method converges to a minimum much faster than does STEPIT[172] since information about the gradient and Hessian of the potential-energy surface is employed.

Transition-State Structures

Since the Hessian is not posititive-definite, the variable metric method cannot be used to calculate transition-state structures[171]. McIver and Komornicki[174] proposed that a saddle point can be obtained by minimizing the norm of the gradient,

$$\sum_i \left[\left(\frac{\partial V}{\partial x_i}\right)^2 + \left(\frac{\partial V}{\partial y_i}\right)^2 + \left(\frac{\partial V}{\partial z_i}\right)^2 \right], \tag{V.39}$$

where V is the potential energy function, since it is zero at a stationary point on the potential energy surface. This can be achieved using a non-linear least-squares technique. This method will converge directly to the transition state provided the starting point is close to the saddle point. At the transition state, the gradient norm must be zero and not just a minimum. This is a drawback of this method, since the gradient norm can be a minimum at a shoulder in the potential-energy surface. Therefore, caution must be used when searching for transition-state structures.

CHAPTER VI

CONFORMATIONAL STUDY OF GAS-PHASE RDX AT 300 K

Introduction

In this chapter, we have applied molecular dynamic simulation methods in a study of isolated molecules of hexahydro-1,3,5-trinitro-1,3,5-triazine (RDX). The goal of this chapter is to develop a potential-energy surface for gas-phase RDX that is accurate at thermal energies, study the dynamics of conformational changes, and compute the entropy (and free energy) change for the chair-to-boat inversion.

Potential-Energy Surface

An equilibrium potential-energy surface was constructed for a theoretical C_{3v} structure for the chair conformation of the triazine ring by using averaged values of the equilibrium bond lengths of the comparable bonds in the α-RDX crystal structure obtained by Choi and Prince[59], that is, the average value of the six C-N ring bonds in the crystal structure were used for all the C-N bond distances. Since the gas phase RDX molecule is thought to possess C_{3v} symmetry, the values of the ring (C-N-C and N-C-N) and methylene (H-C-H) bond angles were assumed to be tetrahedral. The wag angles, defined as the angle between the plane of the C-N-C atoms of the ring and the N-N bond of the exocyclic NO_2 group, for our potential were set equal to zero[80-81] (see Fig 2). The C-N-C-N ring dihedral angles were set equal to 60° due to the tetrahedral symmetry of the ring bond angles. The C-N-N-O dihedral angles were taken to be 0° as calculated by Orloff *et al.*[79] using CNDO/2. The equilibrium values of all the internal coordinates are

given in Table I. The calculated C_s boat conformation is similar to the chair structure except that the apex atom N(2) is below the plane of the C(1), C(3), N(4), N(5) atoms of the molecule (see Fig. 3a).

The potential-energy surface was constructed,

$$V = V_{bond} + V_{bend} + V_{wag} + V_{torsion}, \tag{VI.1}$$

where the bonds are represented by harmonic potentials (Eq. V.9),

$$V_{bond} = \sum_i \frac{1}{2} k_s (r_i - r_i^o)^2 \tag{VI.2}$$

with k_s and r^o being the harmonic force constant and equilibrium bond distance respectively. The bond angles and wag angles are represented by harmonic potentials (Eqs. V.12 and V.13),

$$V_{bend} = \sum_i \frac{1}{2} k_b (\theta_i - \theta_i^o)^2 \tag{VI.3}$$

and

$$V_{wag} = \sum_i \frac{1}{2} k_\gamma (\gamma_i - \gamma_i^o)^2, \tag{VI.4}$$

with k_b and Θ^o being the bond angle force constant and equilibrium bond-angle respectively, and k_γ and γ^o being the wag angle force constant and equilibrium wag angle respectively. The dihedral angles for the ring C-N-C-N and the exocyclic C-N-N-O dihedral angles are represented by a three-term cosine series (Eq. V.14),

TABLE I

EQUILIBRIUM VALUES OF INTERNAL COORDINATES AND FORCE CONSTANT PARAMETERS FOR THE INTRAMOLECULAR POTENTIAL-ENERGY SURFACE OF RDX

bond	r^o [a]	k_b [b]
C-N	1.454	4.80
N-N	1.380	6.20
N-O	1.210	7.45
C-H	1.081	4.99

bond angle	Θ^o [c]	k_Θ [d]
C-N-C	109.500	0.4898
N-C-N	109.500	0.4030
C-N-N	125.250	0.5713
N-N-O	117.202	0.7008
O-N-O	125.596	0.4003
N-C-H	109.500	0.4570
H-C-H	109.327	0.3874

wag angle	γ^o [c]	k_γ [d]
C-N-C--NO_2	0.00	0.66

dihedral angle	τ^o [c]	a_0 [e]	a_1 [e]	a_2 [e]
C-N-C-N	60.00	0.09	-0.12	0.06

a) Distance units are Å.
b) Stretching force constant units are mdyn $Å^{-1}$.
c) Angle units are degrees.
d) Angle force constants in mdyn Å rad^{-2}.
e) Torsional potential parameter units are eV.
f) Non-bonded interaction parameter units are kcal mol^{-1}.

$$V_{torsion} = \sum_{i} \sum_{j=0}^{2} a_j \cos(j\tau_i). \qquad \text{(VI.5)}$$

where the a_j's are fitting parameters. The values of the potential parameters were obtained from the crystal force field for α-RDX of Trinquecoste *et al.*[64] by transforming the normal force constant matrix to a valence force constant matrix and using only the diagonal elements[169]. The stretching force constants were used unaltered while the bond angle force constants were divided by one half[175]. The force constants for the torsional potential of the crystal were not used because they are expected to be influenced by the crystal lattice and thus would not be appropriate for an isolated molecule. Therefore, the parameters for the C-N-C-N dihedral angles of the triazine ring were obtained by fitting the barrier calculated by Allinger[175] for aliphatic amines using the MM2 method[84]. This involves substituting a nitrogen atom in the place of a carbon atom for the C-C-C-N potential of piperidine. Vladimiroff[83] used this method to study heats of formation and dipole moments for RDX and achieved satisfactory results. The torsional potential is intimately involved in the conformational dynamics and thus the lack of data for torsional barriers in cyclic nitramines is unfortunate. However, the potentials we use should be adequate.

Filhol *et al.*[80] used INDO to calculate the most stable configuration of the $C_2N—NO_2$ groups. Their calculation showed that the most stable configuration is achieved when the nitro group is planar with respect to the C-N-C atoms in the ring (see Fig. 2). Planarity at the amine nitrogen was also observed by Politzer *et al* [81-82] in *ab initio* calculations for small nitramines. The INDO calculation[84] showed that the restoring force for the wag angle potential is very weak, that is, ~ 1.0 kcal/mol for 10 degrees out of the $C_2N—NO_2$ plane. To obtain a C-N-N-O torsional barrier, we used the value calculated by the semi-emperical technique CNDO/2 which gave a rotational barrier of 10 kcal/mol for the exocyclic NO_2 group[79]. The values of the potential parameters are given in Table I.

The experimental and calculated normal-mode frequencies are compared in Table II. The calculated normal-mode frequencies were obtained from the analytical second derivatives of the potential-energy surface. The experimental frequencies are for RDX in the solution phase[66]. The solution and gas phase spectra are expected to be similar and there are no complete gas phase spectra for RDX. Experimental values for the torsional frequencies are not available for comparison. The average root mean square (<rms>) deviation between the experimental and the calculated frequencies for the chair structure is 33 cm^{-1}.

Conformational changes sometimes involve motion of more than one internal coordinate. We use the Cremer-Pople pucker coordinates[176-177] to describe the different conformations of the ring atoms of RDX (see appendix B for a complete derivation). For a six membered ring, the three puckering degrees of freedom can be represented by a set of "spherical polar" coordinates, Q, Θ, and Φ given by

$$\cos\Theta = \frac{\frac{1}{\sqrt{6}}\sum_{i=1}^{6} z_i \cos[\pi(i-1)]}{Q}, \tag{VI.6}$$

$$-\tan\Phi = \frac{\sum_{i=1}^{6} z_1 \sin\left[\frac{2}{3}\pi(i-1)\right]}{\sum_{i=1}^{6} z_1 \cos\left[\frac{2}{3}\pi(i-1)\right]}, \tag{VI.7}$$

and

$$Q^2 = \sum_{i=1}^{6} z_i^2, \tag{VI.8}$$

TABLE II

EXPERIMENTAL AND CALCULATED FREQUENCIES FOR THE CHAIR AND BOAT STRUCTURES OF RDX[a]

Experimental[b]	Calculated[c]		
	Chair		Boat
			7
——	47	(2)	48
——	61		66
——	147	(2)	137
——	——		143
——	——		174
——	191		185
——	205	(2)	201
——	210		208
——	237	(2)	232
——	——		255
——	287		261
——	——		395
——	411	(2)	412
——	——		415
——	422	(2)	441
——	——		458
410	425		482
470	471		538
490	591		574
595	627	(2)	609
610	719	(2)	719
——	——		723
——	——		740
740	759		784
750	774	(2)	799
794	872		857
855	944	(2)	943
——	——		982
910	969		994
935	1041	(2)	1005
——	——		1023
1015	1049		1048
1045	1054		1059
1230	1131	(2)	1132

TABLE II (Continued)

Experimental[b]	Calculated[c] Chair		Calculated[c] Boat	
----	----		1137	
1270	1271		1270	(2)
1320	1272	(2)	1275	
1392	1350	(2)	1342	
----	----		1347	
1435	1414		1410	
1460	1497		1494	
1550	1544	(2)	1547	(2)
1585	1568	(3)	1567	(3)
2980	2985	(3)	2985	(3)
3080	3062	(3)	3061	(3)

a) Units are cm^{-1}
b) Iqbal *et al.*, Ref. 66
c) This work.

with Q being the single puckering amplitude. The sum is over the six atoms of the ring and the z_i's are the atomic displacements of the ring atoms from a mean plane that passes through the geometrical center of the triazine ring. The exocyclic atoms have no influence on the definition of the pucker coordinates.

The different conformations of the triazine ring, i.e., the chair, boat, and twist, are located at specific positions defined by the coordinates Θ and Φ on the surface of a sphere of radius Q. The chair structure is located at Θ=0° or 180° with Φ being undefined since the chair structure is located at the pole of the sphere. Rotating the polar angle Θ from 0° to 90° describes the chair-to-boat ring inversion. At the equator of the sphere (Θ = 90°), as the azimuthal angle rotates between 0 and 2π, the triazine ring experiences all the different boat and twist conformations. The different boat and twist conformers (Θ=90°) are located at Φ = 0, 60, 120, 180, 240, and 300° and Φ = 30, 90, 150, 210, 270, and 330°, respectively. As the polar angle continues for 90° to 180°, the ring undergoes inversion from the boat to the inverted chair structure.

The potential energy of the RDX molecule in the chair, boat, and twist-boat conformations was minimized using the program STEPIT[172]. The minimum energy structures are shown in Figs. 2, 3a, and 3b for the chair, boat, and twist conformations respectively. The boat (Θ=90°, Φ=0°) and twist-boat (Θ=90°, Φ=30°) structures are equal in energy and 1.3 kcal mol^{-1} higher in potential energy than the chair (Θ=0°, Φ=0°) structure. To locate the transition states between the chair and boat or twist structures, trajectories which experienced ring inversions where followed and the norm of the gradient (Eq.V.39) was minimized, using a conjugate gradient nonlinear-least squares technique, at points along the trajectories. The gradient norm was minimized to better then $5x10^{-3}$ to determine the local minima and maxima. Figures 5a and 5b show the transition state structures for the chair-to-boat and chair-to-twist inversions, respectively. The transition state for the chair-to-boat inversion is located at Θ = 57.7° and Φ = 181.6° (Fig. 5a). The barrier calculated for this inversion path is 4.72 kcal mol^{-1} and the structure at the barrier is

Figure 5. Half-boat and Half-chair Transition-state Structures of RDX. (a) The half-boat structure is 4.72 kcal mol^{-1} higher in energy than the chair structure. Atoms C(1), C(3), N(4), C(5), and N(6) lie in a plane. (b) The half-chair structure is 4.72 kcal mol^{-1} higher in energy than the chair structure. Atoms C(3), N(4), C(5), and N(6) lie in a plane. The atom types are the same as in Figure 2, but the molecules have been rotated for clarity.

a

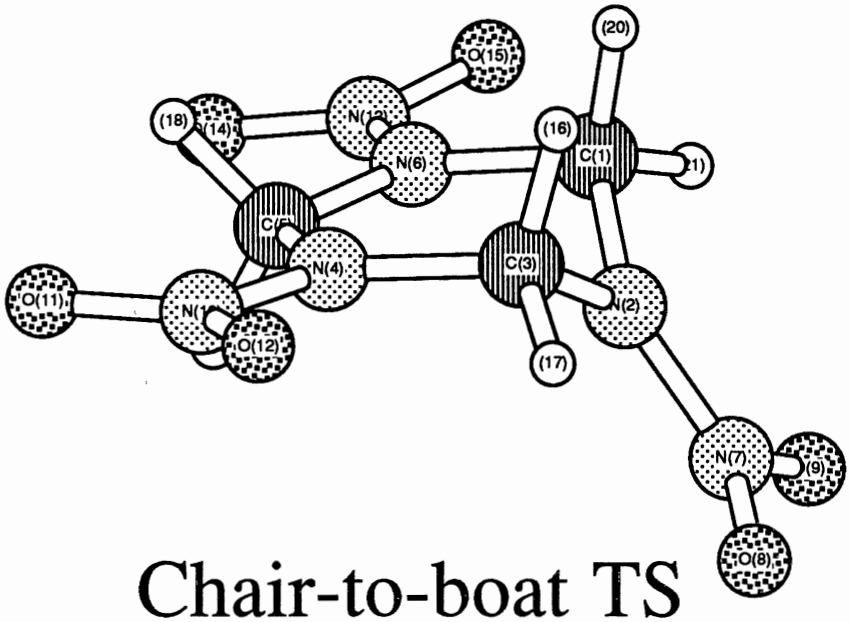

Chair-to-boat TS

b

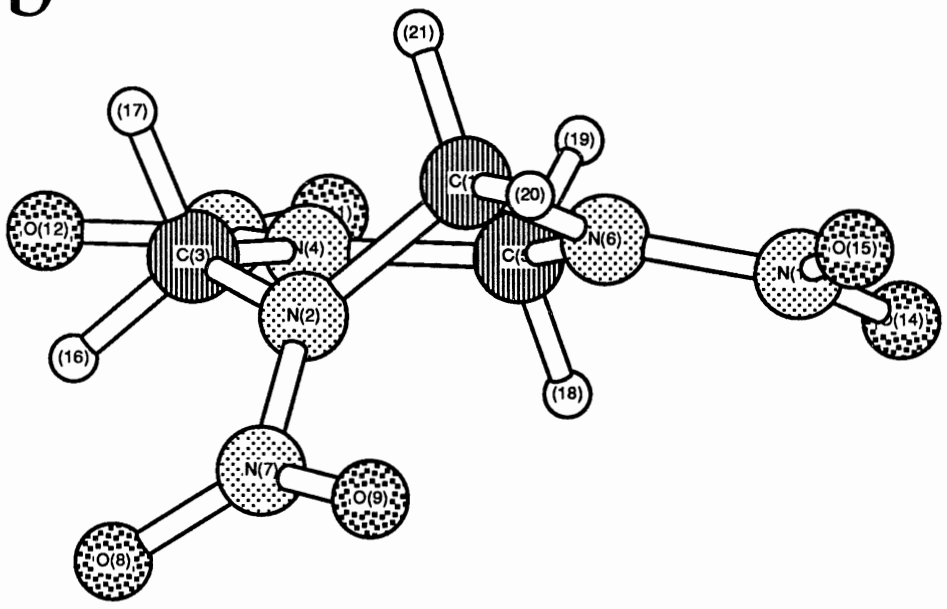

Chair-to-twist TS

of C_s (half-boat) symmetry. Figure 5b illustrates the structure at the transition state for the chair-to-twist-boat inversion, $\Theta = 56.7°$ and $\Phi = 152.7°$. The barrier is 4.76 kcal mol^{-1} for this C_1 (half-chair) structure.

The internal coordinates for the minima and transition states are given in Table III. Unfortunately, there are no experimental gas-phase values with which to compare these results but we can compare our minimized structures with the α-crystal structure[59].

Procedures

Two ensembles at 300 K were calculated using the methods described in chapter V. One ensemble initiated the RDX molecule in the chair conformation (I) while the second ensemble corresponds to the RDX molecule initially in the boat conformation (II). A 100 ps warm-up trajectory was calculated for each ensemble. The trajectories were integrated for 20 ps after 20 ps of equilibration. Due to the small number of the atoms present in the RDX system and the exchange between potential and kinetic energy, fluctuations in the instantaneous temperature were observed. Because of these fluctuations, scaling each trajectory to a certain temperature is almost impossible. Therefore, some deviation from the ensemble temperature must be accepted for each individual trajectory. Any trajectory whose average temperature deviated by more than 10 K from the desired ensemble temperature was rejected. The ensemble temperature for I and II are 302 ± 5 and 300 ± 5 K, respectively. For each run, an ensemble of 10 trajectories were calculated which gave 200 ps of dynamics.

A Runge-Kutta-Gill fourth order numerical integrator was used to solve the equations of motion with a fixed step size of 1.2×10^{-16} s. This step size gave energy conservation of 1×10^{-4} relative percent error.

TABLE III

INTERNAL COORDINATES FOR THE MINIMUM AND TRANSITION-STATE STRUCTURES OF RDX[a]

Coordinate	Crystal[b]	Chair[c]	Half-boat[d]	Boat[e]	Half-chair[f]	Twist
Bond:[g]						
C(1)-N(2)	1.46	1.454	1.452	1.454	1.446	1.454
N(2)-C(3)	1.46	1.454	1.450	1.454	1.446	1.453
C(3)-N(4)	1.46	1.454	1.458	1.454	1.454	1.454
N(4)-C(5)	1.46	1.454	1.455	1.454	1.462	1.454
C(5)-N(6)	1.46	1.454	1.456	1.453	1.461	1.453
N(6)-C(1)	1.46	1.454	1.454	1.454	1.452	1.454
N(2)-N(7)	1.35	1.380	1.381	1.380	1.380	1.380
N(4)-N(10)	1.35	1.380	1.378	1.380	1.380	1.380
N(6)-N(13)	1.35	1.380	1.379	1.380	1.380	1.380
N(7)-O(8)	1.23	1.210	1.210	1.210	1.210	1.210
N(7)-O(9)	1.23	1.210	1.210	1.210	1.210	1.210
N(10)-O(11)	1.23	1.210	1.210	1.210	1.210	1.210
N(10)-O(12)	1.23	1.210	1.210	1.210	1.210	1.210
N(13)-O(14)	1.23	1.210	1.210	1.210	1.210	1.210
N(13)-O(15)	1.23	1.210	1.210	1.210	1.210	1.210
C(1)-H(20)	1.09	1.081	1.081	1.081	1.081	1.081
C(1)-H(21)	1.09	1.081	1.081	1.081	1.081	1.081
C(3)-H(16)	1.09	1.081	1.081	1.081	1.081	1.081
C(3)-H(17)	1.09	1.081	1.082	1.081	1.081	1.081
C(5)-H(18)	1.09	1.081	1.081	1.081	1.081	1.081
C(5)-H(19)	1.09	1.081	1.081	1.081	1.081	1.081
Bond angle:[h]						
C(1)-N(2)-C(3)	115.1	109.50	107.24	109.50	106.45	109.38
N(2)-C(3)-N(4)	108.3	109.50	113.54	109.50	110.94	109.37
C(3)-N(4)-C(5)	115.1	109.50	116.29	109.50	115.16	109.76
N(4)-C(5)-N(6)	108.3	109.50	120.35	109.50	121.16	109.52
C(5)-N(6)-C(1)	115.1	109.50	112.81	109.50	114.38	109.47
N(6)-C(1)-N(2)	108.3	109.50	106.76	109.50	109.41	109.80
C(1)-N(2)-N(7)	119.7	125.25	126.39	125.25	126.77	125.31
C(3)-N(2)-N(7)	119.7	125.25	126.37	125.25	126.77	125.31
N(2)-N(7)-O(8)	117.2	117.20	117.18	117.20	117.08	117.12
N(2)-N(7)-O(9)	117.2	117.20	117.19	117.20	117.08	117.12
O(8)-N(7)-O(9)	125.0	125.60	125.56	125.60	125.38	125.45
C(3)-N(4)-N(10)	119.7	125.25	121.85	125.25	122.42	125.12
C(5)-N(4)-N(10)	119.7	125.25	121.86	125.25	122.41	125.12
N(4)-N(10)-O(11)	117.2	117.20	117.12	117.20	117.16	117.19
N(4)-N(10)-O(12)	117.2	117.20	117.12	117.20	117.16	117.18
O(11)-N(10)-O(12)	125.0	125.60	125.45	125.60	125.52	125.57
C(5)-N(6)-N(13)	119.7	125.25	123.60	125.25	122.81	125.26
C(1)-N(6)-N(13)	119.7	125.25	123.60	125.25	122.81	125.26
N(6)-N(13)-O(14)	117.2	117.20	117.19	117.20	117.14	117.03
N(6)-N(13)-O(15)	117.2	117.20	117.19	117.20	117.14	117.02
O(14)-N(13)-O(15)	125.0	125.60	125.58	125.60	125.48	125.29
N(2)-C(3)-H(16)	109.6	109.50	108.70	109.50	109.22	109.52
N(2)-C(3)-H(17)	109.6	109.50	108.68	109.50	109.22	109.52

TABLE III (Continued)

Coordinate	Crystal	Chair	Half-boat	Boat	Half-chair	Twist
N(4)-C(3)-H(16)	109.6	109.50	108.70	109.50	109.22	109.52
N(4)-C(3)-H(17)	109.6	109.50	108.67	109.50	109.22	109.52
H(16)-C(3)-H(17)	108.7	109.32	108.43	109.32	109.00	109.36
N(4)-C(5)-H(18)	109.6	109.50	107.19	109.50	107.01	109.50
N(4)-C(5)-H(19)	109.6	109.50	107.21	109.50	107.01	109.49
N(6)-C(5)-H(18)	109.6	109.50	107.19	109.50	107.01	109.50
N(6)-C(5)-H(19)	109.6	109.50	107.21	109.50	107.01	109.50
H(18)-C(5)-H(19)	108.7	109.32	107.05	109.32	106.90	109.32
N(6)-C(1)-H(20)	109.6	109.50	110.01	109.50	109.52	109.44
N(6)-C(1)-H(21)	109.6	109.50	110.02	109.50	109.51	109.43
N(2)-C(1)-H(20)	109.6	109.50	110.01	109.50	109.52	109.45
N(2)-C(1)-H(21)	109.6	109.50	110.02	109.50	109.51	109.43
H(20)-C(1)-H(21)	108.7	109.32	109.96	109.32	109.35	109.26
Wag angle:						
C(1)-N(2)-C(3)--N(7)	19.8	0.00	0.00	0.00	0.00	-0.03
C(3)-N(4)-C(5)--N(10)	-33.9	0.00	0.02	0.00	0.00	-0.02
C(5)-N(6)-C(1)--N(13)	-33.4	0.00	0.03	0.00	0.01	-0.03
Dihedral angle:						
C(1)-N(2)-C(3)-N(4)	-57.2	-60.00	55.97	60.00	67.07	70.32
N(2)-C(3)-N(4)-C(5)	51.9	60.00	-13.82	0.00	-28.20	-36.92
C(3)-N(4)-C(5)-N(6)	-49.2	-60.00	-9.63	-60.00	-5.80	-29.20
N(4)-C(5)-N(6)-C(1)	49.4	60.00	-9.77	60.00	1.39	69.91
C(5)-N(6)-C(1)-N(2)	-52.1	-60.00	51.16	0.00	36.59	-36.52
N(6)-C(1)-N(2)-C(3)	57.4	60.00	-75.68	-60.00	-71.60	-29.57
C(1)-N(2)-N(7)-O(9)	-10.1	0.00	-0.02	0.00	-0.09	0.12
C(3)-N(4)-N(10)-O(12)	-10.1	0.00	-0.07	0.00	-0.02	0.12
C(5)-N(6)-N(13)-O(14)	-10.1	0.00	0.04	0.00	-0.02	0.14

a) Atom numbers are defined in Fig. 1.
b) Values taken from Ref. 59.
c) Equilibrium C_{3v} structure.
d) Transition-state between the chair and boat conformations.
e) Equilibrium C_s structure.
f) Transition-state between the chair and twist conformations.
g) Bond length units are Å.
h) Angle units are deg.

Results and Discussion

Due to the small number of atoms in RDX, the validity of the definition of a temperature (Eq. V.23), defined as the time averaged kinetic energy of all the atoms in the system was confirmed by comparing the distribution of atomic speeds from an ensemble of trajectories with the Maxwell distribution corresponding to the temperature of that ensemble. The Maxwellian speed distribution can be derived from the Maxwell-Boltzmann distribution of velocity components[178] and is given by,

$$dF(v) = 4\pi \left(\frac{m}{2\pi\kappa T}\right)^{3/2} v^2 \exp\left[\frac{-mv^2}{2\kappa T}\right], \qquad \text{(VI.9)}$$

where dF(v) is the probability of a speed being between v→v+dv, m is the mass of the atom, and κ and T are the Boltzmann constant and temperature, respectively. The most probable speed is $v_{max} = \sqrt{2\kappa T/m}$. The speed of each atom for a given type was calculated,

$$v_i = \frac{1}{m_i}\left[P_{x_i}^2 + P_{y_i}^2 + P_{z_i}^2\right]^{\frac{1}{2}}, \qquad \text{(VI.10)}$$

where P_{x_i}, P_{y_i}, and P_{z_i} are the Cartesian momenta and m_i is the mass of the ith atom, at each step during the 200 ps of dynamics and histograms at 15-20 equal subintervals were obtained. Figures 6-9 shows the distribution for the four different atom types, C, N, O, and H. The Maxwell-Boltzmann distribution was calculated at 300 K and is illustrated for comparison with the trajectory data. As can be seen, the Maxwellian distribution represents the data well.

Dynamic Structures

The dynamically averaged internal coordinates of RDX for ensemble I are shown in Table IV and are compared to the theoretical C_{3v} equilibrium structure (see Fig. 2). The

Figure 6. Distribution Of Speeds For The Carbon Atoms Of RDX At 300 K.

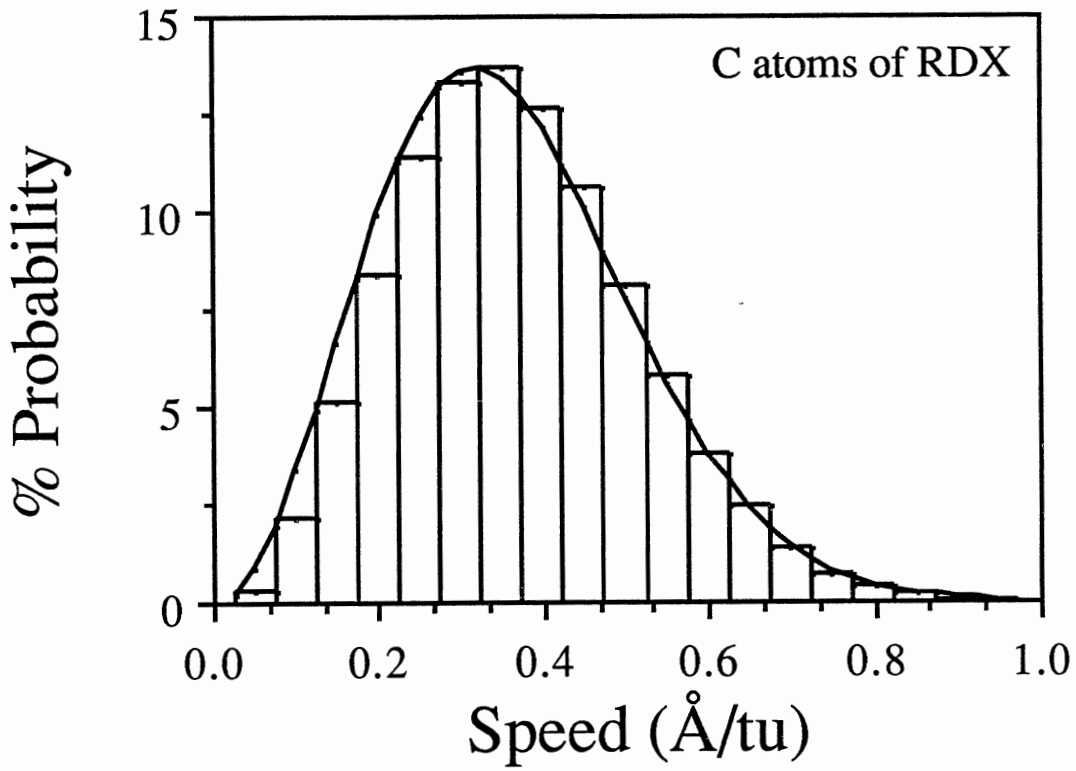
C atoms of RDX
% Probability
15
10
5
0
0.0
0.2
0.4
0.6
0.8
1.0
Speed (Å/tu)

Figure 7. Distribution Of Speeds For The Nitrogen Atoms Of RDX At 300 K.

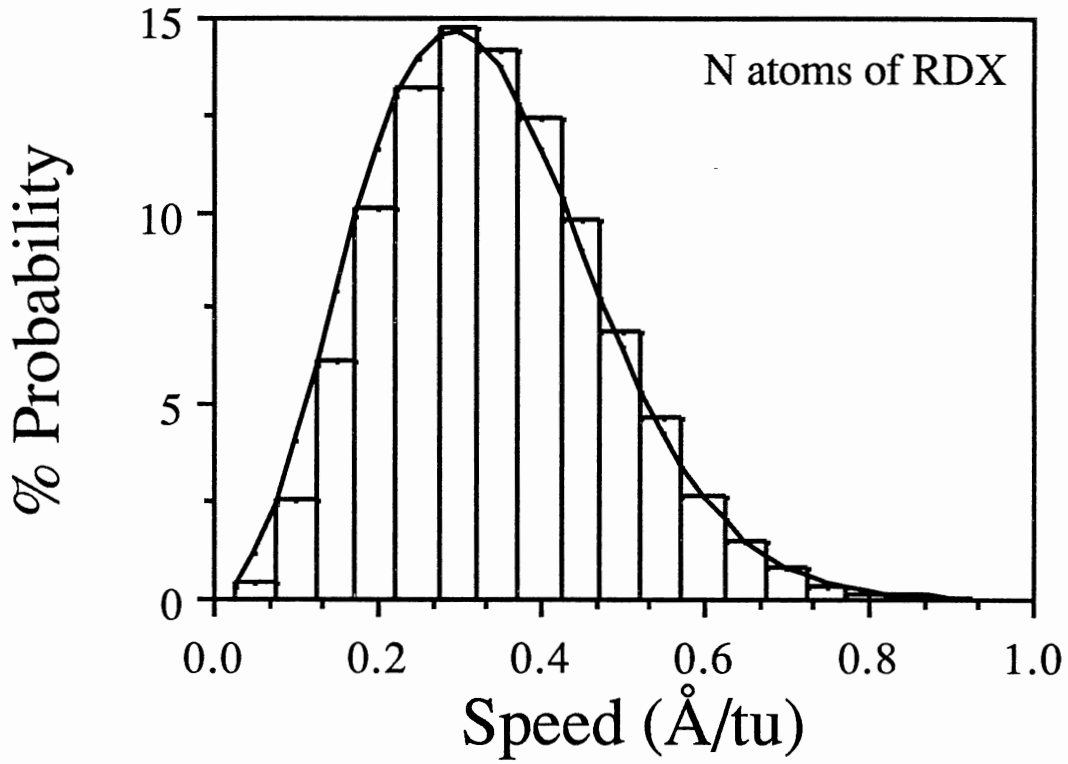
N atoms of RDX
% Probability
15
10
5
0
0.0
0.2
0.4
0.6
0.8
1.0
Speed (Å/tu)

Figure 8. Distribution Of Speeds For The Oxygen Atoms Of RDX At 300 K.

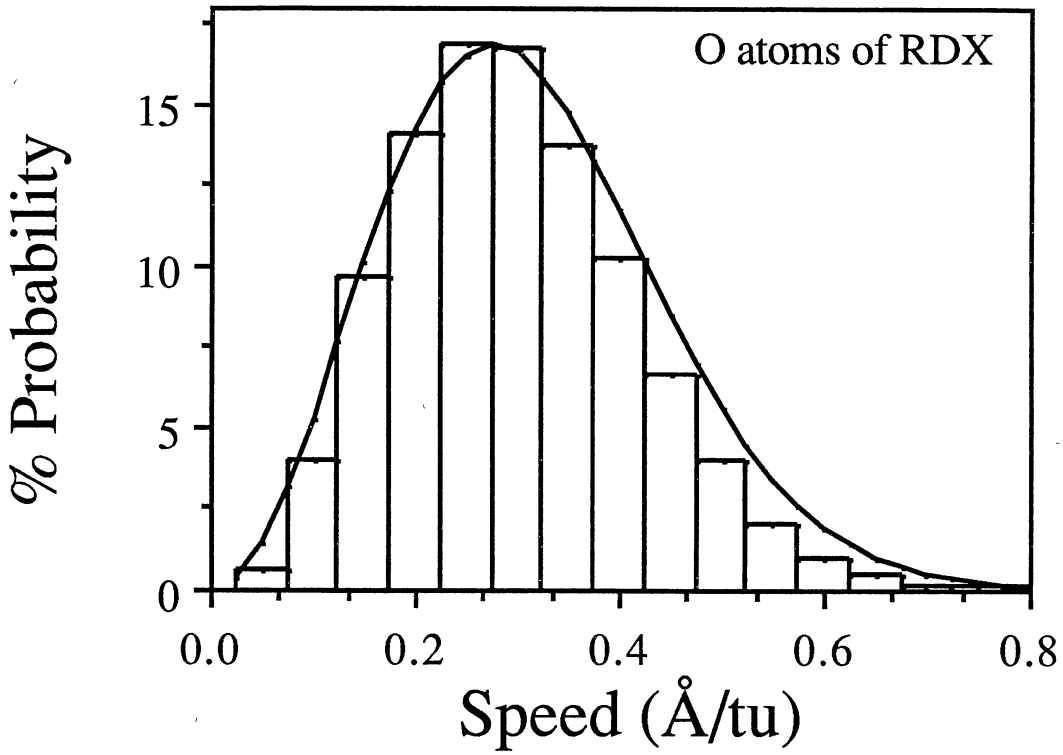
O atoms of RDX
% Probability
15
10
5
0
0.0
0.2
0.4
0.6
0.8
Speed (Å/tu)

Figure 9. Distribution Of Speeds For The Hydrogen Atoms Of RDX At 300 K.

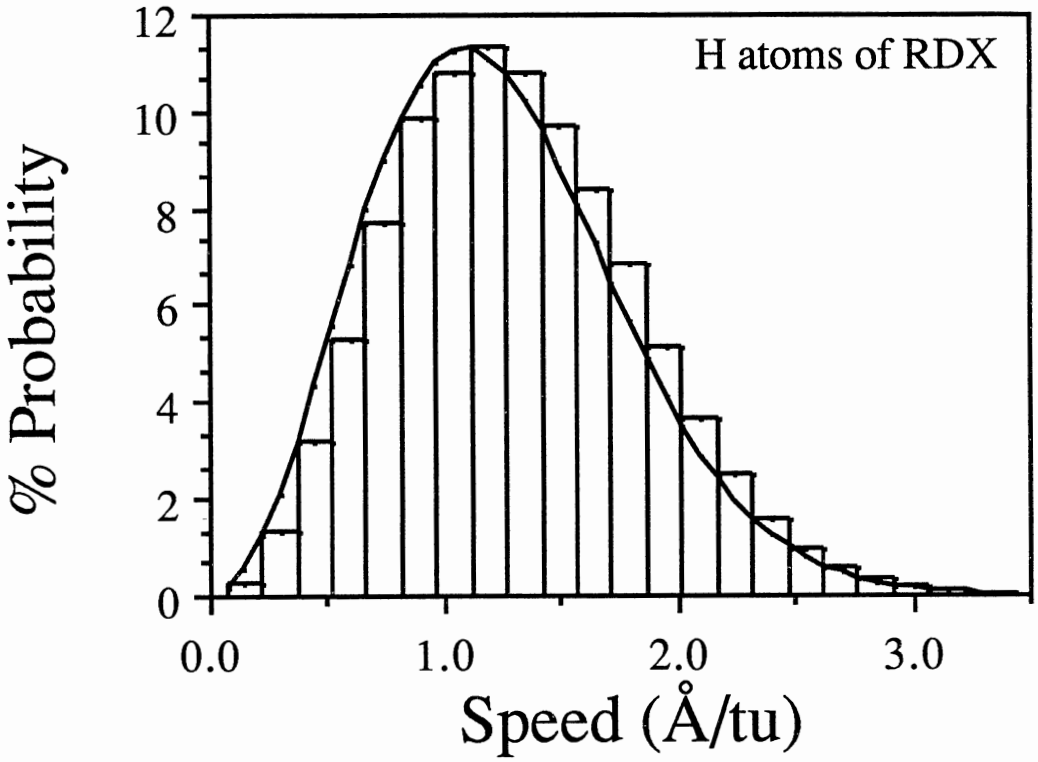
H atoms of RDX
% Probability
12
10
8
6
4
2
0
0.0
1.0
2.0
3.0
Speed (Å/tu)

dynamically averaged bonds are very close to the equilibrium values with small fluctuations. The mean value of the bending angles, both the bond and wag angles, are close to the equilibrium values but have larger deviations with the largest being in the H-C-H bond angles. The time averaged ring dihedral angles of the chair structure are very close to the equilibrium value of 60° (see Table I), but as the results in Table IV show, the mean C-N-C-N dihedral angle is 58° which results in a ring structure that is less puckered then the equilibrium structure. The time averaged values of the pucker coordinates are Q=0.50Å ± 0.033Å and Θ=9.2°± 4.8°. The values of the pucker coordinates for the equilibrium chair structure are Q=0.5927Å and Θ=0.0°. The decrease in the mean value of Q compared with the equilibrium value illustrates the flattening of the ring to a less puckered structure. This result is due mainly to the large anharmonicity in the torsional coordinate. The calculated C-N-N-O dihedral angles show large fluctuations but do not traverse the 10 kcal/mol rotational barrier.

The dynamically averaged structure of RDX for ensemble II is given in Table V. The rms deviations of the internal coordinates for ensemble II are very close to the corresponding internal coordinates of ensemble I except for the time averaged ring dihedral angles which have mean values of ~ 0° and rms values of ~ 48°. The time averaged values of the pucker coordinates for II are Q=0.78Å±0.048Å, Θ=9.2°±4.8°, and Φ=191.0°±103.6°. These values can be compared to the corresponding values for the equilibrium boat conformation of 0.791Å, 90.0°, and 0.0° for Q, Θ, and Φ, respectively. The large deviation in the Φ coordinate is due to a relatively unhindered pseudorotation between the different boat and twist conformations.

The conformational flexibility of RDX is monitored by using the Cremer-Pople puckering coordinates. The chair, boat, half-boat, half-chair and twist-boat conformations of the triazine ring can be described by two coordinates, Θ and Φ. The time histories of the pucker coordinates Θ and Φ for ring inversion in RDX initially in the chair conformation are shown in Figs. 10(a-b). The molecule remains in the chair potential-

TABLE IV

MEAN STRUCTURE OF RDX IN THE CHAIR CONFORMATION AT 300 K[a]

Coordinate	Equilibrium value	Mean value from dynamics	<rms> deviation
Bond:[b]			
C(1)-N(2)	1.45	1.45	0.03
N(2)-N(7)	1.38	1.38	0.03
N(7)-O(8)	1.21	1.21	0.02
C(3)-H(16)	1.08	1.08	0.02
Bond angle:[c]			
C(1)-N(2)-C(3)	109.5	109.5	3.98
N(2)-C(3)-N(4)	109.5	109.7	4.84
C(1)-N(2)-N(7)	125.3	125.1	3.70
N(2)-N(7)-O(8)	117.2	116.1	3.76
O(8)-N(7)-O(9)	125.6	123.7	4.67
N(2)-C(3)-H(16)	109.5	109.3	4.51
H(16)-C(3)-H(17)	109.3	109.1	4.98
Wag angle:			
C(1)-N(2)-C(3)--N(7)	0.0	-0.2	4.37
Dihedral angle:			
C(1)-N(2)-C(3)-N(4)	-60.0	-58.4	9.58
N(2)-C(3)-N(4)-C(5)	60.0	58.3	9.05
C(3)-N(4)-C(5)-N(6)	-60.0	-58.4	8.88
N(4)-C(5)-N(6)-C(1)	60.0	58.4	9.03
C(5)-N(6)-C(1)-N(2)	-60.0	-58.4	8.56
N(6)-C(1)-N(2)-C(3)	60.0	58.4	8.98
C(1)-N(2)-N(7)-O(9)	0.0	-0.3	9.07

a) Representative internal coordinates are listed (atom numbers are defined in Fig. 2).
b) Bond length units are Å.
c) Angle units are deg.

TABLE V

MEAN STRUCTURE OF RDX IN THE BOAT/TWIST CONFORMATION AT 300 K[a]

Coordinate	Equilibrium value	Mean value from dynamics	<rms> deviation
Bond:[b]			
C(1)-N(2)	1.45	1.46	0.03
N(2)-N(7)	1.38	1.38	0.02
N(7)-O(8)	1.21	1.21	0.02
C(3)-H(16)	1.08	1.08	0.03
Bond angle:[c]			
C(1)-N(2)-C(3)	109.5	109.6	3.82
N(2)-C(3)-N(4)	109.5	109.6	4.66
C(1)-N(2)-N(7)	125.3	125.1	3.81
N(2)-N(7)-O(8)	117.2	116.1	3.69
O(8)-N(7)-O(9)	125.6	123.5	4.80
N(2)-C(3)-H(16)	109.5	109.4	4.60
H(16)-C(3)-H(17)	109.3	109.1	4.54
Wag angle:			
C(1)-N(2)-C(3)--N(7)	0.0	0.1	4.51
Dihedral angle:			
C(1)-N(2)-C(3)-N(4)	60.0	-0.6	46.31
N(2)-C(3)-N(4)-C(5)	0.0	-8.6	49.39
C(3)-N(4)-C(5)-N(6)	-60.0	9.4	49.75
N(4)-C(5)-N(6)-C(1)	60.0	-1.7	46.27
C(5)-N(6)-C(1)-N(2)	0.0	-7.6	48.73
N(6)-C(1)-N(2)-C(3)	-60.0	8.3	49.03
C(1)-N(2)-N(7)-O(9)	0.0	-0.2	9.17

a) Representative internal coordinates are listed (atom numbers are defined in Fig. 2).
b) Bond length units are Å.
c) Angle units are deg.

energy well for the first 8 ps (Fig. 10a), after which it undergoes three transitions between the chair and boat structures over the next 6 ps. Figure 11 illustrates, in Θ and Φ space, the final 12 ps of the ring inversion shown in Fig. 10(a-b). The first ring inversion is through Φ=45°, which is between the half-chair (Φ=30°) and the half-boat (Φ=60°) structures. The following two inversions occur through Φ=180°, which corresponds to the half-boat structure. Two of transitions are fairly direct while the third is not. Only two trajectories in the chair ensemble were observed to undergo ring inversion.

A time history of RDX initially in the boat configuration undergoing a boat-to-chair transition is shown in Fig. 12(a-b). As can be seen, the ring undergoes a transition from the boat to the inverted-chair structure (see Fig. 12a) after 2 ps and remains in the inverted-chair conformation for the remaining 18 ps. During the initial 2 ps, the molecule undergoes 5 transitions between different boat and twist structures (Φ = 240, 210, 180, 150, and 120°). These relatively unhindered pseudorotations play a major role in the stability of the boat/twist conformations (Θ= 0°) compared with that of the chair conformation (Θ= 0°) as will be shown later. Figure 13 illustrates, in Θ and Φ space, the initial 2.1 ps of the trajectory shown in Fig. 12(a-b). The observed transitions is fairly indirect. Only one trajectory out of the 10 calculated for the boat ensemble was observed to undergo a boat-to-chair transition.

A time history of a trajectory starting in the boat configuration that does not undergo a ring inversion is shown in Fig. 14. The triazine ring remains at Θ=90° (Fig. 14a) for the 20 ps that the trajectory was followed, but relatively unhindered pseudorotations between the different boat (Φ = 0, 60, 120, 180, 240, and 300°) and twist (Φ = 30, 90, 150, 210, 270, and 330°) conformers are observed (Fig. 14b). The discontinuities Fig. 14b are due to the azimuthal angle being defined between 0° and 360°.

Figure 10. Time History of the Cremer-Pople Coordinates for a Trajectory that Undergoes a Chair-to-Boat Ring Inversion. (a) Θ (deg), and (b) Φ (deg)

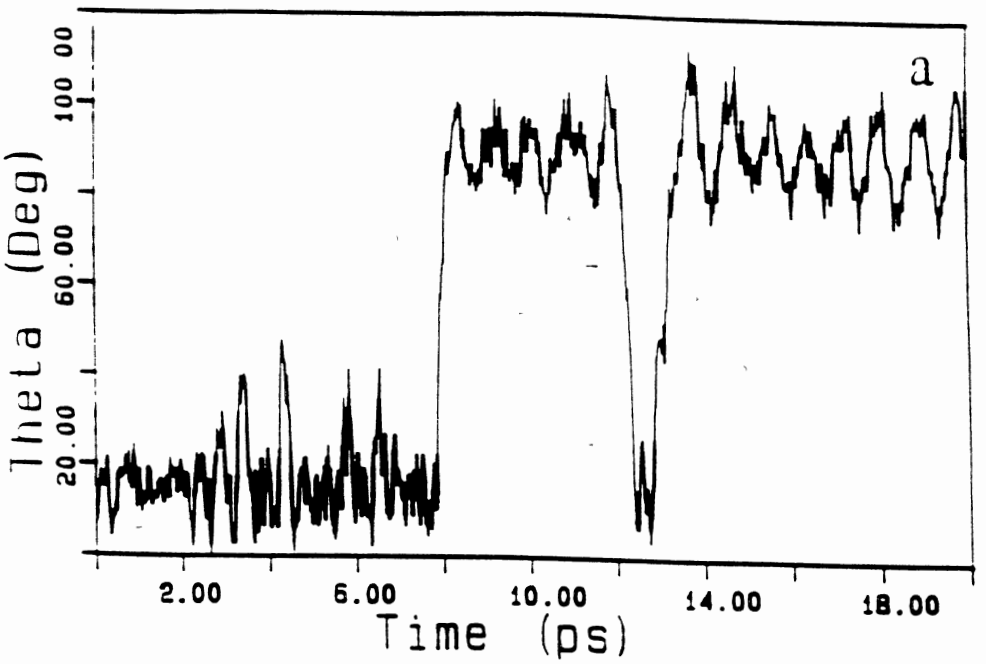
a
Theta (Deg)
100.00
60.00
20.00
2.00
6.00
10.00
14.00
18.00
Time (ps)

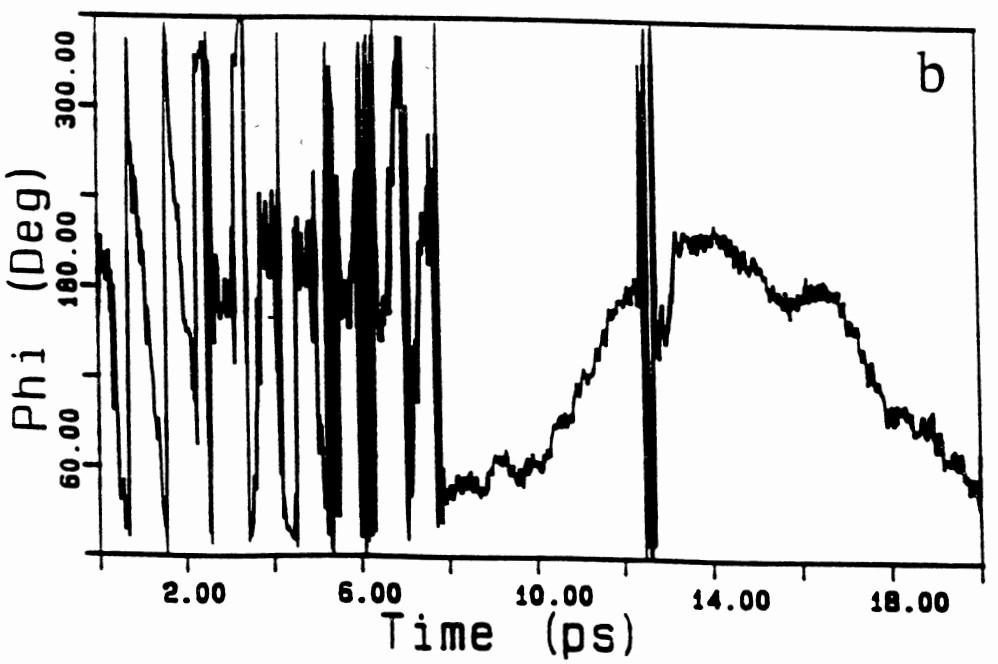
b
Phi (Deg)
300.00
180.00
60.00
2.00
6.00
10.00
14.00
18.00
Time (ps)

Figure 11. Configuration Space Plot of the Pucker Coordinates Θ and Φ for the Trajectory Represented In Figure 10. Only the final 12 ps of the trajectory are shown. units are in degrees.

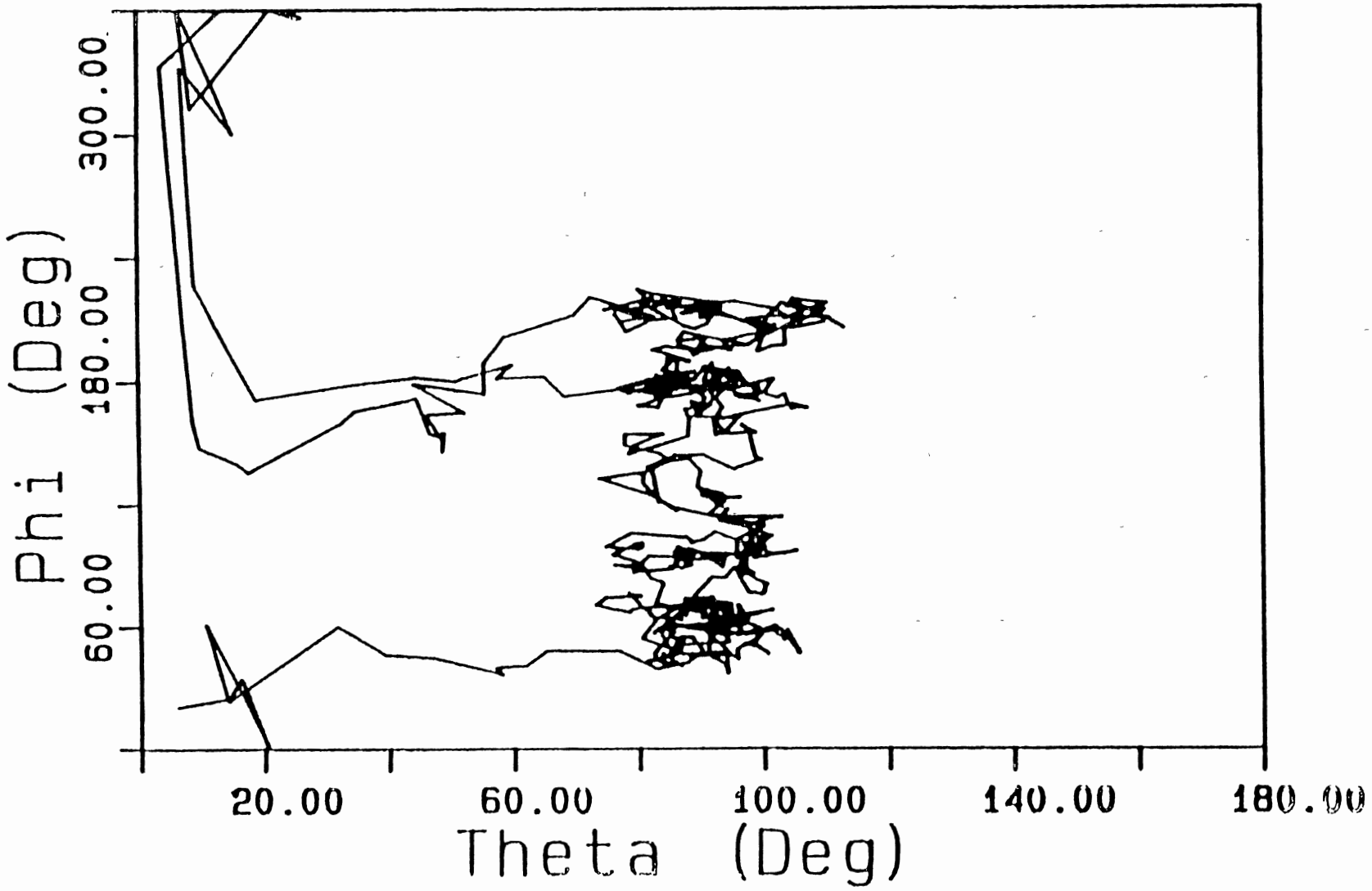
Phi (Deg)
300.00
180.00
60.00
20.00
60.00
100.00
140.00
180.00
Theta (Deg)

Figure 12. Time History of the Cremer-Pople Coordinates for a Trajectory that Undergoes a Boat-to-Chair Ring Inversion. (a) Θ (deg), and (b) Φ (deg).

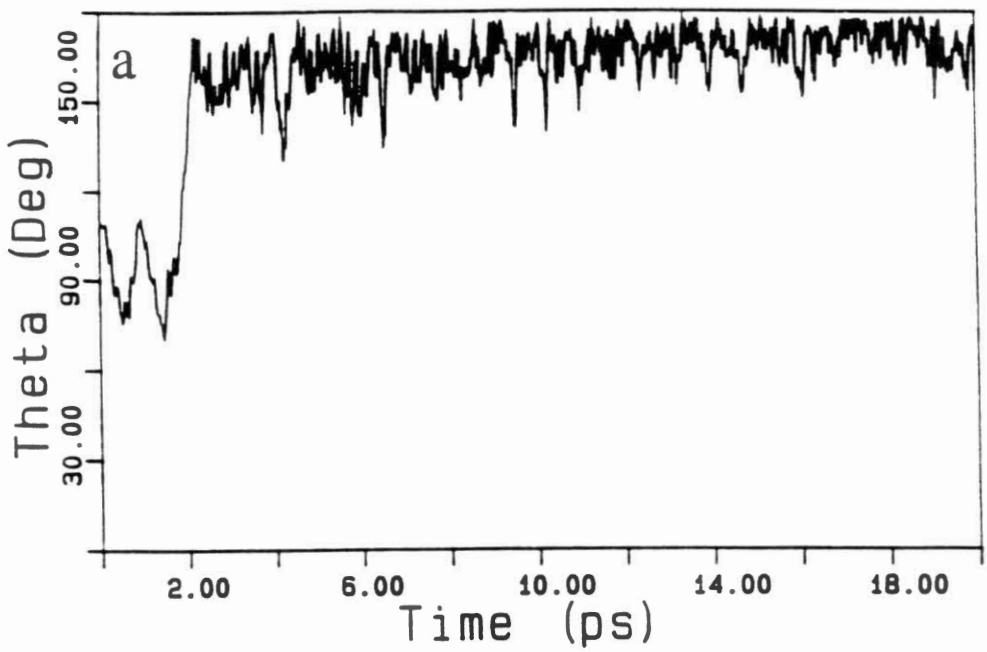
a
Theta (Deg)
150.00
90.00
30.00
2.00
6.00
10.00
14.00
18.00
Time (ps)

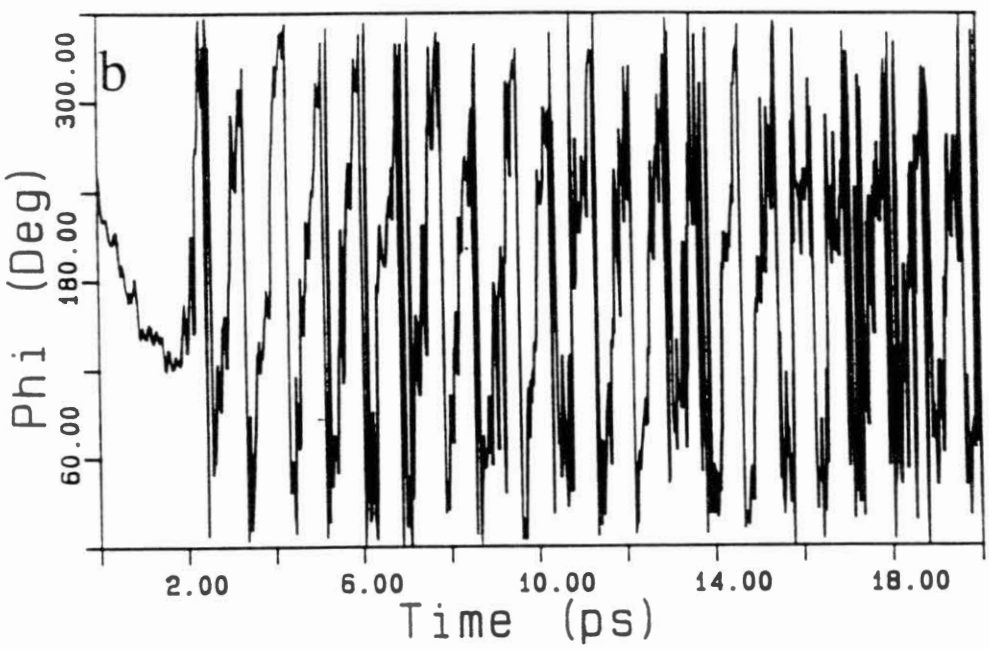
b
Phi (Deg)
300.00
180.00
60.00
2.00
6.00
10.00
14.00
18.00
Time (ps)

Figure 13. Configuration Space Plot Of The Pucker Coordinates Θ and Φ For The Trajectory Represented In Figure 12. Only the initial 12 ps of the trajectory are shown. Units are in degrees.

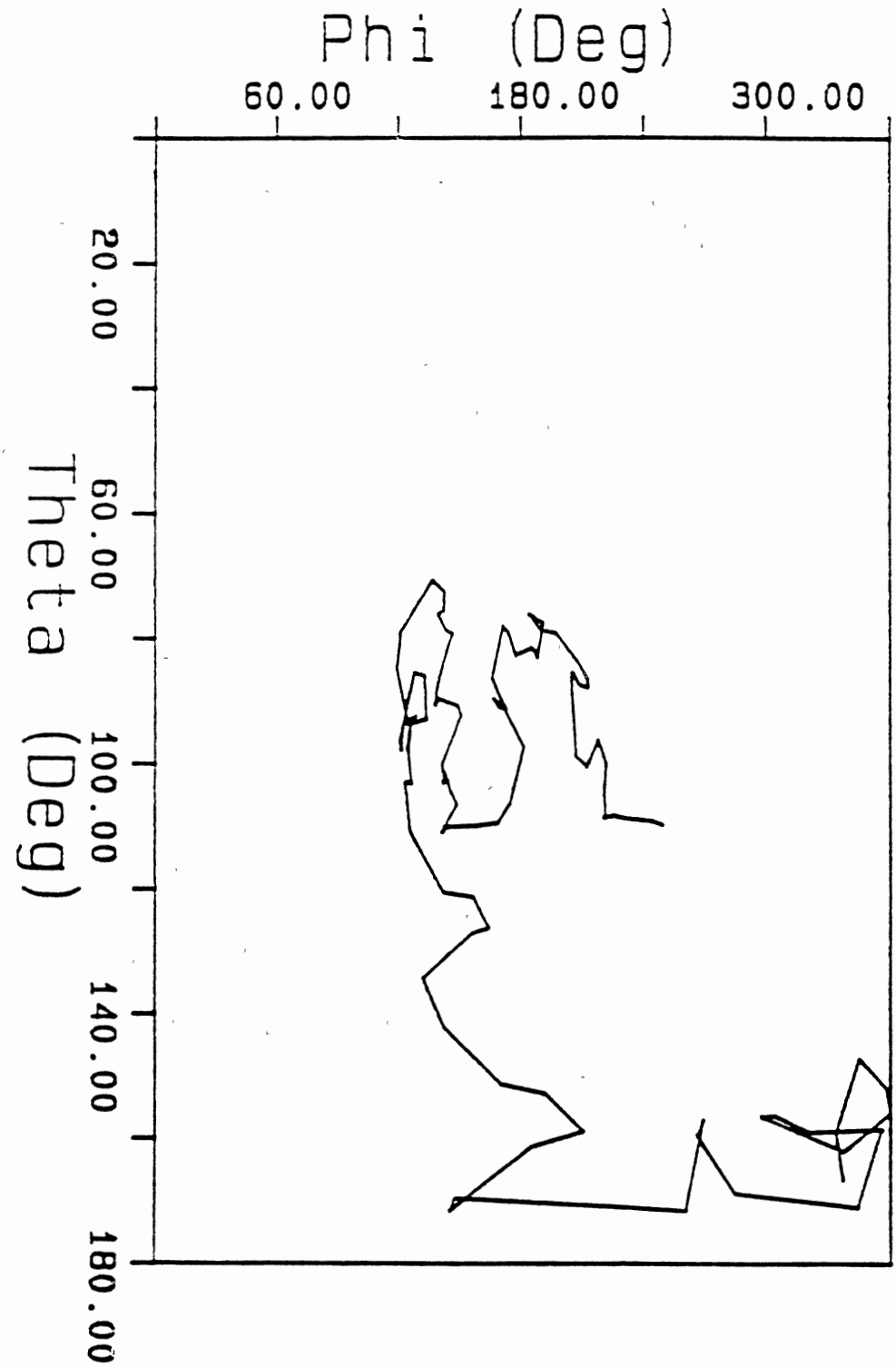
Phi (Deg)
60.00
180.00
300.00
Theta (Deg)
20.00
60.00
100.00
140.00
180.00

Figure 14. Time History Of The Cremer-Pople Coordinates For A Trajectory That Does Not Undergoes A Boat-to-Chair Ring Inversion. (a) Θ (deg) and (b) Φ (deg). The discontinuities in (b) are due to the fact that the azimuthal angle is only defined from 0° to 360°.

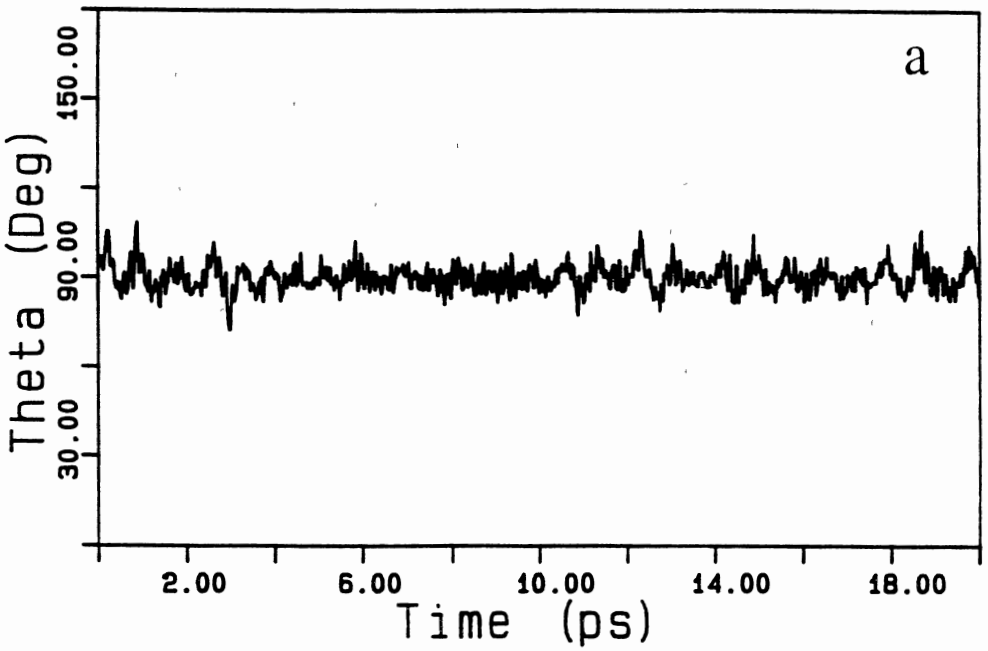
a
Theta (Deg)
150.00
90.00
30.00
2.00
6.00
10.00
14.00
18.00
Time (ps)

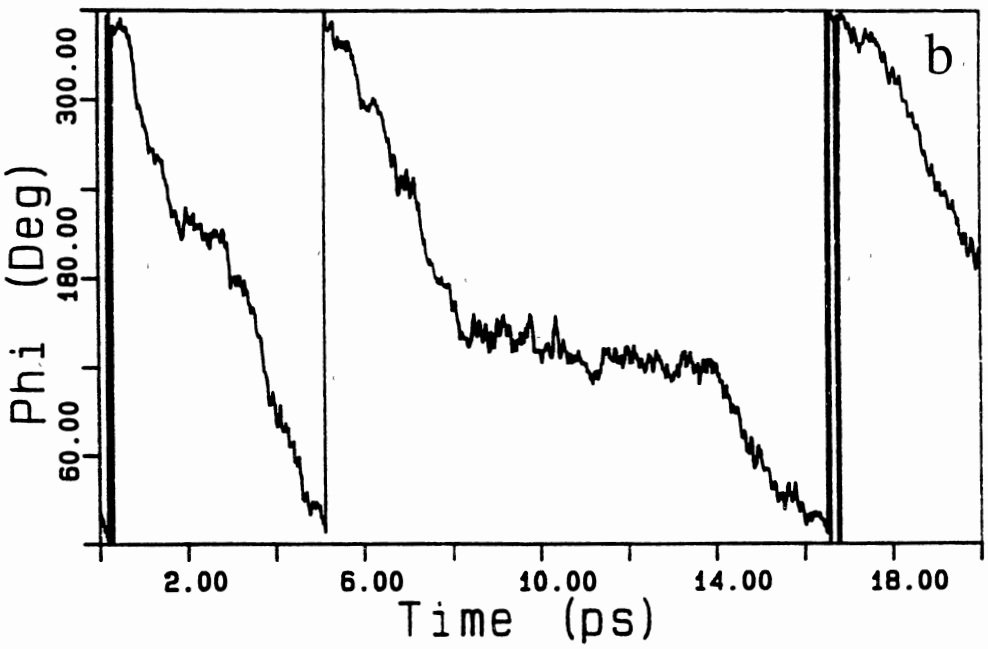
b
Phi (Deg)
300.00
180.00
60.00
2.00
6.00
10.00
14.00
18.00
Time (ps)

Rates and Activation Energies

There were 249 boat-to-twist-boat inversions observed for ensemble II. The rate constant was obtained by fitting a set of computed lifetimes to ln[N(t)/N(0)] =-kt, where N(t) is the number of lifetimes at time t, N(0) is the total number of lifetimes, and k is the pseudorotation rate constant. The rate constant was calculated to be 1.3 ps^{-1}. The transition-state theory for isomerizations yields a rate constant equation[179],

$$k_{TST} = N_{ST}\left[\frac{\kappa T}{h}\right]\exp\left\{\frac{-E_a}{\kappa T}\right\}, \qquad \text{(VI.11)}$$

where N_{ST} is a statistical factory equal to two since the potential is periodic and the molecule can pseudorotate in both directions and h is Planck's constant. Using the rate constant of 1.3 ps^{-1} for the boat-to-twist pseudorotation, the calculated activation energy is 0.8 kcal mol^{-1}.

Thermodynamic Properties

The entropy difference, ΔS, for the chair and boat configurations was estimated by using the method derived by Karplus and Kushick[180]. This method requires the use of a set of coordinates **q** to construct a harmonic potential-energy function. The coordinates are divided into a set of "important" ($\mathbf{q}'$) and "unimportant" ($\mathbf{q}''$) coordinates, where the important coordinates contribute a significant fraction of the total configurational entropy and the unimportant coordinates contribute only a small fraction. A multivariant Gaussian distribution is used to model the joint probability function. The configurational entropy is calculated using:

$$\Delta S = \frac{\kappa}{2}\ln\frac{\sigma(\text{boat})}{\sigma(\text{chair})} \qquad \text{(VI.12)}$$

where σ(boat) and σ(chair) are the determinants of the variance and covariance matrices of the important coordinates given by

$$\sigma_{ij} = < (q'_i - <q'_i>) (q'_j - <q'_j>) >. \qquad \text{(VI.13)}$$

This method is particularly useful for molecular dynamic simulations since the set of coordinates $\mathbf{q}'$ are readily available. In this calculation, there are 57 internal degrees of freedom needed to completely specify the molecule. As was shown previously (Table V), the C-N-C-N ring dihedral angle fluctuations in the boat configuration have large deviations from their respective equilibrium values due to multiple transitions between the boat and twist-boat structures. Therefore, these coordinates were disregarded in the entropy calculation since they violate the harmonic approximation which is a fundamental postulate of the entropy derivation. The set of important coordinates used in the calculation are comprised of 20 bonds, 19 bond angles, and 15 dihedral angles (the 3 ring dihedral angles were disregarded). The internal coordinates used are not unique.

The entropy difference for the chair-to-boat inversion is 6 ± 3 cal mol^{-1} K^{-1}. This gives $T\Delta S = 2 \pm 1$ kcal mol^{-1} at 300 K. The enthalpy for the chair-to-boat inversion, obtained by calculating the difference of the time-averaged potential energy for the chair and boat ensembles, is 1.5 ± 0.4 kcal mol^{-1}. Combining these results, the free energy change for the chair-to-boat inversion is 0 ± 1 kcal mol^{-1}. This value is an upper limit since the configurational entropy due to the C-N-C-N ring dihedral angles is neglected. The relatively unhindered pseudorotation between the different boat and twist-boat conformers will increase the total entropy of the boat conformer thereby decreasing the free energy change. This result suggests that the boat configuration should be favored in the gas phase equilibrium composition, but due to the large uncertainty in the entropy calculation, definite conclusions are unwarranted. There are no experimental values with which to compare these results.

Conclusions

We have performed a dynamics simulation for isolated RDX molecules using a model potential energy surface constructed from spectroscopic and theoretical data. Two ensembles of 10 trajectories were calculated, one in which the initial configuration of the molecule is the chair (I) and the other for the boat structure(II). The initial momenta were selected from a Boltzmann distribution at 300 K. The molecule was equilibrated for 20 ps by scaling the momenta to this temperature. The trajectories were then followed for an additional 20 ps with no further scaling.

The rms deviations of the internal coordinates were calculated for each of the two ensembles. The deviations in the bonds and angles are similar for the two configurations. The main difference between the two dynamically averaged structures is in the C-N-C-N ring dihedral angles, with ensemble II exhibiting the largest fluctuations. These large fluctuations are due to the frequent pseudorotations between the boat and twist structures. The calculated activation barrier is 0.8 kcal mol^{-1}.

The energy for the half-boat (C_S) and half-chair (C_1) structures were calculated by following trajectories that had undergone ring inversions and minimizing the norm of the gradient at points along the trajectories. The energies calculated for these two structures are about 4.7 kcal mol^{-1}.

The configurational entropy change for the chair-to-boat inversion is calculated to be 6 ± 3 cal mol^{-1} K^{-1}. The difference in the time-averaged potential energy for the two ensembles is 1.5 ± 0.4 kcal mol^{-1}. This gives a free energy change of 0 ± 1 kcal mol^{-1} at 300 K. This suggests that the boat conformation should be favored in the equilibrium composition of gas-phase RDX, but due to the uncertainty in the calculations definitive conclusions should not be made. It should be noted that the energetics are determined by the choice of the potential parameters, and thus the values of the thermodynamic quantities are reflections of our choices.

There is very little experimental data with which to compare our results, but experiments have shown that large fluctuations are observed in RDX in both the solution and gas phase[65,80].

CHAPTER VII

THEORETICAL STUDIES OF CONFORMATIONAL FLEXIBILITY AND RING INVERSION IN GAS-PHASE RDX

Introduction

In this chapter, a more realistic potential-energy surface is constructed for gas-phase RDX. In the studies discussed in the previous chapter, we used molecular dynamics simulations to study the conformational flexibility in isolated RDX molecules at 300 K. In that study, a harmonic potential-energy function (PES I) was employed and non-bonded interactions, i.e., interactions between atoms not bonded to one another or to a common atom were neglected. The energy difference between the chair and boat conformations was ca. 1 kcal mol^{-1}. Recent studies[82] on the structures and energetics of piperazine and its N, N-dinitro derivatives have shown that the energy difference between the chair and boat structures for these compounds is ca. 6-12 kcal mol^{-1}. Thus, an energy difference of 1 kcal mol^{-1} between the chair and boat conformations of RDX is suspect.

The effects of anharmonicity have been shown to play an important role in the x-ray refinement of proteins in vacuum, solution, and crystal environments[13-16]. Also, anharmonicity has been shown to play a large role in the dynamic disorder of polymer crystals[27-29], i.e., conformational disorder brought about by the dynamical nature of the system as opposed to the static energetics. This is disorder due to the kinetic portion of the Hamiltonian. Since dynamic disorder implies large amplitude motion, that is, rotation between different minima, anharmonic effects could play an important role by inducing

non-linear resonances, that is, Fermi resonances as well as other low order resonances[181-195].

In the work presented here, we have constructed a model potential-energy surface for isolated RDX molecules (PES II) which incorporates anharmonicity in the bond stretching terms and non-bonded interactions. We have performed Monte Carlo[1-2,157] and molecular dynamics simulations[1-5] to study the conformational flexibility and calculate the free-energy barrier for ring inversion.

Potential-Energy Surface

The equilibrium coordinates are the same as those used in PES I. For that potential-energy surface, the equilibrium coordinates were taken as averaged values of the corresponding coordinates in the crystal structure[59]. The equilibrium internal coordinates are given in Table VI. Since the start of this work, Shishkov *et al.*[60] used electron diffraction to obtain the gas-phase structure of RDX. Their results show that the gas-phase structure is close to the crystal structure except that the three nitro groups are in axial positions, whereas in the crystal structure, two of the nitro groups are axial and the third nitro group is equatorial (see Fig. 2). The differences between the experimental gas-phase structure[60] and our theoretical structure will be discussed later in this chapter.

The potential-energy surface is given by

$$V_{intra} = V_{Morse} + V_{bend} + V_{wag} + V_{torsion} + V_{L\text{-}J}, \qquad \text{(VII.1)}$$

where V_{Morse}, V_{bend}, V_{wag}, $V_{torsion}$, and $V_{L\text{-}J}$ are given by Eq.(V.10), Eq.(V.12), Eq.(V.13), Eq.(V.14), and Eq.(V.15), respectively. The harmonic force constants are taken from the potential-energy function in chapter VI (see Table I). The dissociation energy, D_e, for the Morse potential where taken from the work by Sewell and Thompson[78]. The curvature parameter, α, for the Morse potential were calculated using

Eq.V.11. The non-bonded interaction parameters, σ_{ij} and ε_{ij}, were calculated using the Lorentz-Berthelot combining rules (Eq. V.16 and V.17) where σ_i and ε_i were taken from the MM2 work by Allinger and co-workers[175,196-197]. The equilibrium values of all the internal coordinates and potential parameters are given in Table VI.

The ring inversion process can be monitored by employing the set of coordinates derived by Cremer and Pople[176-177] (for a complete derivation, see Appendix B). For a six-membered ring, the inversion of the triazine ring can be described by the coordinate Θ given by

$$\cos \Theta = \frac{\frac{1}{\sqrt{6}} \sum_{i=1}^{6} z_i \cos[\pi(i-1)]}{Q}, \qquad \text{(VII.2)}$$

where

$$Q^2 = \sum_{i=1}^{6} z_i^2; \qquad \text{(VII.3)}$$

the sums are over the six atoms of the ring and the z_i's are their atomic displacements from a plane that passes through the geometrical center of the triazine ring. Using Eqs. VII.2 and VII.3, the chair and inverted chair conformations, which are chemically equivalent structures, are located at $\Theta = 0°$ and 180°, respectively, and the boat and twist conformations are at $\Theta = 90°$.

Minimum-Energy Conformations

The different minimum-energy structures and corresponding energies have been obtained by minimizing the potential-energy function using the variable metric method discussed in chapter V. The chair conformation ($\Theta = 0°$) is the lowest energy

TABLE VI

EQUILIBRIUM VALUES OF INTERNAL COORDINATES AND POTENTIAL PARAMETERS FOR THE INTRAMOLECULAR POTENTIAL-ENERGY SURFACE OF RDX

bond	r^o [a]	D_e [b]	α [c]
C-N	1.454	3.69	1.06
N-N	1.380	2.07	1.62
N-O	1.210	4.25	1.24
C-H	1.081	4.12	1.03
bending angle	Θ^o [d]	K_Θ [e]	
C-N-C	109.500	0.4898	
N-C-N	109.500	0.4030	
C-N-N	125.250	0.5713	
N-N-O	117.202	0.7008	
O-N-O	125.596	0.4003	
N-C-H	109.500	0.4570	
H-C-H	109.327	0.3874	
wag angle	γ^o [d]	k_γ [e]	
C-N-C--NO_2	0.00	0.66	
dihedral angle	τ^o [d]	a_o [b]	a_1 a_2
C-N-C-N	60.00	0.09	-0.12 0.06
C-N-N-O	0.00	0.22	0.00 -0.22
non-bonded interactions		ε [f]	σ [a]
H		0.022	2.89
C		0.030	3.64
N		0.062	3.24
O		0.002	2.94

a) units are Å.

b) units are eV.

c) distance units are a_o^{-1}

d) angle units are degrees.

e) angle force constants in mdyn Å rad^{-2}.

f) units are kcal mol^{-1}.

conformation (Fig. 15). The internal coordinates for the minimized chair structure are compared with the equilibrium structure in Table VII.

The value of the internal coordinates for the minimum-energy structure are similar to the corresponding values of the equilibrium structure but some deviations are observed. The C-N-C bending angles decrease by ca. 3° and the C-N-C-N ring dihedral angles increase by ca. 3° for the minimum-energy structure as compared to the equilibrium structure. Thus the RDX ring is slightly more puckered in the minimum-energy structure (Q=0.64 Å) than the equilibrium structure (Q=0.59 Å). This is due mainly to the interactions between the C and N atoms of the ring.

The N-C-H_{eq} (H_{eq} = equatorial hydrogen) bending angle increases by ca. 3° while the N-C-H_{ax} (H_{ax} = axial hydrogen) bending angle decreased by ca. 2°. Also, the value of the wag angles increases slightly. The shifts in the values of the N-C-H bending angles and the C_2N—NO_2 wag angles for the minimum energy structure is due to the O-H interactions. The effect of the O-H interaction is also observed in the C-N-N-O dihedral angles which increase by 2° as compared to the equilibrium structure. These shifts reduce the O-H interaction between the H_{eq} and the neighboring oxygen atom of the NO_2 group by increasing the distance between them.

Although we have not considered the experimental gas-phase structure of RDX in constructing PES II, we can compare the experimental structure and the minimum-energy structure and observe any differences that might be present. In the electron diffraction analysis by Shishkov *et al.*[60], some assumptions concerning the geometry were made: the methylene (CH_2) moieties have local C_{2v} symmetry; the C-N-N angles are equivalent; the NO_2 geometry is planar. The bond lengths for our minimum-energy structure and the gas-phase experimental structure are similar with the largest deviation being 0.025Å in the N-N bonds. One of the largest deviations is in the C-N-C ring bending angles in which the minimum-energy structure is ca. 17° smaller than the experimental structure. This large deviation in the C-N-C bending angles causes our structure to be more puckered than the

Figure 15. Minimum Chair Structure of RDX. Atoms C(1), C(3), N(4), N(6) lie in a plane with the three nitro groups slightly out of the C-N-C plane. The triazine ring atoms adopt the chair configuration. Atom types are represented as follows: circles with lines represent carbon atoms; circles with small dots represent nitrogen atoms; circles with large dots represent oxygen atoms; open circles represent hydrogen atoms.

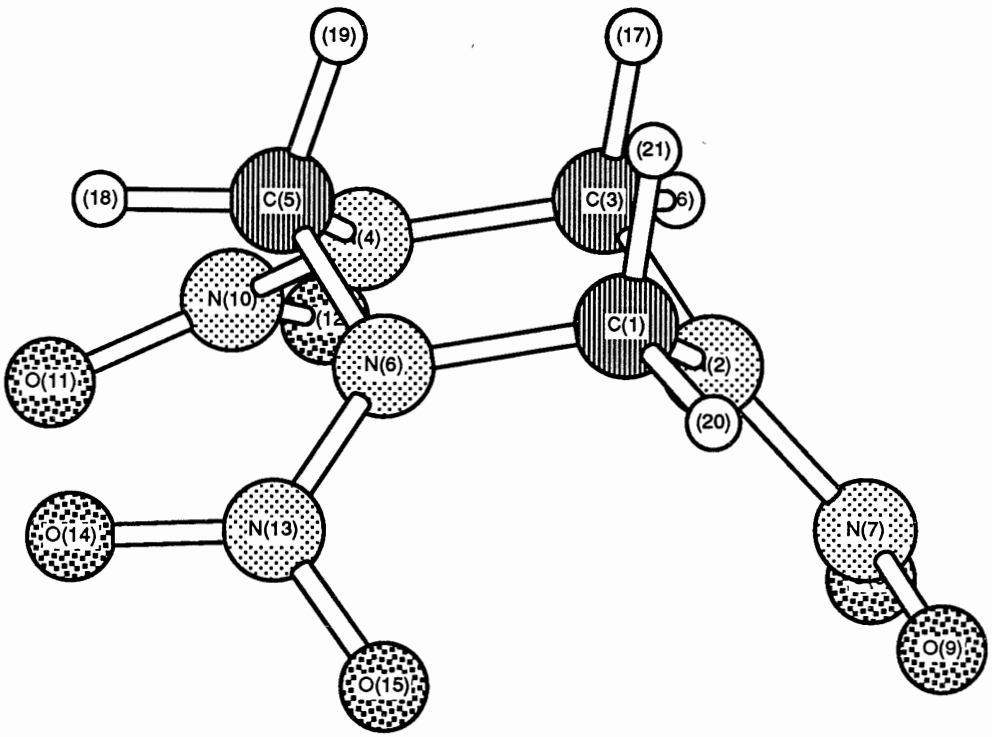

Chair structure

TABLE VII

EQUILIBRIUM AND MINIMUM-ENERGY STRUCTURES FOR RDX[a]

Coordinate	Equilibrium	Chair	Boat	Twist
Bond:[b]				
C(1)-N(2)	1.454	1.471	1.477	1.472
N(2)-C(3)	1.454	1.471	1.475	1.476
C(3)-N(4)	1.454	1.471	1.478	1.476
N(4)-C(5)	1.454	1.471	1.472	1.472
C(5)-N(6)	1.454	1.471	1.471	1.477
N(6)-C(1)	1.454	1.471	1.477	1.477
N(2)-N(7)	1.380	1.388	1.390	1.389
N(4)-N(10)	1.380	1.388	1.390	1.389
N(6)-N(13)	1.380	1.388	1.390	1.389
N(7)-O(8)	1.210	1.210	1.210	1.210
N(7)-O(9)	1.210	1.210	1.210	1.210
N(10)-O(11)	1.210	1.210	1.210	1.210
N(10)-O(12)	1.210	1.210	1.210	1.210
N(13)-O(14)	1.210	1.210	1.210	1.210
N(13)-O(14)	1.210	1.210	1.210	1.210
C(1)-H(20)	1.080	1.082	1.082	1.081
C(1)-H(21)	1.080	1.081	1.082	1.082
C(3)-H(16)	1.080	1.082	1.082	1.082
C(3)-H(17)	1.080	1.081	1.082	1.082
C(5)-H(18)	1.080	1.082	1.082	1.082
C(5)-H(19)	1.080	1.081	1.082	1.081
Bond angle:[c]				
C(1)-N(2)-C(3)	109.5	106.9	108.8	109.0
N(2)-C(3)-N(4)	109.5	109.6	115.5	115.8
C(3)-N(4)-C(5)	109.5	106.9	111.3	109.5
N(4)-C(5)-N(6)	109.5	109.6	109.6	112.8
C(5)-N(6)-C(1)	109.5	106.9	110.3	111.9
N(6)-C(1)-N(2)	109.5	109.6	115.9	112.5
C(1)-N(2)-N(7)	125.3	126.8	125.7	126.4
C(3)-N(2)-N(7)	125.3	126.2	125.5	124.6
N(2)-N(7)-O(8)	117.2	117.1	117.2	116.8
N(2)-N(7)-O(9)	117.2	117.5	117.5	117.9
O(8)-N(7)-O(9)	125.6	122.7	122.2	122.9
C(3)-N(4)-N(10)	125.3	126.8	123.6	125.0
C(5)-N(4)-N(10)	125.3	126.2	125.1	125.5
N(4)-N(10)-O(11)	117.2	117.1	117.5	117.0
N(4)-N(10)-O(12)	117.2	117.6	116.9	117.0
O(11)-N(10)-O(12)	125.6	122.8	122.7	122.4
C(5)-N(6)-N(13)	125.3	126.8	125.8	124.5
C(1)-N(6)-N(13)	125.3	126.2	123.8	123.6
N(6)-N(13)-O(14)	117.2	117.1	118.2	117.5
N(6)-N(13)-O(15)	117.2	117.1	117.2	116.8
O(14)-N(13)-O(15)	125.6	122.8	123.8	122.6

TABLE VII (Continued)

Coordinate	Equilibrium	Chair	Boat	Twist
Bond angles (cont.)				
N(2)-C(3)-H(16)	109.5	112.3	106.5	106.3
N(2)-C(3)-H(17)	109.5	107.5	110.7	110.1
N(4)-C(3)-H(16)	109.5	112.8	107.9	110.1
N(4)-C(3)-H(17)	109.5	107.5	108.8	106.6
H(16)-C(3)-H(17)	109.3	106.9	107.0	107.7
N(4)-C(5)-H(18)	109.5	112.3	112.8	110.7
N(4)-C(5)-H(19)	109.5	107.5	107.4	107.2
N(6)-C(5)-H(18)	109.5	112.8	112.7	111.4
N(6)-C(5)-H(19)	109.5	107.5	107.4	107.5
H(18)-C(5)-H(19)	109.3	106.9	106.7	106.9
N(6)-C(1)-H(20)	109.5	112.3	109.0	107.6
N(6)-C(1)-H(21)	109.5	107.5	106.8	111.0
N(2)-C(1)-H(20)	109.5	112.8	106.5	107.2
N(2)-C(1)-H(21)	109.5	107.5	110.8	111.2
H(20)-C(1)-H(21)	109.3	106.9	107.5	106.9
Wag angle[c]:				
C(1)-N(2)-C(3)--N(7)	19.1	0.3	1.4	-0.4
C(3)-N(4)-C(5)--N(10)	19.1	0.3	0.1	-1.1
C(5)-N(6)-C(1)--N(13)	19.1	0.3	0.4	-0.8
Dihedral angle[c]:				
C(1)-N(2)-C(3)-N(4)	60.0	-62.9	52.2	30.5
N(2)-C(3)-N(4)-C(5)	60.0	62.9	-5.5	28.1
C(3)-N(4)-C(5)-N(6)	60.0	-62.9	-52.0	-60.9
N(4)-C(5)-N(6)-C(1)	60.0	62.8	61.5	30.5
C(5)-N(6)-C(1)-N(2)	60.0	-62.8	-12.5	31.0
N(6)-C(1)-N(2)-C(3)	60.0	62.8	-42.3	-62.4
C(1)-N(2)-N(7)-O(9)	0.0	-2.0	4.8	-3.2
C(3)-N(4)-N(10)-O(12)	0.0	-2.0	-1.8	-4.8
C(5)-N(6)-N(13)-O(14)	0.0	-2.0	1.6	-4.6

a) Atom numbers are defined in Fig. 15.
b) Bond length units are Å.
c) Angle units are deg.

experimental structure. The C-N-N bending angles are ca. 10° larger in the minimum-energy structure as compared to the corresponding value in the experimental structure. The largest deviation between our minimum-energy structure and the experimental gas-phase structure is the wag angles. The wag angle, defined as the angle between the plane made by the C-N-C atoms of the ring and the N-N bond, is 0.3° (planar) for all three nitro groups in the minimum-energy structure while the experimental structure shows all three wag angles to be 19° (axial). In our structure, the potential function for the wag angle is harmonic. Therefore, the possibility of axial-equatorial inversion is neglected.

The calculated normal-mode frequencies for the theoretical chair configuration are compared with the experimental frequencies of RDX in the solution phase[66] and are presented in Table VIII. Unfortunately, there is no complete gas-phase spectrum, but the solution-phase and gas-phase frequencies were shown to be similar[65]. The average root mean square deviation (<rms>) between the experimental and calculated frequencies is 33 cm^{-1}.

The boat and twist minimum energy structures ($\Theta = 90°$) were obtained using the variable metric method and the internal coordinates are given in Table VII. The boat structure (Fig. 16a) is 4.5 kcal mol^{-1} higher in energy than the chair structure while the twist structure (Fig. 16b) is 4.0 kcal mol^{-1} higher in energy than the chair structure. There are no experimental data with which to compare either the minimized structures or corresponding energies of these two conformations. The calculated normal mode frequencies for the boat and twist structures are given in Table VIII.

Monte Carlo Procedures

Monte Carlo[89-91] techniques have been employed to calculate the average potential-energy and free energy surfaces for the chair→boat/twist ring inversion at 300 K. The MC method was described in chapter V. The convergence of a standard Monte Carlo method is poor when dealing with activated events since the Metropolis[158] method

TABLE VIII

EXPERIMENTAL AND CALCULATED FREQUENCIES FOR RDX[a]

Solution phase[b]	Calculated[c]		
	Chair	Boat	Twist
——	38 (2)	12	12
——	——	29	33
——	41	40	49
——	52 (2)	45	53
——	——	55	64
——	57	75	80
——	178 (2)	163	166
——	——	172	182
——	249	190	211
——	257	233	221
——	261 (2)	244	245
——	——	258	262
——	316 (2)	274	269
——	——	290	302
——	343	342	312
——	424 (2)	404	406
——	——	417	420
410	438 (2)	434	428
470	——	468	467
490	441	478	472
595	495	518	513
610	582	562	572
——	648 (2)	588	585
——	——	603	624
740	741 (2)	732	733
750	——	741	749
794	776 (2)	783 (2)	762
855	——	——	794
——	807	813	811
910	877	885	885
935	956	1007	1009
——	1027 (2)	1011 (2)	1020
1015	——	——	1032
1045	1038 (2)	1034	1040 (2)

TABLE VIII (Continued)

Solution phase[b]	Calculated[c]		
	Chair	Boat	Twist
1230	——	1064	——
——	1052	1128	1130
1270	1165 (2)	1167	1164
1320	——	1179	1193
1392	1185	1211	1207
——	1285	1256	1259
1435	1290 (2)	1264	1262
1460	——	1297	1290
——	1335 (2)	1333 (2)	1330 (2)
——	1382	1399	1401
——	1466	1453	1452
1550	1519 (2)	1522 (2)	1523 (2)
1585	1554 (3)	1555 (3)	1553 (3)
2980	2982 (3)	2980 (3)	2980 (3)
3080	3051 (3)	3045 (3)	3049 (3)

a) Units are cm^{-1}
b) Iqbal *et al.*, Ref. 66
c) This work.

Figure 16. Boat and Twist Minimum Structures of RDX. (a) The boat structure is 4.5 kcal mol^{-1} higher in energy than the chair structure. Atoms C(1), C(3), N(4), and N(6) lie in a plane. (b) The twist structure is 4.0 kcal mol^{-1} higher in energy than the chair structure. Atoms C(1), C(3), C(5), and N(6) lie in a plane. The atom types are the same as in Figure 15, but the molecules have been rotated for clarity.

A

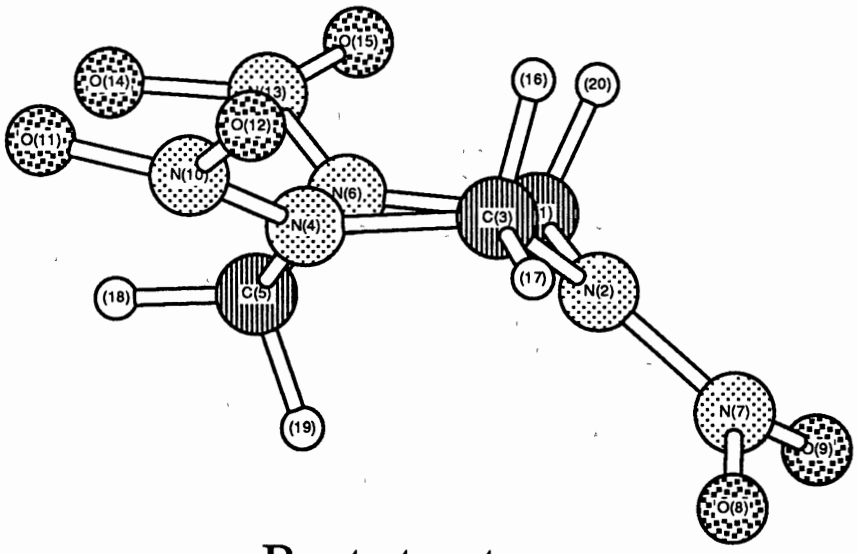

Boat structure

B

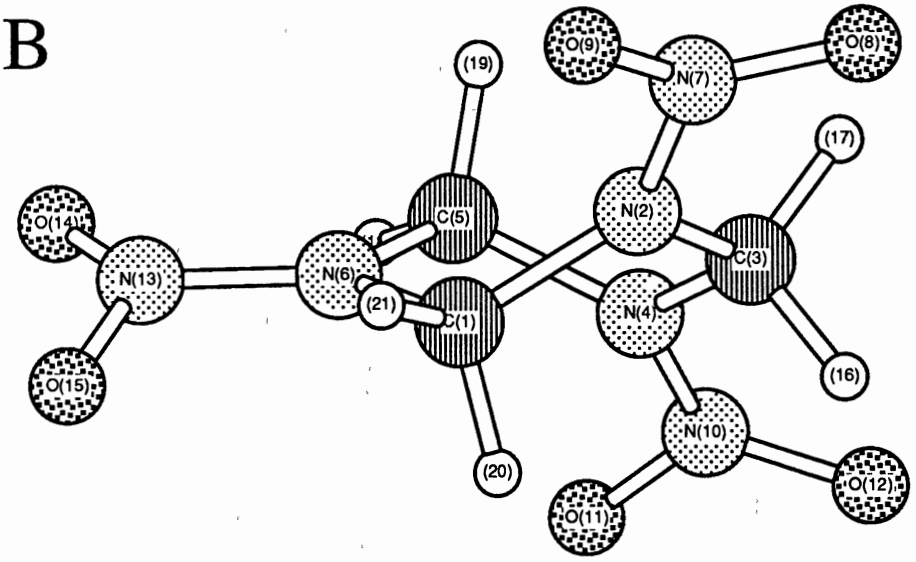

Twist-boat structure

generates Markov chains that are weighted to favor low energy configurations, that is, near the minimum of the potential-energy surface. Excursions to the barrier region are infrequent. One method uses to overcome this problem is non-Boltzmann sampling[1-2,198-200].

The free energy, $A(\Theta)$, is obtained by integrating[119]

$$\exp[-\beta A(\Theta)] = \int \delta[\Theta^* - \Theta(\mathbf{q})] \exp[-\beta V(\mathbf{q})]\, d\mathbf{q} \qquad \text{(VII.4)}$$

where $\beta = (\kappa T)^{-1}$ with κ and T being the Boltzmann constant and temperature respectively, $V(\mathbf{q})$ is the potential energy of configuration $\mathbf{q}$, and $\delta[\Theta^* - \Theta(\mathbf{q})]$ is the Dirac delta function that is equal to unity for $\Theta(\mathbf{q})=\Theta^*$ and zero otherwise. In the Monte Carlo solution to Eq. VII.4, the integral can be expressed as

$$\exp[-\beta A(\Theta)] = \lim_{N\to\infty} N^{-1} \sum_{i=1}^{N} \delta[\Theta^* - \Theta(\mathbf{q})] \exp[-\beta V(\mathbf{q})]. \qquad \text{(VII.5)}$$

The sum is evaluated using Metropolis sampling[158] which employs a Markov chain (see chapter V.)

Umbrella sampling[198-200] was employed to overcome the large barrier between the chair and boat/twist conformation. In this method, configuration space is sampled according to

$$\rho_W = \frac{W(\Theta) \exp[-\beta V(\mathbf{q})]\, d\mathbf{q}}{\int W(\Theta) \exp[-\beta V(\mathbf{q})]\, d\mathbf{q}} \qquad \text{(VII.6)}$$

where ρ_W is the weighted distribution and $W(\Theta)$ is a specified weight function which biases the system to a specific region of configuration space. The weight function must be introduced such that it can subsequently be removed. In this work, the weight function is given by

$$W(\Theta) = \exp[-\beta V_{bias}(\Theta)]. \qquad \text{(VII.7)}$$

with $V(\Theta)$ being a biasing potential,

$$V_{bias}(\Theta) = \frac{1}{2} k_{bias}(\Theta - \Theta^{o})^{2}, \qquad \text{(VII.8)}$$

(where Θ represents the reaction coordinate and k_{bias} is the harmonic force constant) used to bias the distribution of the RDX molecule about Θ^{o}. The free-energy surface in the unbiased system is given by

$$\exp[-\beta A(\Theta)] = \frac{N^{-1} \sum_{i=1}^{N} \delta[\Theta-\Theta(\mathbf{q})] \exp[-\beta V(\mathbf{q})] W(\Theta)^{-1}}{N^{-1} \sum_{i=1}^{N} W(\Theta)^{-1}}. \qquad \text{(VII.9)}$$

For each biasing potential or window, i.e., each different Θ^{o}, the free energy surface is calculated. Since the full free-energy surface is continuous, it can be constructed piece-wise from each individual window provided there is good overlap between adjacent windows.

For this calculation, Θ° ranged from 0° to 90° in increments of 30°. The bias force constant, k_{bias}, was taken as 0.01 kcal mol^{-1} deg^{-2}. The initial configuration of the "ith" window was taken as the final configuration of the "(i -1)th" window. Each Markov chain was generated using the prescription described in chapter V. A new configuration is generated by randomly moving an atom of the RDX molecule. If the move lowers the potential-energy of the molecule, the move is accepted, otherwise, the new move is accepted with a probability of $\exp[-\beta\Delta V']$, where $\Delta V' = V'_{trial} - V'_{old}$, $V' = V_{intra} + V_{bias}$, and V_{intra} is given by Eq. VIII.1. The Markov chain was initialized for 1000 steps after

which, $5x10^6$ steps were generated and the free-energy surface in each window was calculated. The step size of the chain is δq=0.1 Å which results in about a 0.50 acceptance ratio. This ratio was maintained throughout the calculation.

Molecular Dynamics

Molecular dynamics methods were used to compute the mean dynamical structure for gas-phase RDX at 300 K. The molecular dynamics methods described in the chapter V were employed. The RDX molecule was initiated in the chair configuration and the atomic momenta were sampled from a thermal distribution (Eq. V.21) at 300 K. One warm up trajectory was run for 20 ps during which the atomic momenta were scaled to the desired ensemble temperature. Periodically, during the warm up trajectory, configurations of the RDX molecule were saved as initial configurations for subsequent trajectories in the ensemble. Using one of the saved configurations, the atomic momenta were selected from a thermal distribution and the molecule was equilibrated for 20 ps by periodically scaling the momenta. The trajectory was continued without further scaling for 20 ps and the phase-space coordinates were saved every 10 fs for subsequent analysis. An Adams[201] numerical integration method was employed with an error tolerance of $1x10^{-6}$ which gave energy conservation of $1x10^{-4}$ percent error. An ensemble of 10 trajectories was computed.

Due to the small number of atoms in RDX and the exchange between kinetic and potential energy, a small deviation in the temperature for each trajectory was accepted. If a trajectory deviated by more than 10 K from the desired ensemble temperature, it was discarded and a new trajectory was initiated.

Results and Discussion

Dynamical Structure

The dynamically averaged chair structure was computed using molecular dynamics methods. An ensemble of 10 trajectories for 20 ps each was calculated which gave 200 ps of dynamics. The ensemble temperature was 306±5 K. The mean structure was obtained by calculating the time averaged structure for the 200 ps of dynamics. Table IX compares the dynamical structure with the minimum-energy structure for the chair conformation. As is shown in Table IX, the bond stretches and angle bending coordinates are very close to the corresponding values of the minimum-energy structure. There is a slight deviation between the dynamically averaged C-N-C-N ring dihedral angles and those for the minimum-energy structure. The pucker coordinates for the average structure are; Q=0.64±0.04 Å and $\Theta = 10\pm5°$, while the values of the pucker coordinates for the minimum energy structure are; Q=0.64 Å and $\Theta = 0.0°$. The time-averaged C-N-N-O dihedral angle shows the largest deviation for all of the coordinates as compared to the minimum-energy structure. The mean value is ca. 0° while the value for the C-N-N-O dihedral angle in the minimum structure is ca. -2°. The cause of this deviation will be discussed later in this section.

The RDX molecule stayed in the chair conformation for the entire 200 ps of dynamics, that is, no chair→boat/twist ring inversions were observed at 300 K.

The time averaged structure for the boat/twist conformation ($\Theta = 90°$) could not be obtained since no trajectories initiated in the boat/twist conformation remained in that conformation for the duration of the equilibration period.

We compared PES I (see Chapter. V) and the revised potential-energy surface, PES II. Both potential-energy surfaces give time-averaged structures that are close to their corresponding minimum-energy structures. The difference in energy between the boat and

TABLE IX

MEAN STRUCTURE OF RDX IN THE CHAIR CONFORMATION AT 300 K[a]

Coordinate	Minimum-enrgy value	Mean value from dynamics	<rms> deviation
Bond:[b]			
C(1)-N(2)	1.47	1.47	0.03
N(2)-N(7)	1.39	1.39	0.03
N(7)-O(8)	1.21	1.21	0.02
C(3)-H(16)	1.08	1.08	0.03
Bond angle:[c]			
C(1)-N(2)-C(3)	106.9	106.8	3.44
N(2)-C(3)-N(4)	109.6	109.9	4.20
C(1)-N(2)-N(7)	126.8	126.7	3.42
N(2)-N(7)-O(8)	117.1	117.0	3.89
O(8)-N(7)-O(9)	122.7	121.8	4.58
N(2)-C(3)-H(16)	112.3	112.2	4.60
N(2)-C(3)-H(17)	107.5	107.3	5.20
H(16)-C(3)-H(17)	106.9	106.7	5.15
Wag angle:			
C(1)-N(2)-C(3)--N(7)	0.3	0.6	4.60
Dihedral angle:			
C(1)-N(2)-C(3)-N(4)	-62.9	-61.8	7.73
N(2)-C(3)-N(4)-C(5)	62.9	61.9	7.45
C(3)-N(4)-C(5)-N(6)	-62.9	-61.9	7.48
N(4)-C(5)-N(6)-C(1)	62.8	61.7	7.90
C(5)-N(6)-C(1)-N(2)	-62.8	-61.7	7.76
N(6)-C(1)-N(2)-C(3)	62.8	61.7	7.67
C(1)-N(2)-N(7)-O(9)	-2.0	0.1	11.15

a) Representative internal coordinates are listed (atom numbers are defined in Fig. 15).
b) Bond length units are Å.
c) Angle units are deg.

chair structure for PES I is ca. 1 kcal mol^{-1} while that for PES II is ca. 4.0 kcal mol^{-1} which is in better accord with the literature[82]. Also, the RDX molecule is more flexible using PES I as compared with PES II. This can be seen by comparing the <rms> values calculated using PES I (Table IV) and those calculated using PES II (Table IX). As can be seen, the <rms> value is consistently larger for the corresponding internal coordinates of PES I compared with PES II. One exception is in the C-N-N-O dihedral angle which has a larger fluctuation for PES II than for PES I. This large fluctuation is due to the O-H interaction which modifies the C-N-N-O torsion potential. There are two shallow minima at $\tau_{C\text{-}N\text{-}N\text{-}O} = \pm 2°$ due to the $O\text{-}H_{eq}$ interaction. At the simulation temperature (300 K) though, the energy of the $\tau_{C\text{-}N\text{-}N\text{-}O}$ is larger than the small barrier between the two minima and therefore, the O-H interaction has little effect on the dynamics but produces a slightly flatter potential near the bottom of the well which gives rise to the larger fluctuations.

Thermodynamic Parameters

The average potential-energy and free-energy surfaces are calculated at 300 K using MC methods with umbrella sampling[198-200] and are shown in Fig. 17(a-b). Due to the symmetry of the potential, the reaction coordinate was only followed from Θ=0° to Θ=90°. The solid line is the non-linear least squares fit to the calculate points. The average deviation between the non-linear least squares line and calculated points is 0.1 kcal mol^{-1} and 0.3 kcal mol^{-1} for the potential-energy and free-energy surfaces, respectively. As Fig. 17a. illustrates, the ΔH(300 K) for the chair→boat/twist inversion is ca. 4.5 kcal mol^{-1} with an activation enthalpy, $\Delta H^{\dagger}$(300 K), of ca. 4.8 kcal mol^{-1}. Figure 17b. shows the calculated free-energy surface. The free energy, ΔA(300 K), for the chair→boat/twist inversion is calculated to be ca. 4.0 kcal mol^{-1} and the activation free energy, $\Delta A^{\dagger}$(300 K), is ca. 4.7 kcal mol^{-1}. The $\Delta H^{\dagger}$ for PES I (4.7 kcal mol^{-1}), taken as the potential energy of the transition-state structure, is very close to the $\Delta H^{\dagger}$ for PES II. Thus, non-bonded

Figure 17. Potental-Energy and Free-Energy Surfaces for RDX at 300 K. (a) Average potential-energy surface. The deviation between the calculated points and the non-linear least squares fit line is 0.1 kcal mol^{-1}. (b) The free-energy surface. The deviation is 0.3 kcal mol^{-1}.

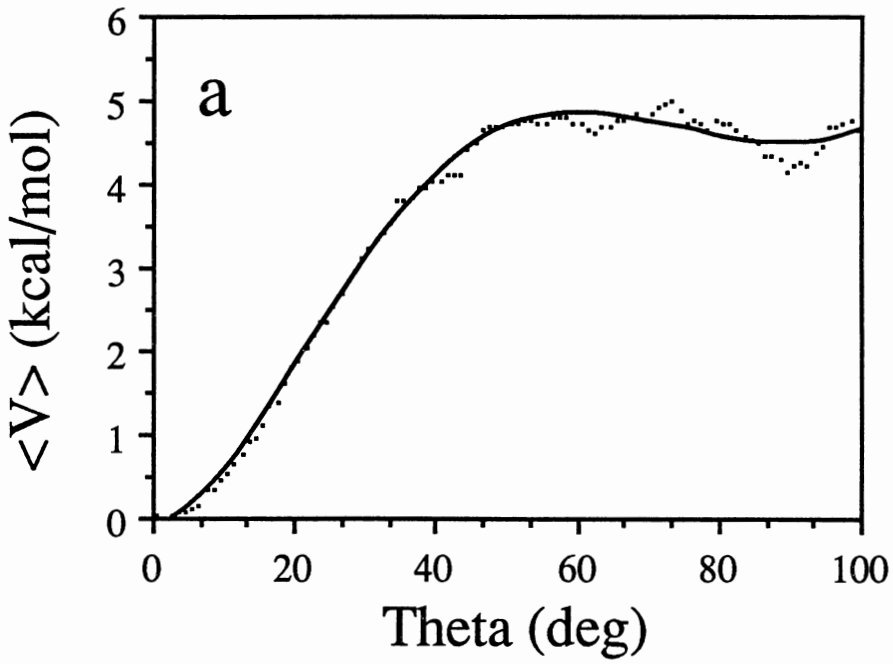
a
<V> (kcal/mol)
Theta (deg)
0
1
2
3
4
5
6
0
20
40
60
80
100

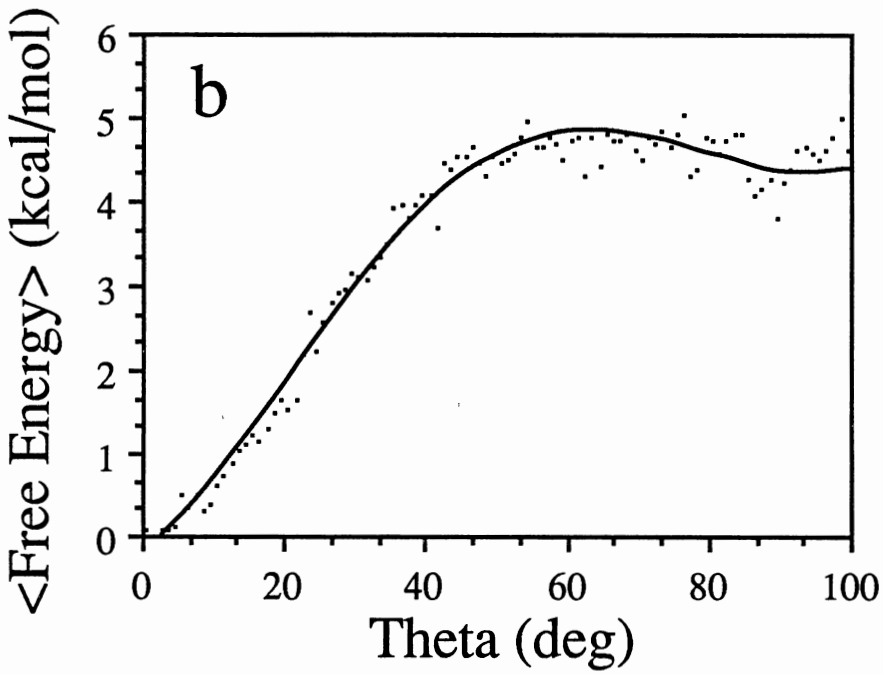
b
<Free Energy> (kcal/mol)
Theta (deg)
0
1
2
3
4
5
6
0
20
40
60
80
100

interactions substantially modify the difference in the minimum-energy structures by ca. 3.5 kcal mol^{-1} but do not strongly affect the barrier for ring inversion.

Conclusions

We have modified the potential-energy surface constructed in chapter VI to include anharmonicity in the bond stretching terms and non-bonded interactions between atoms not bonded to one another or to a common atom. The chair, boat, and twist minimum-energy structures and corresponding energies have been calculated using a variable metric technique. The chair structure was found to be the lowest energy structure with the boat and twist structures being 4.5 and 4.0 kcal mol^{-1} higher in energy than the chair conformation respectively. The chair structure compares well with the experimental gas-phase structure[60], with the largest deviation being in the C-N-C bending angle and C_2N--NO_2 wag angles. Our structure adopts a more puckered chair conformation than the experimental gas-phase structure. Also, the nitro groups adopt the axial position in the experimental structure but remain planar in our minimum-energy structure.

The dynamical structure is close to the minimum-energy structure with small deviations in the C-N-C-N and C-N-N-O dihedral angles. The C-N-C-N dihedral angles are slightly smaller in the dynamical structure as compared with the minimum-energy structure. The C-N-N-O dihedral angles deviate by ca. 2° between the time-averaged structure and the minimum-energy structure. The dihedral angles also exhibit the largest fluctuations. This is due to the O-H interaction which slightly modifies the effective C-N-N-O torsional potential. Overall, PES I exhibits more flexibility than does PES II.

The thermodynamics of PES II are: $\Delta H(300) = 4.5$ kcal mol^{-1}; $\Delta A(300) = 4.0$ kcal mol^{-1}; $\Delta H^{\dagger}(300) = 4.5$ kcal mol^{-1}; and $\Delta A^{\dagger}(300) = 4.7$ kcal mol^{-1}. In contrast to PES I, where the boat/twist conformation was favored due to the large entropy difference between the chair and boat/twist structures, the chair conformation is strongly favored on PES II by ca. 4.5 kcal mol^{-1}. This is in accord with the electron diffraction

experiments which shows that the chair configuration is favored in the gas-phase[60]. It should be pointed out that the energetics are determined by the choice of potential parameters and thus, are a reflection of our choices.

CHAPTER VIII

MOLECULAR DYNAMICS STUDY OF RING INVERSION OF RDX IN THE GAS-PHASE AND A DENSE XE FLUID AT 500 K

Introduction

In chapters VI and VII, the conformational dynamics for isolated RDX molecules were studied. Although studies of molecules in a vacuum can give valuable insight into the dynamics of these systems, vacuum studies do not correlate directly with experimental situations. In the study of isolated RDX, the energy of the molecule was a constant during each trajectory (microcanonical ensemble). In a thermal experiment, intermolecular energy transfer results in a continuous interchange of both energy and angular momenta between the solute molecule and the bath gas (canonical ensemble).

There have been many studies concerning the dynamical effects of the solvent on barrier crossing processes[33-44,108-117,132-139,156,159-164]. These studies show that the solvent can have a dramatic effect on the rate of reaction. For the prototypic atom transfer reaction, AB+C $\rightarrow$ AB + C, Hynes and co-workers[33-34] and Wilson and co-workers[35-37] have shown that the solvent can dramatically alter the reaction dynamics from those expected for the similar gas-phase process if the solvent couples strongly to the solute molecules. For a weakly coupled system, gas-phase behavior is observed, i.e., TST predicts the reaction rates fairly well. Straube *et al.*[44] and Robinson and co-workers[41-43] have shown that for a model isomerization process, a solvent environment can have a marked effect on the rate of barrier crossing due to the changing forces experienced by the solute along the reaction coordinate. When the barrier crossing takes place rapidly in

comparison with the solvent motion, local non-equilibrium effects exist[43]. Chandler and co-workers[39-40,124] have studied the solvent effects on the ring inversion of cyclohexane. They shown that quasi-periodic motion can play an important role in the dynamics of the system. Since quasi-periodic trajectories decrease the rate of ring inversion, the ability of the solvent to quench these trajectories leads to increased rates with increasing solvent density or pressure. Thus, intermolecular coupling, i.e., coupling between the solute and solvent can play a large part in reaction dynamics of condensed-phase systems.

In this chapter, we discuss the effects of a Xe solvent on the equilibrium distribution of the chair and boat/twist isomers and on the rate constant for chair→boat/twist ring inversion.

The presence of the bulky exocyclic nitro groups of RDX (see Fig. 15), which are coupled directly to the reaction coordinate, requires that a large volume must be swept out for the ring inversion process. Thus, the solvent could play a large role in determining the inversion dynamics of RDX by hindering the motion of the nitro groups. The study of hexahydro-1,3,5-trimethyl-1,3,5-triazine[147] showed that the bulky exocyclic methyl groups contribute to the slower rate of ring inversion and higher free energy of activation in the liquid phase as compared with the gas phase.

Another factor in determining the rate of ring inversion is the hydrodynamic volume, i.e., the excluded volume difference between the product and reactant conformations. The larger the hydrodynamic volume difference between product and reactant structures, the larger the entropic contribution to the rate constant for the isomerization. In the model systems studied by Statman and Robinson[41], the *cis* configuration is about two-thirds the volume of the *trans* configuration which contributes to the difference between the *cis*→*trans* and *trans*→*cis* isomerization rate constants (a factor of 4) even thought the gas-phase isomerization potential is symmetric (the *cis*→*trans* and *trans*→*cis* isomerization rate constants should be equal).

For RDX, the energy difference between the boat/twist configuration and the chair configuration (see Chapter VII), may well be compensated by changes in the hydrodynamic volume as the solvent density increases. Thus, the equilibrium constant, which for gas-phase RDX strongly favors the chair conformation, could tend toward unity.

Potential-Energy Surface

The potential-energy surface is given by,

$$V = V_{intra} + V_{inter} + V_{wall}, \tag{VIII.1}$$

where the intramolecular potential, V_{intra}, from chapter VII was employed. The intramolecular potential parameters are given in Table VI.

The intermolecular potential, V_{inter}, for the RDX-Xe and Xe-Xe interactions are described by a Lennard-Jones 6-12 interaction

$$V_{L\text{-}J} = \sum_i \sum_j 4\varepsilon_{ij} \left\{ \left(\frac{\sigma_{ij}}{r_{ij}} \right)^{12} - \left(\frac{\sigma_{ij}}{r_{ij}} \right)^{6} \right\}, \tag{VIII.2}$$

where the potential parameters, σ_{ij} and ε_{ij}, are calculated using the Lorentz-Berthelot mixing rules given by

$$\sigma_{ij} = \frac{1}{2}[\sigma_i + \sigma_j] \tag{VIII.3}$$

and

$$\varepsilon_{ij} = \sqrt{\varepsilon_i \varepsilon_i} \tag{VIII.4}$$

where σ_i and ε_i are the atomic radius and Lennard-Jones well depth for the "ith" atom. The intermolecular potential parameters are given in Table X.

The finite volume method by Murrell and co-workers[156,160-164] was employed as described in chapter V. The wall potential, V_{wall}, was modeled using a modified Born-Mayer[156] potential given by

$$V_{wall} = \sum_i \frac{A\rho_i^2}{R^2} e^{-b(R-\rho_i)}, \qquad \text{(VIII.5)}$$

where R is the radius of the sphere and ρ_i is the distance of atom i from the center of the sphere. The ρ_i^2 term in the numerator guarantee the potential and first derivative go to zero at the center of the sphere (ρ_i=0). The parameters A and b are taken as 100 kcal mol^{-1} and 9.5 Å^{-1}, respectively.

Computational Procedures

Gas-Phase MD Simulation. The MD simulation of gas-phase RDX was performed as described in chapter IV. No Xe solvent atoms were present and no boundary conditions were applied. The RDX molecule was initially in the chair conformation and the momenta were selected from a thermal distribution (Eq. V.21) at 500 K. A warm up trajectory was calculated for 10 ps during which, the momenta were scaled (Eq. V.22) to the ensemble temperature. Only one warm up trajectory was calculated. Periodically during the warm up trajectory, configurations of the RDX molecule were saved as initial configurations for subsequent trajectories. Using one of the saved configurations, a set of atomic momenta were sampled from a thermal distribution and the trajectory was equilibrated for 10 ps by periodically scaling the atomic momenta to the ensemble temperature. After the equilibration period, the trajectory was continued for 50 ps without further scaling. The phase-space coordinates were saved every 10 fs for subsequent

TABLE X

POTENTIAL PARAMETERS FOR THE INTERMOLECULAR INTERACTIONS FOR RDX AND XE

intermolecular interactions[a]	ε[b]	σ[c]
H	0.017	2.81
C	0.102	3.35
N	0.074	3.31
O	0.122	2.95
Xe	0.549	3.97

a) The values were taken from Ref. 1.
b) Units are kcal mol^{-1}.
c) Units are Å.

analysis. If a trajectory deviated by more than 10 K, it was discarded and a new trajectory was initiated. Each trajectory required 7 hours of CPU time on an Alliant FX/8 vector processor. An ensemble of 20 trajectories was calculated which gave 1000 ps of dynamics. The ensemble temperature was 499±3 K.

Condensed-Phase MD Simulation. The condensed-phase system consisted of one RDX molecule and 128 Xe solvent atoms. The initial conditions of the RDX molecule and Xe solvent were calculated as described in chapter V. The RDX molecule is placed at the center of the reaction sphere while the solvent atoms are place in an fcc lattice about the molecule. The radius of the sphere is determined from the desired solvent density. The RDX molecule was initially in the chair configuration. The atomic momenta of all the atoms were sampled from a thermal distribution (Eq. V.21) at 500 K. The system was annealed for 2.0 ps to reduce any large potential due to the starting configuration. This was achieved by zeroing the atomic momenta whenever the kinetic energy exceeded the potential energy. A warm up trajectory was calculated for 10 ps during which the atomic momenta were scaled periodically to the desired ensemble temperature (Eq. V.22). Only one warm up trajectory was performed for each ensemble. Each trajectory was calculated for 60 ps, 10 ps of equilibration and 50 ps of production. The phase-space coordinates were saved every 10 fs for subsequent analysis. Each condensed-phase trajectory required 12 hours of CPU time on an IBM3090-200s vector processor. Ensembles of 8-12 trajectories were calculated at eight different solvent concentrations. No trajectories were discarded from the condensed phase ensembles.

An Adams[201] numerical integration method was employed for both the gas-phase and condensed-phase calculations with an tolerance of $1x10^{-6}$ which gave energy conservation of $1\ x10^{-3}$ percent error, respectively.

Results and Discussion

A temperature of 500 K was used so that a fair number of events could be observed in both the gas and condensed-phases. We verified the definition of temperature, given by Eq. V.23, for both calculations. The speed (Eq. VI.10) of each atom type, C, N, O, H, and Xe, was calculated every 10 fs during a trajectory and a histogram of 15-20 equal subintervals was obtained. The distribution of speeds are compared to the Maxwell-Boltzmann distribution (Eq. VI.9) calculated at the ensemble temperature.

The distribution of speeds for gas-phase RDX are plotted in Fig. 18(a-d). The histograms for gas-phase RDX were obtained by averaging over all 20 trajectories of the gas-phase ensemble. As can be seen, the Maxwell-Boltzmann distribution represents the trajectory data very well.

The distribution of speeds for the RDX molecule and the Xe atoms at solvent densities of [Xe] = 3.1 mol dm^{-3} and [Xe] = 19.1 mol dm^{-3} are shown in Figs. 19-22. The histograms for RDX and the Xe solvent represent the distribution of speeds for a single trajectory. Thus, the agreement between the molecular dynamics simulation data and the Maxwell-Boltzmann distribution does not appear as good as for the gas phase, but as more trajectories were averaged, the agreement more become better. At both densities, the most probable speeds for the four different atom types of RDX are shifted slightly to the higher region (Figs. 19(a-d) and 21(a-d)), but the distribution exhibits the correct profile. The speed distributions for the Xe atoms at the lower (Fig. 20) and upper (Fig. 22) densities are well represented by the Maxwell-Boltzmann distribution.

The time history of the average temperature of a condensed-phase trajectory is shown in Fig. 23. As can be seen, after ca. 6 ps, the fluctuations are negligible. The temperature for this trajectory is 510 K.

Figure 18. Distribution of Speeds for Gas-Phase RDX. The Maxwell-Boltzmann distribution (solid line) is calculated at the ensemble temperature of 500 K. The atom types are as follows: (a) carbon atoms, (b) nitrogen atoms, (c) oxygen atoms, and (d) hydrogen atoms.

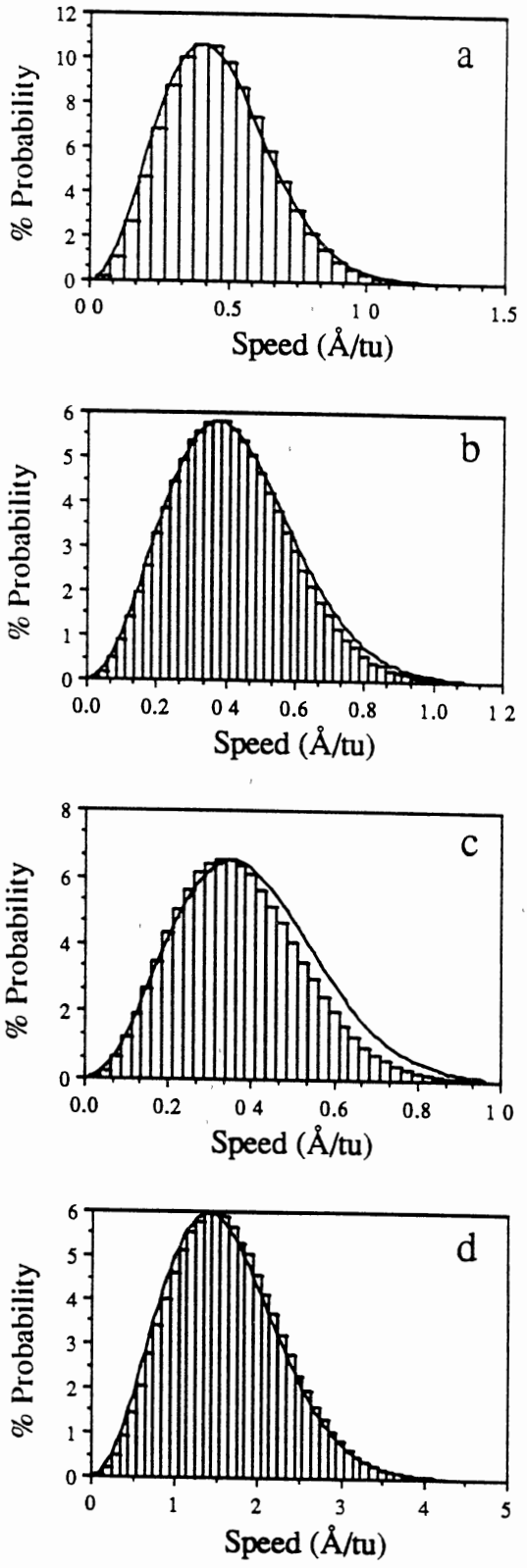
a
% Probability
Speed (Å/tu)
b
% Probability
Speed (Å/tu)
c
% Probability
Speed (Å/tu)
d
% Probability
Speed (Å/tu)

Figure 19. Distribution of Speeds for RDX at [Xe] = 3.1 mol dm^{-3}. The Maxwell-Boltzmann distribution (solid line) is calculated at 500 K. The atom types are as follows: (a) carbon atoms, (b) nitrogen atoms, (c) oxygen atoms, and (d) hydrogen atoms.

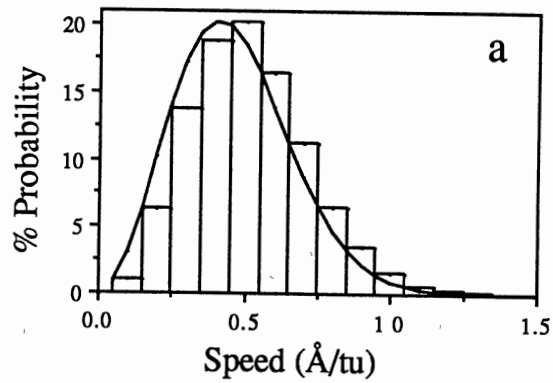
a
% Probability
20
15
10
5
0
0.0
0.5
1 0
1.5
Speed (Å/tu)

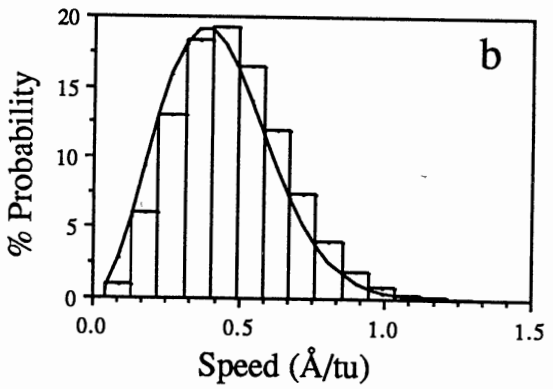
b
% Probability
20
15
10
5
0
0.0
0.5
1.0
1.5
Speed (Å/tu)

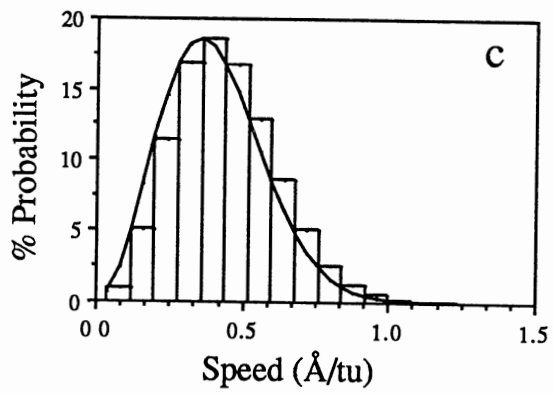
c
% Probability
20
15
10
5
0
0 0
0.5
1.0
1.5
Speed (Å/tu)

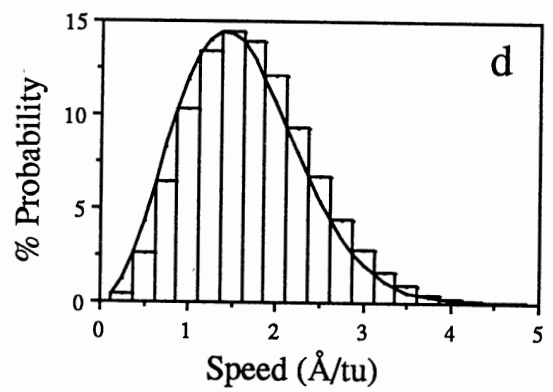
d
% Probability
15
10
5
0
0
1
2
3
4
5
Speed (Å/tu)

Figure 20. Distribution of Speeds for the Xe atoms at [Xe] = 3.1 mol dm^{-3}. The Maxwell-Boltzmann distribution (solid line) is calculated at a temperature is 500 K.

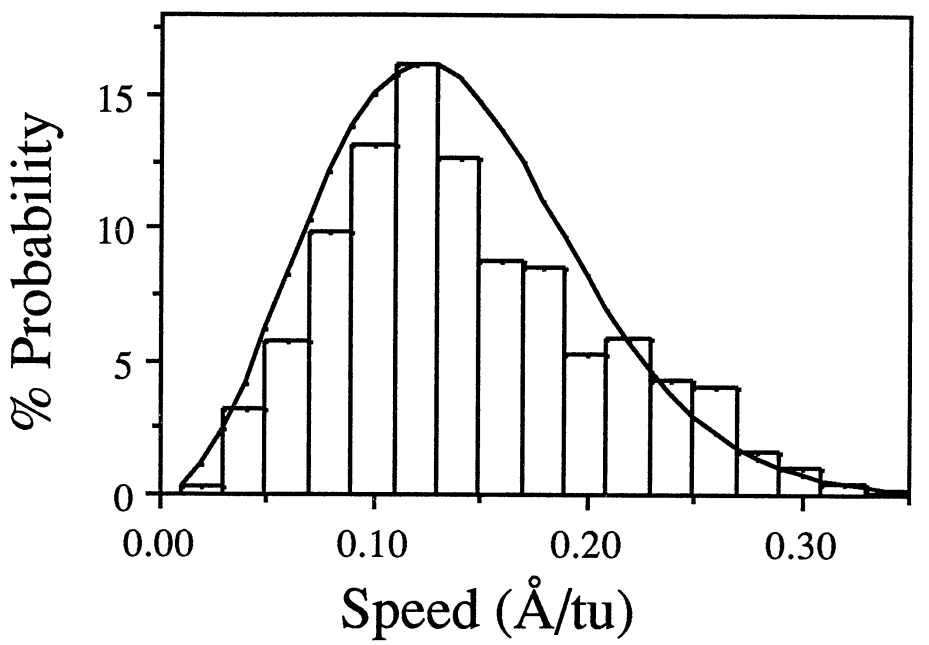
% Probability
15
10
5
0
0.00
0.10
0.20
0.30
Speed (Å/tu)

Figure 21. Distribution of Speeds for RDX at [Xe] = 19.1 mol dm^{-3}. The Maxwell-Boltzmann distribution (solid line) is calculated at 500 K. The atom types are as follows: (a) carbon atoms, (b) nitrogen atoms, (c) oxygen atoms, and (d) hydrogen atoms.

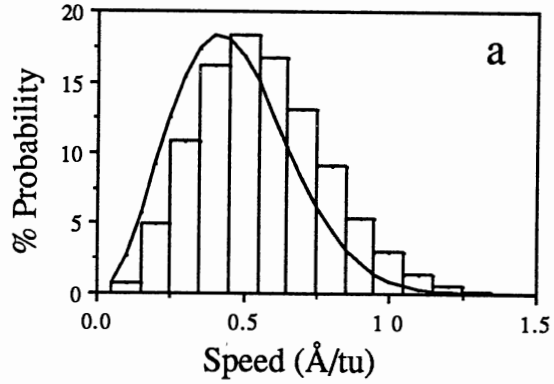
a
% Probability
Speed (Å/tu)
0
5
10
15
20
0.0
0.5
1 0
1.5

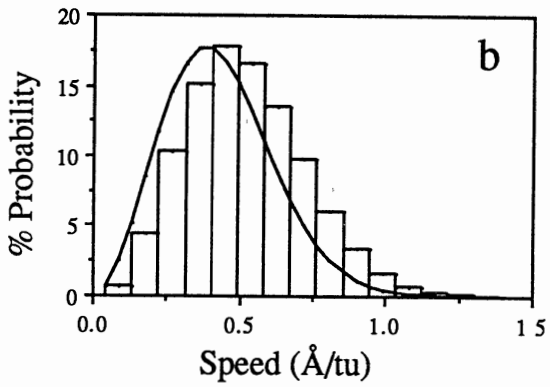
b
% Probability
Speed (Å/tu)
0
5
10
15
20
0.0
0.5
1.0
1 5

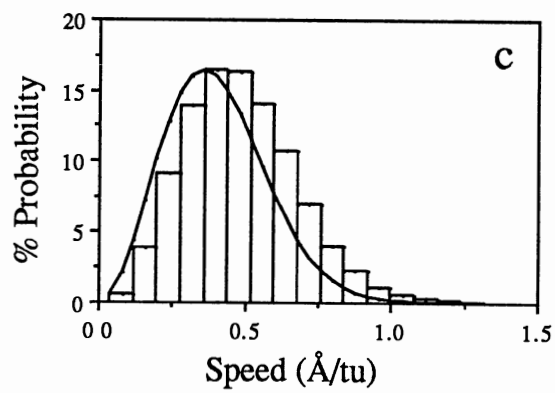
c
% Probability
Speed (Å/tu)
0
5
10
15
20
0 0
0.5
1.0
1.5

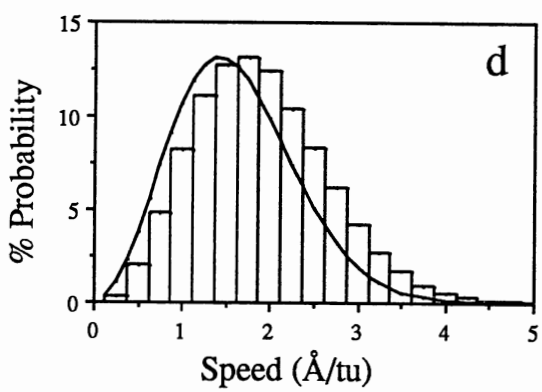
d
% Probability
Speed (Å/tu)
0
5
10
15
0
1
2
3
4
5

Figure 22. Distribution of Speeds for the Xe atoms at [Xe] = 19.1 mol dm^{-3}. The Maxwell-Boltzmann distribution (solid line) is calculated at a temperature is 500 K.

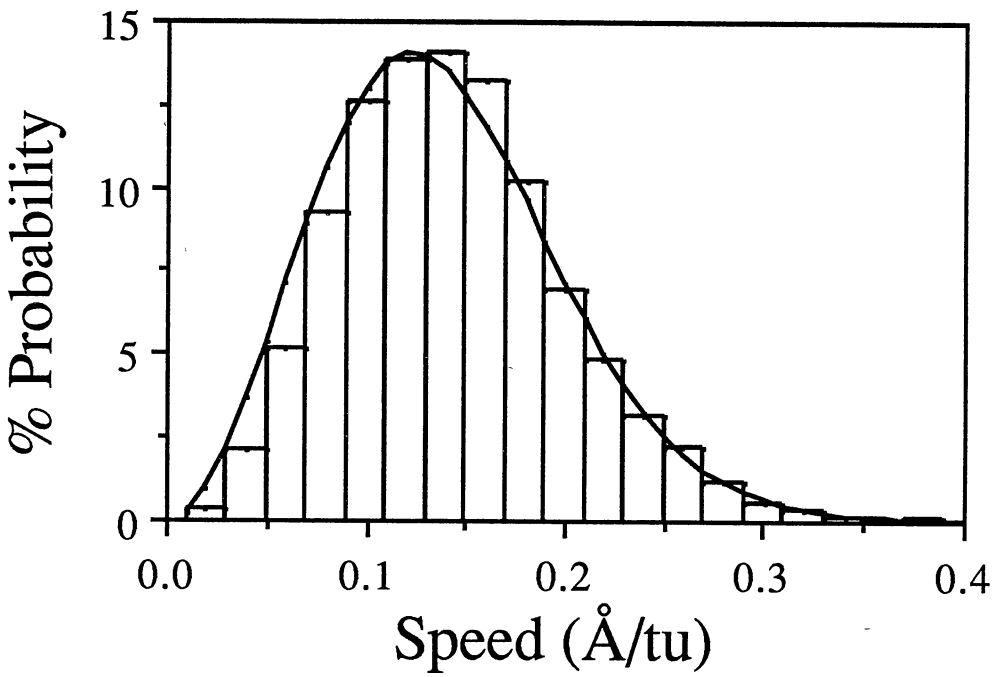
15
10
5
0
% Probability
0.0
0.1
0.2
0.3
0.4
Speed (Å/tu)

Figure 23. Time History of the Average Temperature for a Condensed-Phase Trajectory. The temperature for the trajectory is 510 K.

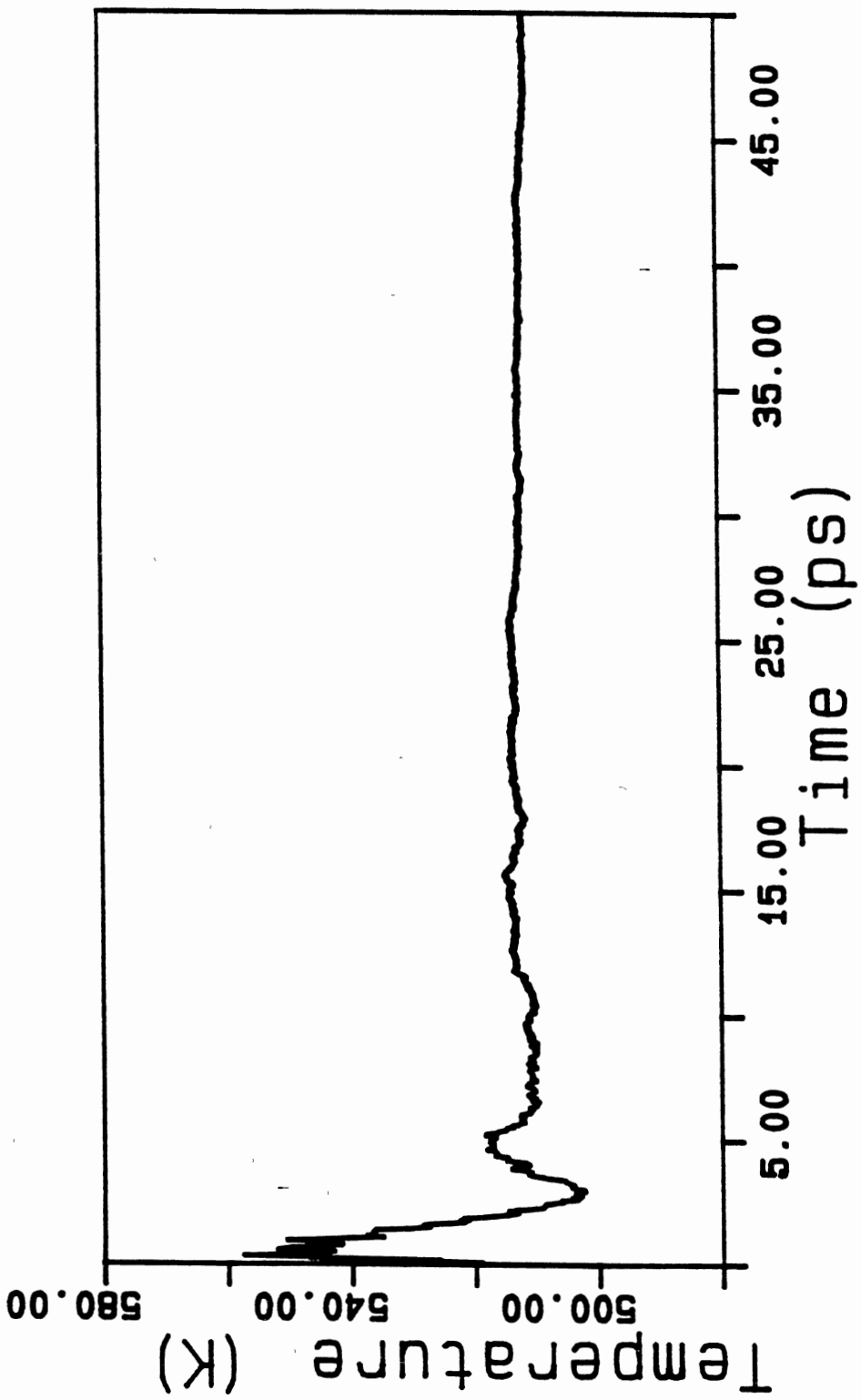
Temperature (K)
500.00
540.00
580.00
5.00
15.00
25.00
35.00
45.00
Time (ps)

Equilibrium Dynamics

Table XI lists the ensemble averages for the temperature (Eq. V.23) and translational energy (Eq. V.25), rotational energy (Eq. V.26), internal energy (Eq. V.28), and internal kinetic energy (Eq. V.30) of RDX for the eight different Xe concentrations studied. As the results in Table XI illustrates, the ensemble averaged internal kinetic energy is close to the theoretical value of (3N-6)/2 κT and the ensemble averaged rotational and translational energies are close to their theoretical value of 1.5κT. This suggests that thermal equilibrium has been fairly well established in each ensemble.

The gas-phase configurational distribution function for RDX is given by the Boltzmann distribution

$$P(\Theta) = \frac{\exp[-\beta V(\Theta)]}{\int d\Theta \exp[-\beta V(\Theta)]}, \qquad \text{(VIII.6)}$$

where $V(\Theta)$ is the gas-phase potential along the reaction coordinate. The potential-energy surface from $\Theta = 0°$ to $\Theta = 90°$ was calculated in Chapter VII. The calculated points were fit with a fifth order polynomial between these limits. Since the potential-energy surface is symmetric, the potential-energy surface from $\Theta = 90°$ to $\Theta = 180°$ was taken as the mirror image of the potential-energy surface from $\Theta = 0°$ to $\Theta = 90°$. The potential energy, $V(\Theta)$, is calculated by

$$V(\Theta) = \sum_{i=1}^{5} a_i \varphi^i \qquad \text{(VIII.7)}$$

$$\varphi = \begin{cases} \Theta \quad \text{for} \quad 0° \le \Theta \le 90° \\ 180°-\Theta \text{ for } 90° \le \Theta \le 180° \end{cases}, \qquad \text{(VIII.8)}$$

where Θ in Eq. VIII.8 is the value of the pucker coordinate and the a_i's are obtained from the non-linear least squares fit of the gas-phase potential-energy surface (Fig. 17a)

TABLE XI

ENSEMBLE AVERAGES FOR RDX IN A XE FLUID

[Xe][a]	<T>[b]	$\langle E_{kin} \rangle$[c]	<E(int)>[c]	<E(trans)>[c]	<E(rot)>[c]
3.1	510±16	28±4	69±7	1.3±0.6	1.3±0.4
6.3	510±32	32±4	69±8	1.5±0.4	1.5±0.5
9.4	490±31	31±3	78±7	1.7±0.4	1.4±0.2
11.0	510±29	31±4	76±8	1.8±0.3	1.5±0.3
12.6	510±25	28±3	71±8	1.4±0.3	1.6±0.3
14.2	510±26	30±4	72±7	1.3±0.2	1.5±0.4
15.8	490±29	28±4	69±7	1.7±0.4	1.7±0.4
19.1	520±28	36±4	84±6	1.8±0.3	1.8±0.3

a) Units are mol dm^{-3}.
b) Units are K.
c) Units are kcal mol^{-1}

obtained from the Monte Carlo simulation in chapter VII. The fitted coefficients are given in Table XII.

Gas-Phase Equilibrium Distribution The pucker coordinate Θ was calculated every 10 fs during each trajectory of the gas-phase ensemble and a histogram over 18 equal subintervals in the range 0° to 180° was accumulated. The probability distribution of the reaction coordinate, P(Θ), is plotted in Fig. 24. The Boltzmann probability distribution (Eq. VIII.6) is shown for comparison. Both distribution functions are normalized such that

$$\int P(\Theta)\, d\Theta = 1 \qquad \text{(VIII.9)}$$

where the limits of the integral are 0° to 180°. As can be seen, almost complete equilibration is achieved, P(0°) ≈ P(180°). The Boltzmann configurational distribution models the trajectory data fairly well. There is a slight underpopulation for the boat/twist conformations. The deviations at the end points are due to the definition of the Θ coordinate which is defined between 0° and 180°.

Condensed-Phase Equilibrium Distribution There has been some controversy as to the validity of applying the gas-phase configurational distribution function to solvent environments. Flory[155] suggests that for *n*-butane in a solvent, the average potential along the dihedral angle should correspond closely to its unperturbed value, that is, the gas-phase potential. Thus, the system of molecules may be pictured as populating the configuration space according to a Boltzmann distribution over the intramolecular energy, i.e., intermolecular effects are negligible. This behavior was also observed by Zhu and Robinson[42] for a series of model 4-atom molecules in a Lennard-Jones liquid.

Robertus *et al.*[32] and Pratt and Chandler[128-131] show that the gas-phase and condensed-phase configurational distributions are markedly different for a model potential of *n*-butane in solution. Robertus *et al.*[32] suggest that the local structure of a liquid can

TABLE XII

COEFFICIENTS FOR THE POTENTIAL-ENERGY SURFACE OF RDX

a_0 =	-5.4446×10^{-2}
a_1 =	1.8150×10^{-3}
a_2 =	7.5359×10^{-3}
a_3 =	-1.7699×10^{-4}
a_4 =	1.4767×10^{-6}
a_5 =	-4.1531×10^{-9}

a) Units are kcal mol^{-1}.

Figure 24. Configurational Distribution of Gas-Phase RDX. The Boltzmann distribution (solid line), calculated at a temperature of 500 K, is shown for comparison.

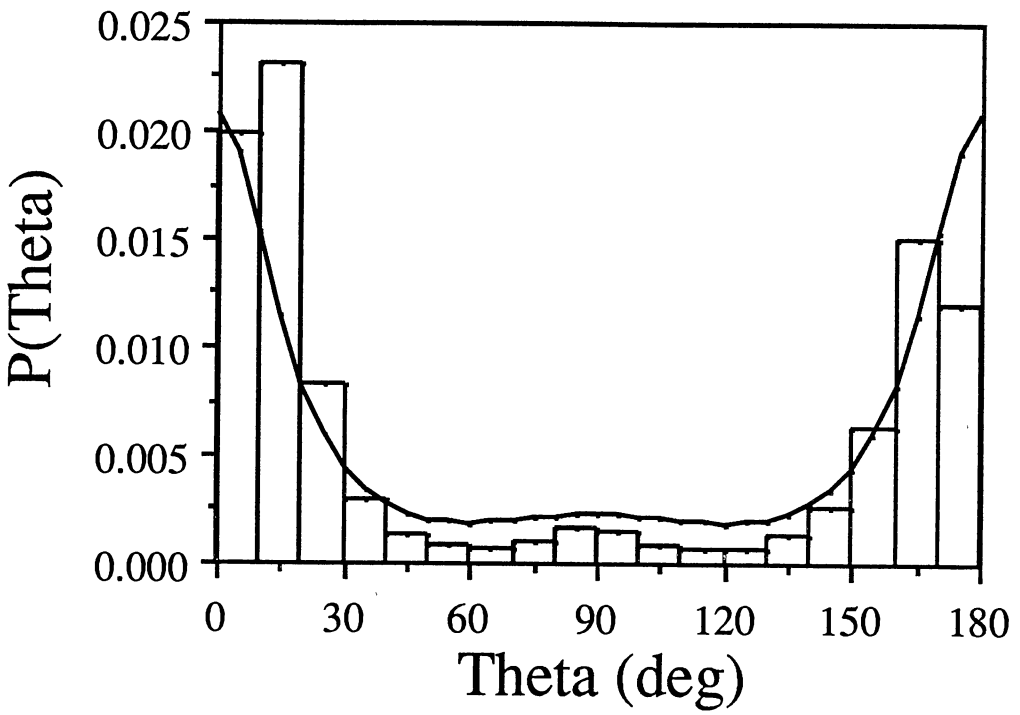
0.025
0.020
0.015
0.010
0.005
0.000
P(Theta)
0
30
60
90
120
150
180
Theta (deg)

sometimes accommodate one isomer preferentially to another. They suggest that the liquid structure is more easily obtained when the *n*-butane molecule is in the *gauche* isomer since this configuration is more "spherical" compared to the *trans* isomer. Zhu *et al.*[43] and Berne *et al.*[44] observed similar results for a quasi-diatomic molecule in which the configurational distribution is biased towards the contracted isomer due to its smaller volume.

The distributions for different solvent concentrations, [Xe] = 6.2 mol dm^{-3}, [Xe] = 14.2 mol dm^{-3}, and [Xe] = 19.1 mol dm^{-3} are plotted in Figs. 25(a-c), respectively. The Boltzmann configurational distribution (Eq. VIII.6) is shown for comparison. All distributions have been normalized according to Eq. VIII.9.

At [Xe] = 6.2 mol dm^{-3}, fair configurational equilibration has occurred in the time period calculated (as evidenced by P(0°) being almost equal to P(180°)). The Boltzmann distribution models the molecular dynamics simulation results fairly well over the region $15° < \Theta < 165°$. As the solvent concentration is increased, the distribution starts to show more deviation from the gas-phase distribution (Fig. 24) in the region of $15° < \Theta < 165°$. Also, configurational equilibration is not as complete as evidenced by P(0°) being only about half of P(180°). The interesting feature though is that as the solvent concentration increases, the probability of the boat/twist conformation increase. The probability of the boat/twist structure, P(90°), is ca. 1.6 time the gas-phase value (see Fig. 24) at [Xe] = 6.2 mol dm^{-3} and ca. 3 times the gas-phase value at [Xe] = 19.1 mol dm^{-3}.

The equilibrium constant is $K_{eq} = \frac{[chair]}{[boat/twist]}$, where [chair] and [boat/twist] are the concentration of the chair and boat/twist conformations, respectively. The boat/twist concentration is obtained by integrating over the configurational distribution from $\Theta = 60$ to 120°, while the chair concentration is obtained by integrating over the conformational distribution from $\Theta = 0°$ to 60° and $\Theta = 120°$ to 180° and dividing by two. The value for the equilibrium constant for the chair-boat/twist inversion for the gas-phase, [Xe] = 6.2 mol dm^{-3}, [Xe] = 14.2 mol dm^{-3}, [Xe] = 19.1 mol dm^{-3} are 5.3, 3.7, 2.4, 1.5,

Figure 25. Configurational Distribution of Condensed-Phase RDX. The Boltzmann distribution (solid line), calculated at a temperature of 500 K, is shown for comparison. The solvent concentrations are: (a) [Xe]=6.3 mol dm^{-3}; (b) [Xe] = 14.2 mol dm^{-3}; (c) [Xe]=19.1 mol dm^{-3}.

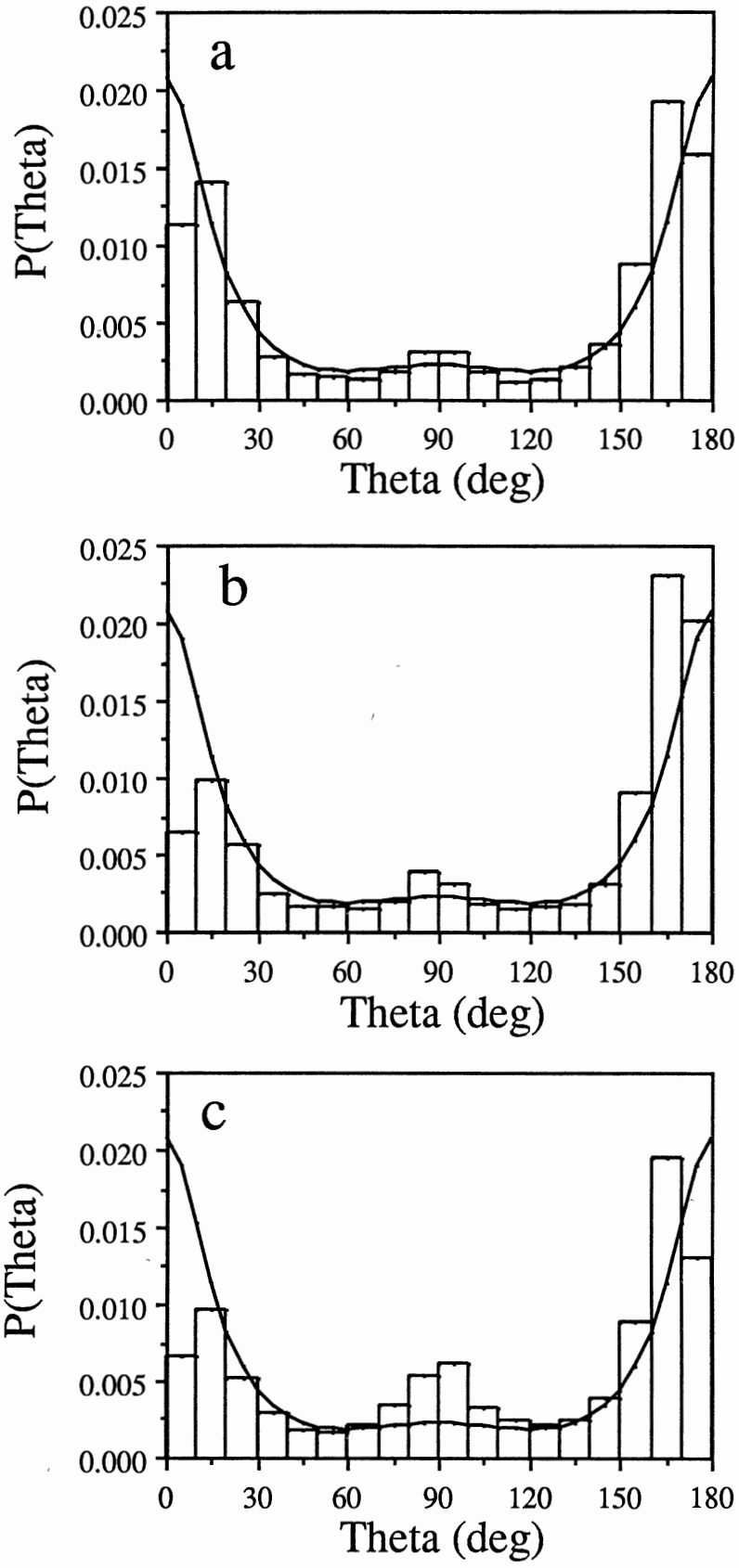
a
b
c
P(Theta)
Theta (deg)
0.025
0.020
0.015
0.010
0.005
0.000
0
30
60
90
120
150
180

respectively. Thus, for RDX in this simple Lennard-Jones fluid, we observe that the gas-phase configurational distribution does not describe the condensed-phase configurational distributions very well at high solvent concentrations. One explanation for this results is that the volume of the boat/twist conformation is much smaller than that for the chair structure, as will be shown later. Therefore, the entropy or "size" effect, discussed previously[32,43-44,128-131], appears to play a role in the equilibrium dynamics of condensed-phase RDX.

Chair-Boat/Twist Ring Inversion Rate Constants

The chair→boat/twist inversion process can be followed by calculating the time history of the Θ pucker coordinate (Eq. VII.2). The rate constant for the inversion process can be obtained by non-linear least-squares fitting

$$\frac{N(t)}{No} = \exp[-k_{uni}t], \qquad \text{(VIII.10)}$$

where N(t) is the number of lifetimes for RDX in the chair conformation at time t, No is the total number of lifetimes for RDX in the chair conformation, and k_{uni} is the chair→boat/twist rate constant. A trajectory is assumed to isomerize when the RDX molecule passes over the barrier and through the equilibrium configuration of the product state (the boat/twist conformation). The lifetime is taken as the time between the first and last inner turning point of the pucker coordinate Θ in the reactant state. The deviations between the lifetime distribution obtained from the molecular dynamics simulations and the exponential fit are between 6-10% for all cases studied.

Gas-Phase Results. Figure 26 illustrates the time history of the pucker coordinate Θ for a typical gas-phase trajectory. The RDX molecule is initially in the chair conformation for the first 8 ps after which it experiences 5 ring inversions. The molecule

Figure 26. Time History of the Pucker Coordinate Θ for a Gas-Phase Trajectory at 500 K.

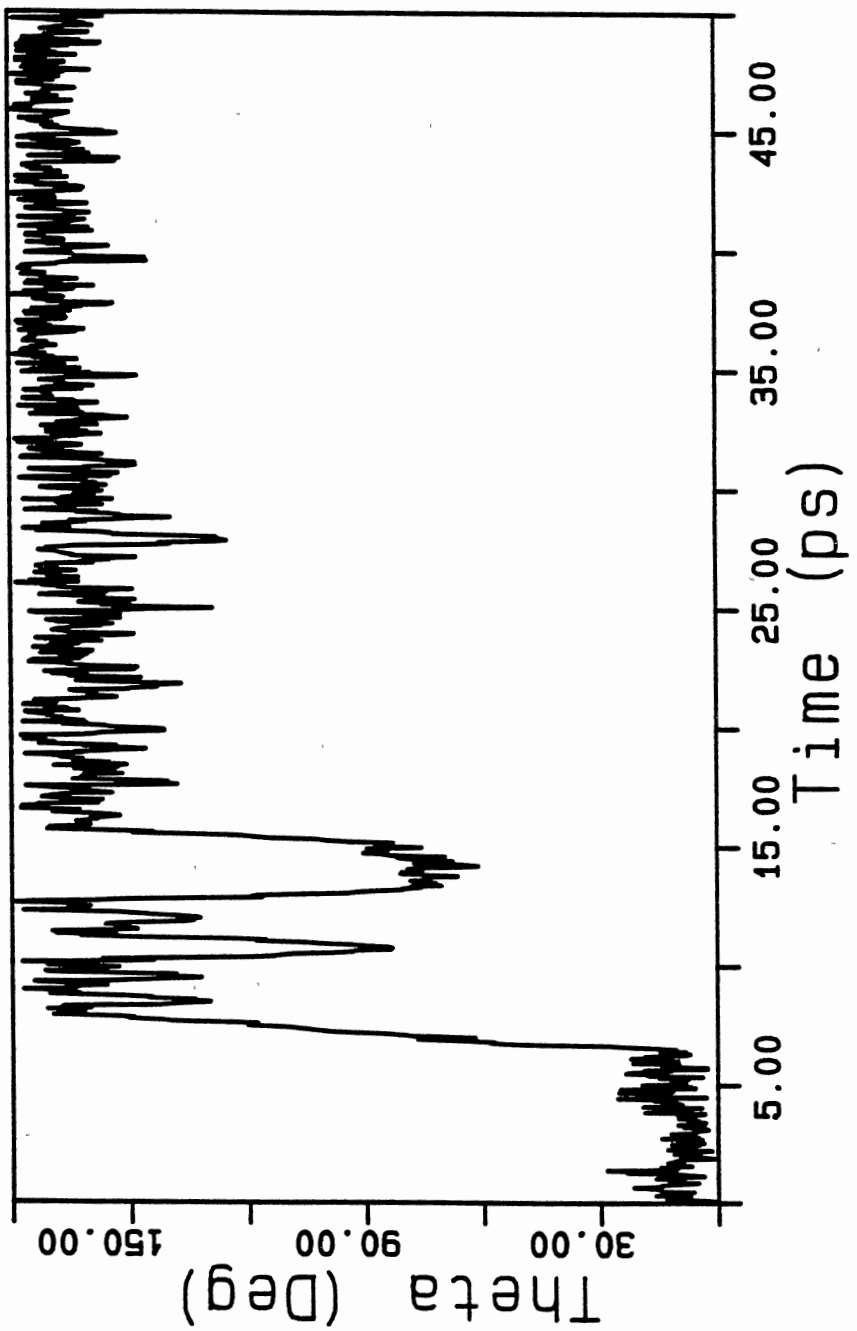
Theta (Deg)
30.00
90.00
150.00
5.00
15.00
25.00
35.00
45.00
Time (ps)

remains in the the inverted-chair conformation for the final 35 ps of the trajectory. Figure 27 shows the distribution of lifetimes for the gas-phase ensemble. The rate constant for the chair→boat/twist inversion process obtained from Eq. VIII.10 for gas-phase RDX is 1.2×10^{11} s^{-1}.

Condensed-Phase Results. Figure 28 shows the time history of the pucker coordinate for a typical trajectory in the condensed-phase. The RDX molecule experiences quit a few inversions during the 50 ps trajectory. This type of behavior was common to all the trajectories calculated at the eight different Xe solvent concentrations.

The distribution of lifetimes and the fitted exponential decay curve for the eight different solvent densities studied are shown in Fig. 29(a-h). The values for the rate constants obtained from Eq. VIII.10 at the different solvent densities are given in Table XIII.

Pressure Dependence of the Ring Inversion Rate Constant

The rate constant, k_{uni}, as a function of the Xe concentration are shown in Fig. 30. At low concentration (inertial regime[106,108-112]), the ring inversion rate constant, k_{uni}, obeys Lindemann behavior, that is, k_{uni} is an increasing function of the bath gas concentration [Xe].

At [Xe] = 6.3 mol dm^{-3}, the rate constant is a maximum and starts to decrease as the solvent concentration increases. This turnover in k_{uni} (Kramer's turnover[114]) has been seen in a number of isomerization processes[39-40,113,124,139]. This behavior is usually attributed to frictional effects of the solvent on the reaction coordinate. Therefore, the isomerization can be described as a diffusive process, i.e., the rate constant decreases as the solvent density increases[108-114]. In RDX, the three exocyclic NO_2 groups (see Fig. 15), which are coupled directly to the reaction coordinate, must sweep out a large volume as the ring inversion proceeds.

Figure 27. Lifetime Distribution for the Chair Conformation of RDX in the Gas Phase at 500 K. The solid line represents the exponential fit from which the rate constant can be obtained.

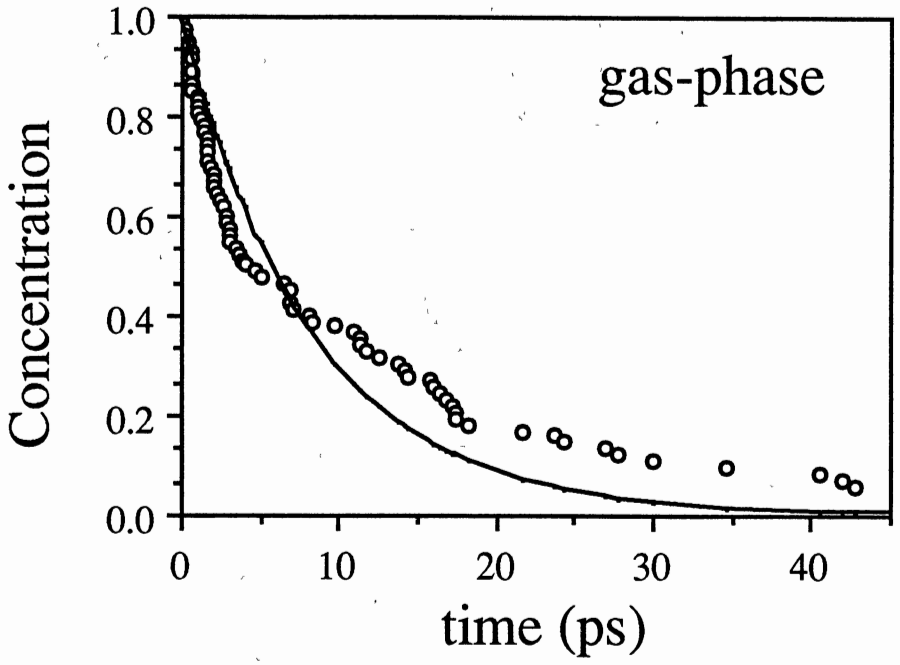
gas-phase
Concentration
time (ps)
1.0
0.8
0.6
0.4
0.2
0.0
0
10
20
30
40

Figure 28. Time History of the Pucker Coordinate Θ for a Condensed-Phase Trajectory at 500 K.

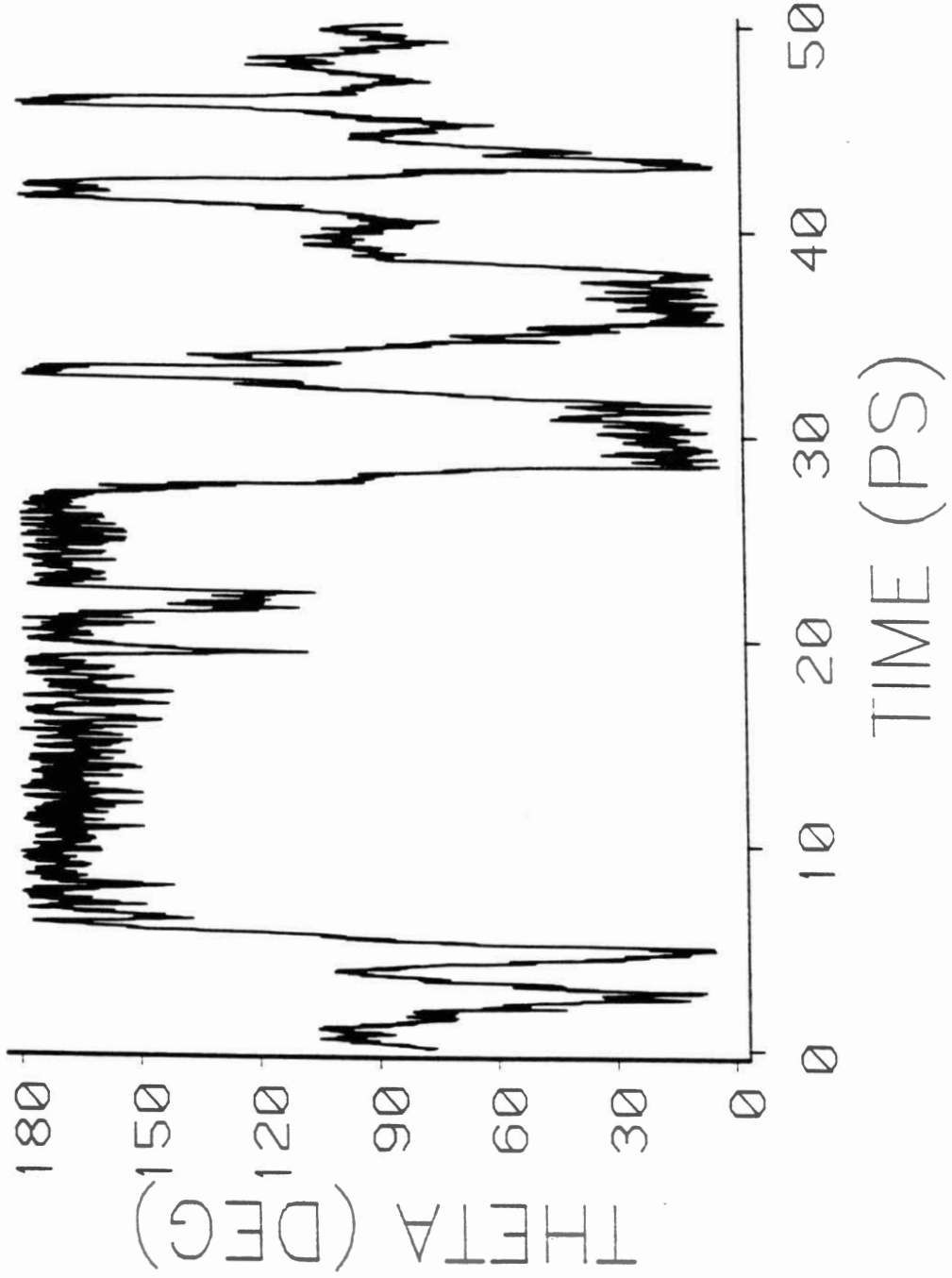
THETA (DEG)
180
150
120
90
60
30
0
0
10
20
30
40
50
TIME (PS)

Figure 29. Lifetime Distributions for the Chair Conformation of RDX in theCondensed-Phase at 500 K. The Solvent Concentration are: (a) [Xe] = 3.1 mol dm^{-3}; (b) [Xe] = 6.3 mol dm^{-3}; (c) [Xe] = 9.4 mol dm^{-3}; (d) [Xe] = 11.0 mol dm^{-3}; (e) [Xe] = 12.6 mol dm^{-3}; (f) [Xe] = 14.2 mol dm^{-3}; (g) [Xe] = 15.8 mol dm^{-3}; (h) [Xe] = 19.1 mol dm^{-3}. The solid lines represent the exponential fit from which the rate constant can be obtained.

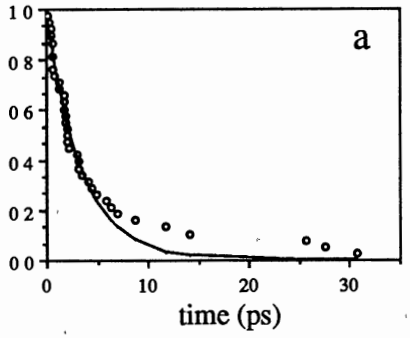
a
1.0
0.8
0.6
0.4
0.2
0.0
0
10
20
30
time (ps)

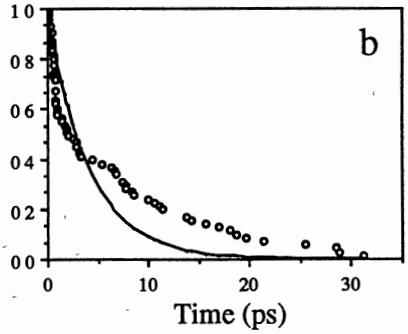
b
1.0
0.8
0.6
0.4
0.2
0.0
0
10
20
30
Time (ps)

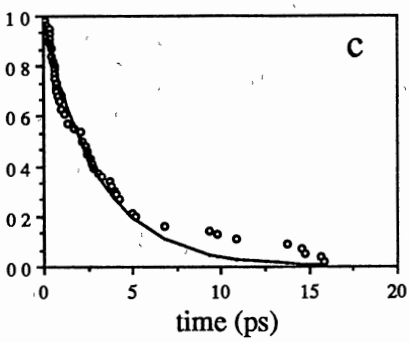
c
1.0
0.8
0.6
0.4
0.2
0.0
0
5
10
15
20
time (ps)

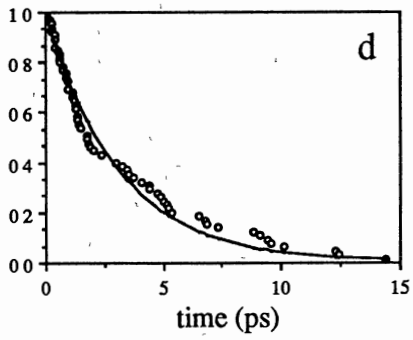
d
1.0
0.8
0.6
0.4
0.2
0.0
0
5
10
15
time (ps)

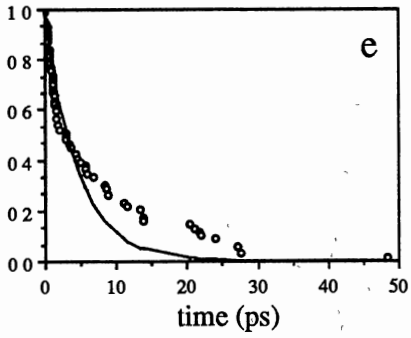
e
1.0
0.8
0.6
0.4
0.2
0.0
0
10
20
30
40
50
time (ps)

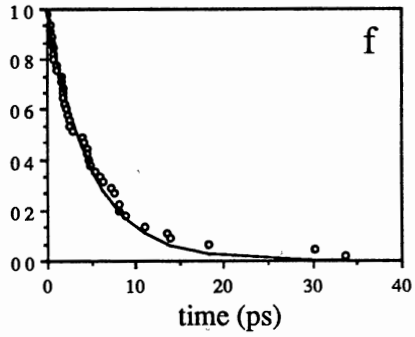
f
1.0
0.8
0.6
0.4
0.2
0.0
0
10
20
30
40
time (ps)

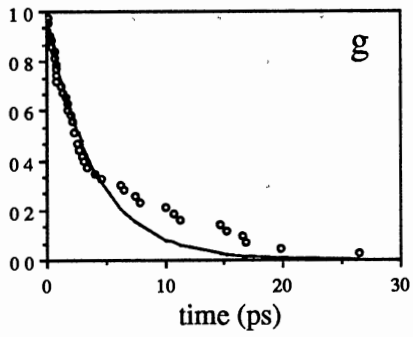
g
1.0
0.8
0.6
0.4
0.2
0.0
0
10
20
30
time (ps)

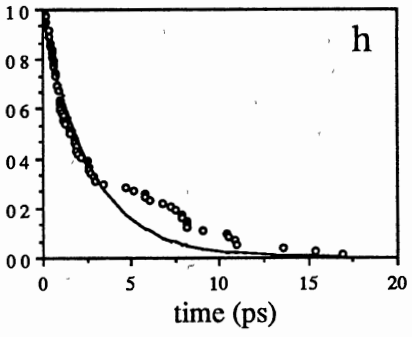
h
1.0
0.8
0.6
0.4
0.2
0.0
0
5
10
15
20
time (ps)

TABLE XIII

RATE CONSTANTS FOR THE CHAIR→BOAT/TWIST RING INVERSION OF RDX IN A XE FLUID

[Xe] mol dm^{-3}	$k_{chair \rightarrow boat/twist}$ (s^{-1})	
0.0[a]	1.2×10^{11}	(75)[b]
3.1	2.9×10^{11}	(35)
6.3	4.4×10^{11}	(59)
9.4	3.3×10^{11}	(48)
11.0	3.2×10^{11}	(59)
12.6	2.2×10^{11}	(57)
14.2	2.0×10^{11}	(42)
15.8	2.5×10^{11}	(39)
19.1	3.7×10^{11}	(61)

a) Taken from the gas-phase results.
b) The numbers in parentheses are the number of lifetimes for the corresponding ensemble.

Figure 30. Chair→Boat/Twist Rate Constant Versus Solvent Concentration for RDX.

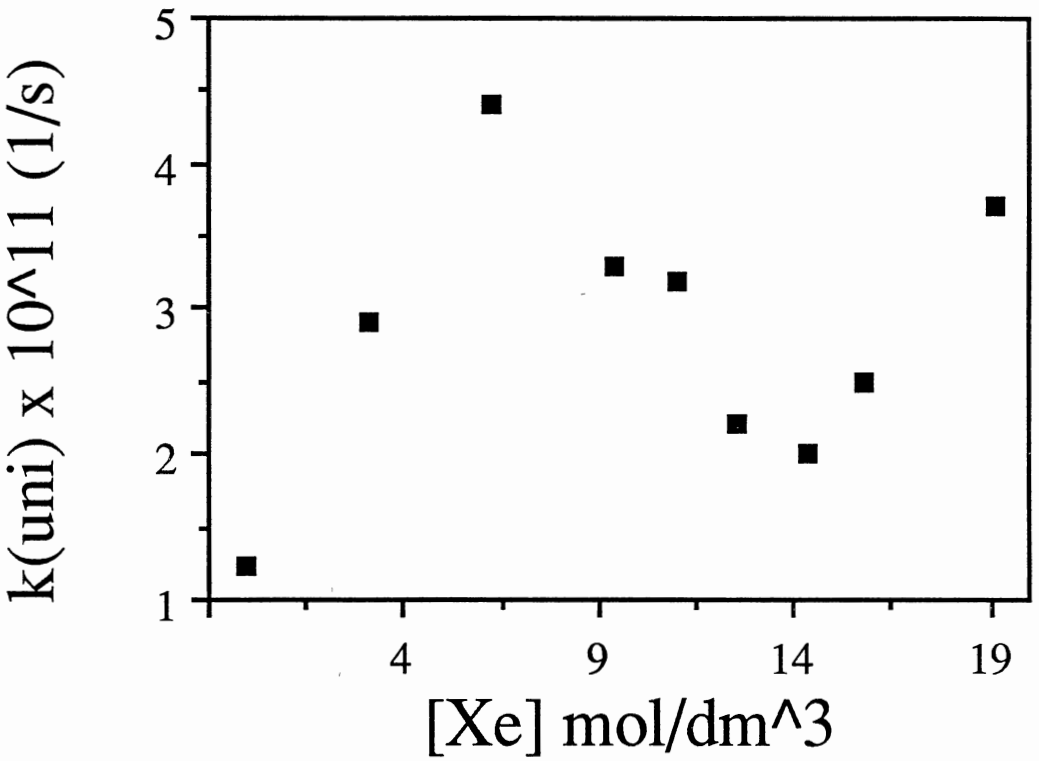
k(uni) x 10^11 (1/s)
5
4
3
2
1
4
9
14
19
[Xe] mol/dm^3

For hexahydro-1,3,5-trimethyl-1,3,5-triazine[147] (replace the three NO_2 groups of RDX with three CH_3 groups), the rate constant for ring inversion is lower (higher free energy barrier) in the solution phase[151] as compared with the gas-phase[147]. This increase in the free energy barrier is attributed to the large volume that the bulky methyl groups have to sweep out for inversion to occur[147].

The chair→boat/twist rate constant, k_{uni}, decreases until it reaches a minimum at [Xe] = 14.2 mol dm^{-3}. As the solvent concentration increases above [Xe] = 14.2 mol dm^{-3}, k_{uni} starts to increase. A frequently invoked concept, the activation volume $\Delta V^{\dagger}$ is employed to study deviations from Lindemann behavior at high solvent concentration[105-106,108,113,120-121]. The activation volume is defined as[105]

$$\Delta V^{\dagger} = -\kappa T \left(\frac{\partial (\ln k)}{\partial P} \right), \qquad \text{(VIII.11)}$$

where P is the pressure. The activation volume is a measure of the difference between the excluded volume of the transition-state structure and that of the reactant geometry[105]. Ladanyi and Hynes[121] have shown that variations in $\Delta V^{\dagger}$ generally arise from the change in solvent packing about the transition-state geometry as opposed to only changes in the reactant or transition-state geometry themselves. For a highly compressed solvent and a "tight" transition-state structure, $\Delta V^{\dagger}$ will be negative and according to Le Châtelier's principle the pressure of the solvent will lead to an equilibrium between the reactant and transition state in which the transition state is more favorable than at low density.

Using the transition state theory formulation, the unimolecular rate constant is given by[106]

$$k_{uni} = \frac{\kappa T}{h} K^{\dagger} \exp\left[\frac{-E_0}{\kappa T}\right], \qquad \text{(VIII.12)}$$

where E_o is the activation energy and $K^{\dagger}$ is the "pseudoequilibrium" constant for the assumed equilibrium between the reactant and transition-state configurations. Thus, for a "tight" transition-state structure and high solvent density, the equilibrium is expected to shift toward the transition state structure and $K^{\dagger}$ should increase[121]. An increase in $K^{\dagger}$ results in an increase in the unimolecular rate constant.

We have studied the "volume" of RDX as a function of the reaction coordinate at the different Xe concentrations. We can use the pucker coordinate Q (see Eq. III.4) except that the sum now extends over all 21 atoms of RDX. We let this coordinate be designated as Z so as to distinguish it from the true pucker coordinate Q. The volume of the molecule is than proportional to Z^3. Figure 31 illustrates the ensemble averaged Z coordinate as a function of the reaction coordinate for gas-phase RDX. As can be seen, the volume of the chair ($\Theta \sim 0°$) is much larger than the volume of the molecule in the transition-state region ($\Theta \sim 50°$).

We investigated the change in pressure just preceding and immediately following the minimum in the rate constant at [Xe] = 14.2 mol dm^{-3}. The pressure is calculated using Eq. V.24. The change in pressure, ΔP, in going from [Xe] = 12.6 mol dm^{-3} to [Xe] = 14.2 mol dm^{-3} (just before the minimum rate constant) is ~ 39 atm, whereas, when the solvent concentration is increased from [Xe] = 14.2 mol dm^{-3} to [Xe] = 15.8 mol dm^{-3} (immediately following the minimum rate constant), ΔP is ~ 54 atm. Also, as the solvent density is increased from [Xe] = 15.8 mol dm^{-3} to [Xe] = 19.1 mol dm^{-3}, ΔP is ~ 178 atm. These large increases in pressure represent an increase in the average Xe-Xe interactions (see Eq. V.24) which would result in the structure with the smaller volume being more favorable.

The "tight" transition state and increased Xe-Xe interactions, both strongly suggest that the activation volume is a plausible explanation for the increase in the chair→boat/twist inversion rate constant at high solvent concentrations.

Figure 31. Radius of Gas-Phase RDX as a Function of the Reaction Coordinate.

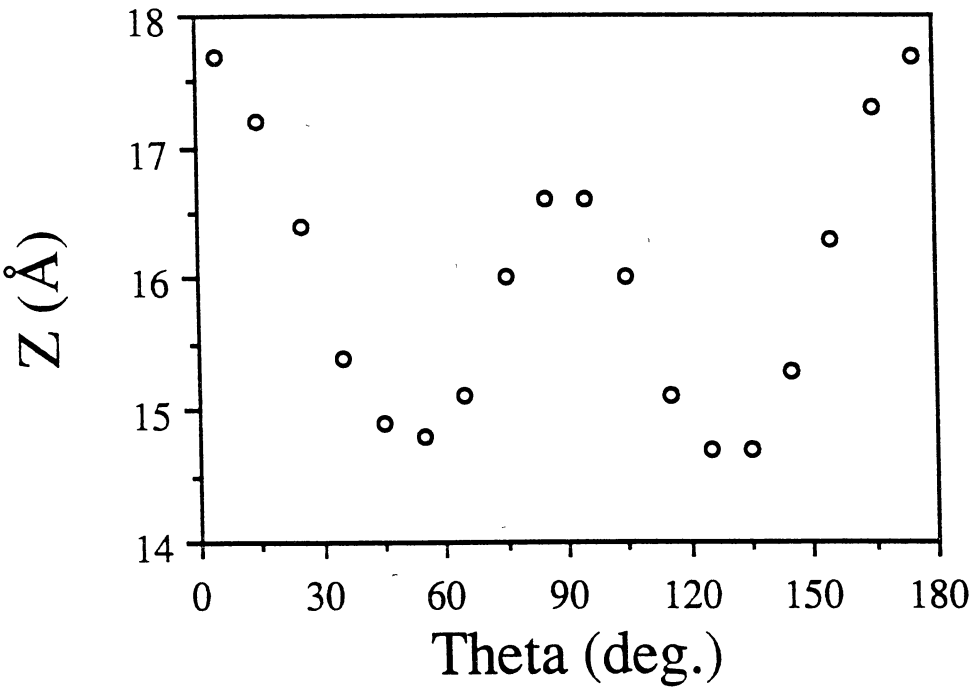
18
17
16
15
14
Z (Å)
0
30
60
90
120
150
180
Theta (deg.)

Conclusions

We have used molecular dynamics simulations to study the solvent effects on the equilibrium properties and the chair→boat/twist ring inversion rate constant at 500 K for eight Xe solvent concentrations.

The configurational distributions for RDX in the gas and condensed-phases were shown to be markedly different. The results show that as the solvent density increases, the probability distributions shift towards the boat/twist conformations. This is in accord with the results obtained for other isomerizations processes. The equilibrium constant for the chair-boat/twist ring inversion of RDX in the gas-phase and in the condensed phase ([Xe] = 19.1 mol dm^{-3}) is 5.3 and 1.5, respectively.

The rate constant for ring inversion, k_{uni}, obey Lindemann behavior at low solvent concentrations. As the solvent concentration increases, a maximum in the rate constant is observed after which it becomes a decreasing function of the solvent concentration (Kramer's turnover). We attribute this behavior to the bulky exocyclic NO_2 groups which are directly coupled to the reaction coordinate and must sweep out a large volume during the ring inversion process. At high solvent concentrations, k_{uni} increases with increasing solvent density. The behavior at high solvent densities was attributed to a negative volume of activation due to the "tight" transition state and the increase in the average Xe-Xe interaction which results in the "smaller" structure being favored.

Unfortunately, there are no experimental data for RDX with which to compare, but comparison with a similar system[121] yield qualitatively correct results.

CHAPTER IX

MOLECULAR DYNAMICS SIMULATIONS OF THE *CIS —TRANS* ISOMERIZATION OF HONO IN SOLUTION

Introduction

In this chapter, we discuss the effects of an Ar solvent on the *cis-trans* isomerization of nitrous acid (HONO). HONO is among the simplest of molecules to experience isomerization. Also, much is know about the potential-energy surface of HONO both experimentally[87-93] and theoretically[94-104]. The reaction coordinate has been shown to be primarily the dihedral angle.

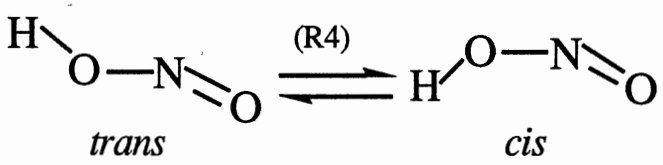

The *cis* isomer is slightly higher in energy than the *trans* isomer. Therefore, if the reaction could be described by a statistical thermodynamic theory, the rate constant for the *trans* →*cis* isomerization process should be about equal to that of the reverse process *cis*→*trans*.

The canonical distribution is fundamental to many of the presently accepted theories of chemical reactions[202]. This assumes that the solute and solvent are in perfect thermal equilibrium along the reaction coordinate. Zhu and Robinson[43] have recently shown that this might not be correct for solutes which undergo rapid local acceleration compared to the solvent atoms. The effect of non-equilibrium in barrier crossing processes is that the

solute cannot keep in perfect thermal equilibrium with the solvent at all points on the reaction coordinate, especially in the region of the barrier where the forces are large. Zhu and Robinson[43] show that the deviations from canonical behavior increase with increasing barrier height and the difference in mass between the reacting system and the bath atoms.

In a recent review of simple reactions in solution, Wilson[36a] discussed the importance of the process of climbing to the barrier top since this process dominates the reaction time. Nitzan and co-workers[153-154] showed that at low viscosity or density when the energy accumulation step is dominant, the dynamics of the system in the reactant well could play an important role in the reaction dynamics. Also, in non-Markovian regimes, that is, when the solvent does not act impulsively on the reacting molecule, the dynamics distant from the transition state could play an important role in the isomerization process. Molecular dynamics simulations, although time consuming, make no assumptions concerning thermal equilibrium between the solvent particles and the reacting species since the solvent is calculated explicitly.

To date, most molecular dynamics simulations on *cis—trans* isomerization reactions have used model systems with certain internal coordinates constrained to their equilibrium values. Studies have shown that the presence of rigid bonds and bending angles may lead to significant reductions in the isomerization rates[20,45-48]. Helfand *et al*[43] have shown that for chain molecules, as the transforming bond rotates over the barrier, neighboring degrees of freedom can undergo distortions. These distortions can dramatically affect both the barrier crossing process and the equilibrium distributions.

Van Gunsteren *et al.*[20] studied the dynamics of a protein with and without constrains imposed on the internal coordinates. They showed that the magnitude of the fluctuations decrease by a factor of 2 and transitions between the different conformations are drastically reduced when internal constrains are employed. They suggest that in a closely packed system, excluded volume effects due to repulsive non-bonded interactions can induce strong coupling between the dihedral angle and bond angle degrees of freedom

. Dunfield and Whittington[47] and Johsi and Rao[48] suggest that coupling between angle bending and torsional modes is important for conformational flexibility of polysaccharides.

We have used molecular dynamics simulations to calculate the equilibrium configurational distribution and rate constants for the *cis→trans* and *trans→cis* isomerization of HONO in solution using a model intramolecular potential-energy surface which incorporates bond stretching, angle bending, and non-linear couplings.

Potential-Energy Surface

The intramolecular potential-energy surface calculated by Guan and Thompson[103] for HONO was employed. The potential is given by,

$$V = V_{HONO} + V_{solute\text{-}solvent} + V_{solvent\text{-}solvent} \qquad \text{(IX.1)}$$

where the intramolecular potential,

$$V_{HONO} = V_{Morse} + V_{bend} + V_{torsion} \qquad \text{(IX.2)}$$

is comprised of Morse stretches (Eq. V.10),

$$V_{Morse} = \sum_i D_{e_i} \left(1 - e^{-\alpha_i (r_i - r_i^o)}\right)^2, \qquad \text{(IX.3)}$$

with D_e, r^o, and α being the dissociation energy, equilibrium bond distance, and curvature parameter, respectively, harmonic bends (Eq. V.12),

$$V_{bend} = \sum_i \frac{1}{2} k_b (\theta_i - \theta_i^o)^2 \qquad \text{(IX.4)}$$

where k_b and θ_i^o are the bending force constant and equilibrium bending angle, and a six term cosine series,

$$V_{torsion} = a_o + a_1 \cos(\tau) + a_2 [\, 2\cos^2(\tau) - 1] + a_3 [\, 4\cos^3(\tau) - 3\cos(\tau)\,]$$
$$+ a_4 [\, 8\cos^4(\tau) - 8\cos^2(\tau) + 1\,]$$
$$+ a_5 [\, 16\cos^5(\tau) - 20\cos^3(\tau) + 5\cos(\tau)\,]. \qquad \text{(IX.5)}$$

A switching function of the form[203],

$$S_\tau = \frac{1}{2}(1-\cos(\tau)), \qquad \text{(IX.6)}$$

was used to smoothly vary the geometry and potential parameters between the *trans* and *cis* isomers. The importance of nonlinear coupling between the internal coordinates and the reaction coordinate has been addressed extensively for the dynamics and unimolecular reactions of polyatomic molecules[28,203-209]. The instantaneous "equilibrium" geometrical and potential parameters are given by

$$X_i^o = X_i^{cis} - (\, X_i^{cis} - X_i^{trans}\,)S_\tau, \qquad \text{(IX.7)}$$

where X_i^{trans} and X_i^{cis} are the value of the "ith" geometrical and potential parameters in the *trans* and *cis* conformations, respectively. The equilibrium coordinates, r^0 and Θ^o, and potential parameters, α and k_b are switched in this study.

For this potential-energy function, the barrier for the *trans*→*cis* isomerization is 9.6 kcal mol^{-1} which is much to high (16κT, where κ is the Boltzmann factor and T is the temperature) for a sufficient number of barrier crossings to occur at 300 K in a reasonable amount of computer time. A technique developed to study infrequent events is the reactive flux method[125] (see chapter III). This method is based on the time correlation description of the barrier crossing process. Since each trajectory is initiated at the barrier, they need

only be calculated for a short period of time until the reactive flux has reached a plateau value. Robertus *et al.*[32] developed another approach in which the configurational probability distribution is calculated from a molecular dynamics simulation with a zero barrier for the reacting molecule. The equilibrium constant can be obtained by multiplying the zero barrier distribution function and the Boltzmann factor, $\exp[-\beta V(\tau)]$, where $V(\tau)$ is the potential along the reaction coordinate and $\beta=(\kappa T)^{-1}$. Both of these methods assume that the solute and solvent remain in thermal equilibrium throughout the barrier crossing process, which might not be the case[43].

To overcome the high barrier but not introduce assumptions as to the behavior of the solute and solvent along the reaction coordinate, we scaled the torsional barrier to $1.41\kappa T$. Thus, our model potential-energy surface for HONO is representative of a low barrier height system[43c]. The bond stretching, angle bending, and coupling terms from the potential-energy function by Guan and Thomson[103] are retained. The values for the equilibrium internal coordinates and potential parameters are given in Table XIV and Table XV, respectively. The gas-phase torsional barrier is illustrated in Fig. 32. In the scaled potential, the *cis* isomer is 0.058 kcal/mol higher in energy than the *trans* isomer and the barrier is 0.84 kcal mol^{-1}.

The transition-state (τ=85.4°) structure was calculated using the gradient norm method (see Chapter V). The calculated values of the internal coordinates for the transition-state structures are given in Table XIV. The calculated frequencies for the three different structures, *cis* (τ=0°), *trans* (τ=180°), and transition state (τ=85.4°) are given in Table XVI.

The molecule-solvent and solvent-solvent interactions, $V_{\text{solute-solvent}}$ and $V_{\text{solvent-solvent}}$, are represented by Lennard-Jones 12-6 interactions

$$V_{L\text{-}J} = \sum_i \sum_j 4\varepsilon_{ij}\left\{\left(\frac{\sigma_{ij}}{r_{ij}}\right)^{12} - \left(\frac{\sigma_{ij}}{r_{ij}}\right)^{6}\right\}, \qquad \text{(IX.8)}$$

TABLE XIV

EQUILIBRIUM INTERNAL COORDINATES FOR HONO

bond	r^o (Å)		
	trans	cis	TS[a]
N=O	1.1665	1.1773	1.1723
N-O	1.3996	1.3776	1.3877
H-O	0.9539	0.9646	0.9597
bending angle		Θ (deg)	
	trans	cis	TS
O-N-O	111.38	113.94	112.76
H-O-N	107.89	111.61	109.90
dihedral angle		τ (deg)	
	trans	cis	TS
H-O-N-O	180.00	0.00	85.44

a) Values for the transition-state structure were obtained from the mimimization proceedure (see text).

TABLE XV

POTENTIAL PARAMETERS FOR THE INTRAMOLECULAR POTENTIAL-ENERGY SURFACE FOR HONO

bond	D_e (kcal/mol)	α ($Å^{-1}$)	
		trans	cis
N=O	115.0195	2.7553	2.6228
N-O	40.7985	2.1027	2.1364
H-O	78.8310	2.5629	2.4459

bending angle	K_Θ (kcal mol^{-1} rad^{-2})	
	trans	cis
O-N-O	249.1791	277.9544
H-O-N	107.2165	120.4446

dihedral angle	a_0[a]	a_1	a_2	a_3	a_4	a_5
H-O-N-O	0.4429	0.0524	-0.4039	-0.0232	-0.0108	-0.0012

a) units are kcal mol^{-1}.

Figure 32. Potential-Energy Barrier for *Cis*—*Trans* Isomerization for Gas-Phase HONO.

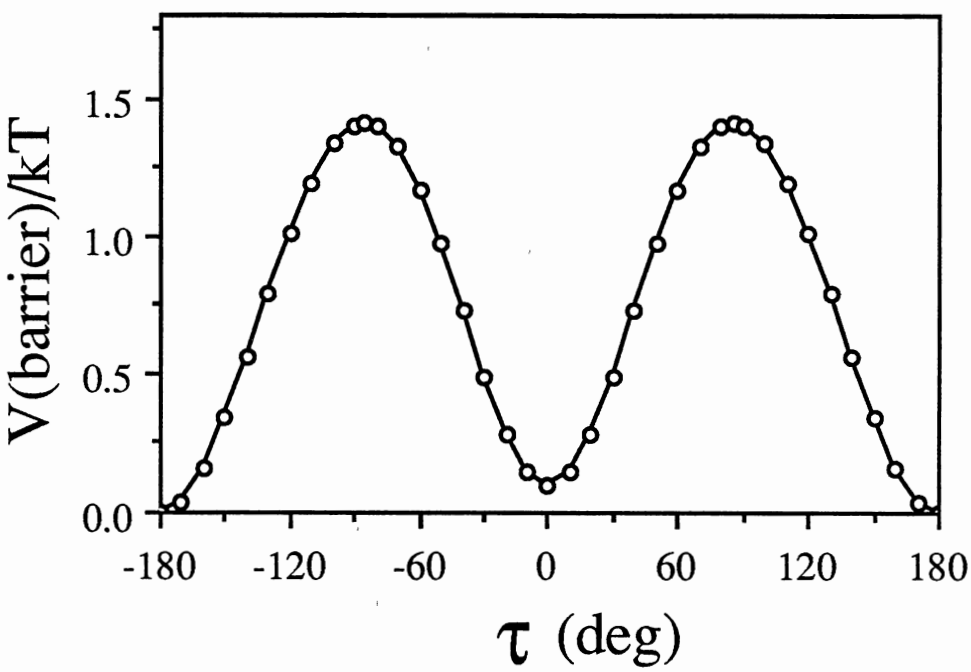
V(barrier)/kT
1.5
1.0
0.5
0.0
-180
-120
-60
0
60
120
180
τ (deg)

TABLE XVI

CALCULATED NORMAL MODE FREQUENCIES OF HONO[a]

	ν_1 (OH)	ν_2 (N=O)	ν_3 (HON)	ν_4 (NO)	ν_5 (ONO)	ν_6 (τ)
Trans						
previous calc.[b]	3591	1700	1263	845	541	537
present calc.	3589	1698	1262	844	540	162
Cis						
previous calc.[b]	3426	1641	1302	909	540	648
present calc.	3426	1640	1301	907	540	195
TS[c]						
present calc.	3500	1645	1299	888	545	161*i* [c]

a) Units are cm^{-1}.
b) Guan and Thompson, Chem. Phys., 139, 147 (1989).
c) The transition-state structure. The torsional coordinate, τ, is the reaction coordinate.

where r_{ij} is the distance, σ_{ij} is the atomic radius, and ε_{ij} is the Lennard-Jones well depth between atoms i and j which are calculated using the Lorentz-Berthelot mixing rules,

$$\sigma_{ij} = [\sigma_i + \sigma_j] \tag{IX.9}$$

and

$$\varepsilon_{ij} = \sqrt{\varepsilon_i \varepsilon_j}\ , \tag{IX.10}$$

where the σ_i and ε_i are the atomic radius and Lennard-Jones well depth for the ith atom. The solute-solvent and solvent-solvent potential parameters are given in Table XVII.

Computational Procedure

The system consists of one HONO molecule and 104 Ar solvent atoms using periodic boundary conditions (see Chapter V). The HONO molecule is initiated in the *trans* configuration and placed at the center of an fcc lattice of Ar atoms. Box lengths of 17.9817 Å and 16.6927 Å gave densities of ρ=1.20 g cm^{-3} and ρ=1.50 g cm^{-3} or reduces solvent densities ($\rho_{Ar}^* = \rho_{Ar}\sigma_{Ar}$) of 0.709 and 0.887, respectively. The atomic momenta are sampled from a thermal distribution (Eq. V.21) at 300 K. A trajectory is calculated by numerically solving Hamilton's equations of motion (Eqs. V.5-V.6) in Cartesian coordinates using an Adams[201] variable-order variable-step algorithm with an error tolerance of 5 x 10^{-5} which gives energy conservation of 0.05%. The system is annealed for 1.0 ps by periodically zeroing the atomic momenta. A warm up trajectory is calculated for 2.5 ps by periodically scaling the momenta to the desired ensemble temperature (Eq. V.22). After the warm up period, a new set of momenta are sampled from a thermal distribution at 300 K and a trajectory is calculated for 100-200 ps after 5 ps of equilibration. The phase-space coordinates are saved every 5 fs for subsequent analysis.

TABLE XVII

INTERMOLECULAR INTERACTIONS FOR HONO AND ARGON

intermolecular interactions[a]	ε^b	σ^c
Ar — N	0.133	3.36
Ar — O	0.171	3.18
Ar — H	0.064	3.11
Ar — Ar	0.238	3.41

a) The values were taken from Ref. 1.
b) Atomic polarizability units are kcal mol^{-1}.
c) Atomic radius units are Å.

The equilibrium dynamics and rate constants for the *cis*→*trans* and *trans*→*cis* isomerization processes are calculated.

Results and Discussions

The time-averaged value of the temperature for the two densities studies are given in Table XVIII. The time-averaged value of the internal energy (Eq. V.28), internal kinetic energy (Eq. V.30), translational energy (Eq. V.25), and rotational energy (Eq. V.26) are given in Table XVIII. All are close to their theoretical values, i.e., 3κT for the internal kinetic energy and 1.5κT for the translational and rotational energy.

Configurational Distribution

The torsional angle was calculated every 5 fs during each trajectory and a histogram of 10 equal subintervals was accumulated. The configurational distribution for the two densities are plotted in Figs. 33(a-b). The Boltzmann distribution for gas-phase HONO, given by[119]

$$\frac{\exp[-\beta V(\tau)]}{\int \exp[-\beta V(\tau)]}, \qquad \text{(IX.11)}$$

(where $V(\tau)$ is the gas-phase torsional barrier, $\beta = (\kappa T)^{-1}$, and the limits of integration are from 0 to 2π) is shown for comparison. All distributions have been normalized such that

$$\int \exp[-\beta V(\tau)] = 1 \qquad \text{(IX.12)}$$

where the limits are from 0 to 2π. The configurational probability distribution for HONO at ρ=1.20 g cm^{-3} (Fig. 33a) and at ρ=1.50 g cm^{-3} (Fig. 33b) is modeled fairly well by the Boltzmann distribution. The equilibrium constant is $K_{eq} = \frac{[cis]}{[trans]}$, where [*cis*] and [*trans*] are obtained by integrating the configurational probability distribution obtained from the

TABLE XVIII

TIME AVERAGES FOR HONO

$[Ar]^a$	<T> (K)	$<E(int)>^b$	$<E(kin)>^b$	$<E(trans)>^b$	$<E(rot)>^b$
1.20	316.2	4.12	2.07	1.00	0.95
1.50	286.4	4.47	2.23	0.87	0.92

a) Solution concentrations units are g cm^{-3}.
b) Energy units are kcal mol^{-1}.

Figure 33. Configurational Probability Distribution for HONO. (a) ρ=1.20 g cm^{-3}; (b) ρ=1.50 g cm^{-3}.

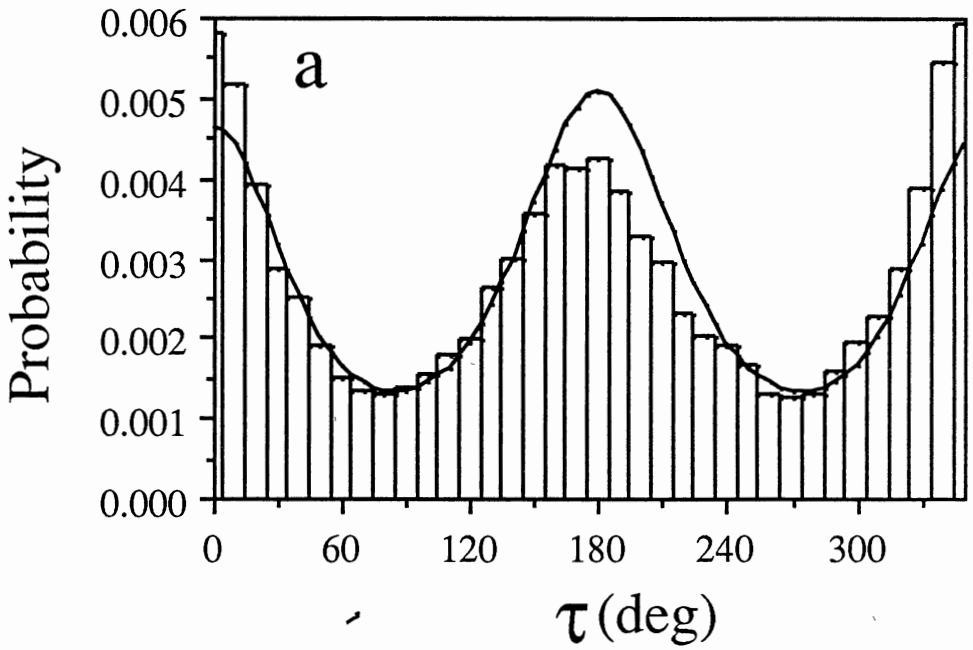
a
Probability
0.006
0.005
0.004
0.003
0.002
0.001
0.000
0
60
120
180
240
300
τ (deg)

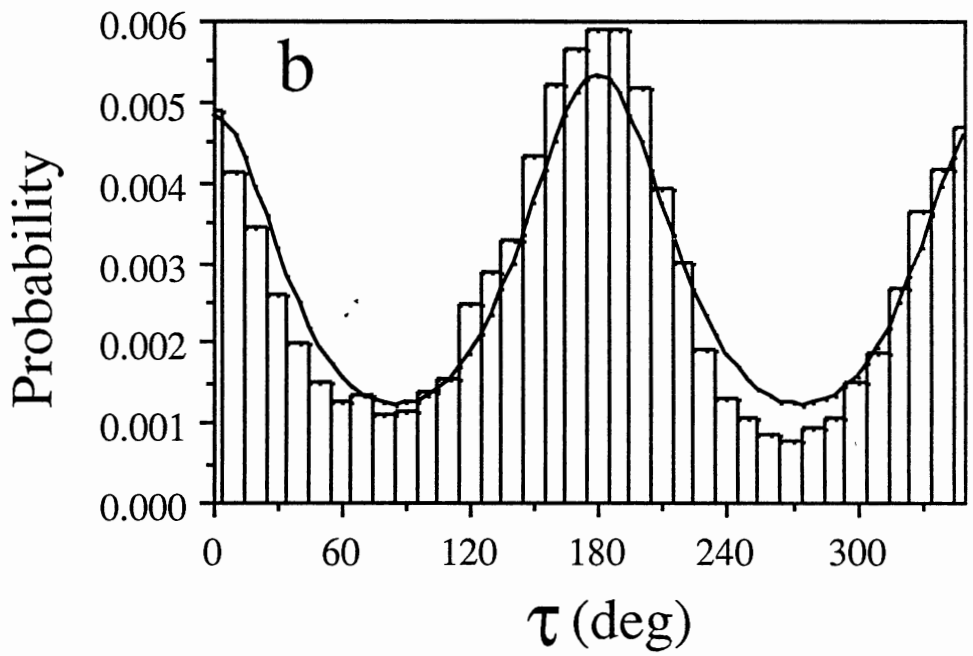
b
Probability
0.006
0.005
0.004
0.003
0.002
0.001
0.000
0
60
120
180
240
300
τ (deg)

molecular dynamics simulations over the *cis* and *trans* conformations. The molecule is assumed in the *trans* isomer when $85.4° \leq \tau \leq 265.4°$ and the *cis* isomer otherwise. The equilibrium constants for the *cis*→*trans* isomerization are calculated to be 1.1 and 0.7 for ρ=1.20 g cm^{-3} and ρ=1.50 g cm^{-3}, respectively. The gas-phase equilibrium constant, obtained from the Boltzmann probability distribution, is 0.89. These results show that HONO, in an Ar liquid, populates the configuration space according to a near Boltzmann distribution over the intramolecular energy of the gas-phase molecule.

Zhu *et al.*[42a], show that for the systems they studied, the Boltzmann distribution models the trajectory data well, which is in accord with the ideas suggested by Flory[155]. As was stated in Chapter VIII, there has been some controversy as to the validity of extending gas-phase principles to condensed-phase systems.

Solvent Structure

The solvent structure can be studied by calculating the argon-argon pair radial distribution function, given by[119]

$$g(r)_{Ar\text{-}Ar} = (4\pi\rho_{Ar}r^2)^{-1}\frac{dN(r)}{dr}, \qquad \text{(IX.13)}$$

where ρ_{Ar} is the number density of the bulk solvent and dN(r) is the number of solvent atoms in a radial distance r→r+dr of a tagged atom. The factor $(4\pi\rho_{Ar}r^2)^{-1}$ normalizes the function to unity at distances far from the tagged particle.

The argon-argon pair radial distribution functions, $g(r)_{Ar\text{-}Ar}$, at ρ=1.20 g cm^{-3} and ρ=1.50 g cm^{-3} are plotted in Figs. 34a and 34b, respectively. The first solvation shell extend to the first minimum, r_{min}, in $g(r)_{Ar\text{-}Ar}$ which corresponds to 5.42 Å and 5.22 Å for ρ=1.20 g cm^{-3} and ρ=1.50 g cm^{-3}, respectively. The average number of atoms constituting the first shell can be obtained by integrating $g(r)_{Ar\text{-}Ar}$ from r=0 to r=r_{min}. The

Figure 34. Argon-Argon Pair Radial Distribution Function. (a) ρ=1.20 g cm^{-3}; (a) ρ=1.50 g cm^{-3}.

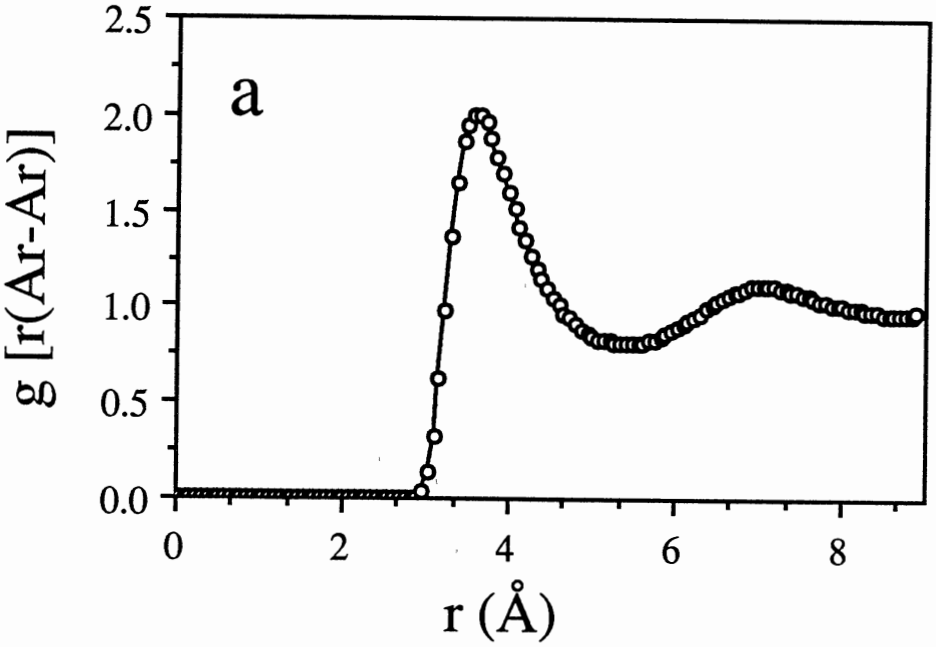
a
g [r(Ar-Ar)]
r (Å)
0.0
0.5
1.0
1.5
2.0
2.5
0
2
4
6
8

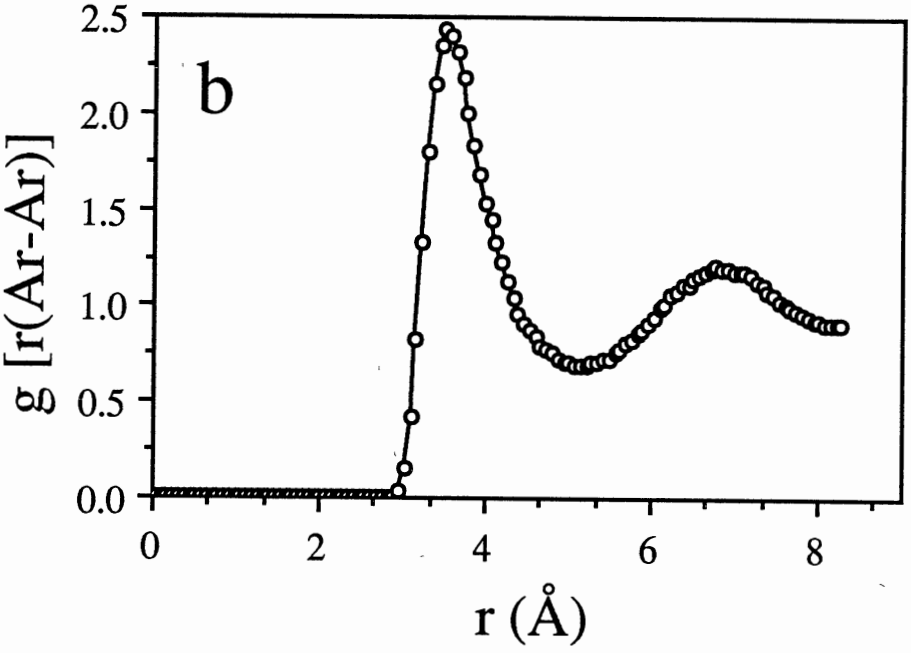
b
g [r(Ar-Ar)]
r (Å)
0.0
0.5
1.0
1.5
2.0
2.5
0
2
4
6
8

average number of solvent atoms in the first solvation shell is 10.9 ≈ 11 and 12.7 ≈ 13 for ρ=1.20 g cm^{-3} and ρ=1.50 g cm^{-3}, respectively.

Isomerization Rate Constants

Molecular Dynamics Rate Constants Since the system is comprised of only one isomerizing molecule, an ensemble was obtained using the method of Robinson and co-workers[41-43]. After each isomerization, i.e., *cis*→*trans* or *trans*→*cis*, a "new" trajectory is begun with the final configuration of the preceding isomerization as the initial configuration of the "new" trajectory. In this scheme, the time average replaces the ensemble average.

The lifetime of a trajectory is calculated as the time between the initial the final turning points in the reactant well provided the HONO molecule passes through the equilibrium position of the product well before returning to the reactant well. Thus, we account for barrier recrossings, that is, trajectories which proceed to the transition state but return to the equilibrium well instead of proceeding to products. The rate constant is obtained by fitting the computed lifetime distribution to

$$\left[\frac{N(t)}{N(0)}\right] = \exp[-kt], \qquad \text{(IX.14)}$$

where N(t) is the number of lifetimes at time t, N(0) is the total number of lifetimes, and k is the rate constant. The calculated lifetime distributions for the *cis*→*trans* and *trans*→*cis* isomerizations at ρ=1.20 g cm^{-3} and ρ=1.50 g cm^{-3} are plotted in Figs. 35(a-b) and 36(a-b), respectively. The deviations between the lifetime distributions and the exponential fit is between 8-10% for all distributions. The values of the rate constants for the *cis*→*trans* and *trans*→*cis* isomerization processes at the two densities are given in Table XIX. The trajectory at ρ=1.20 g cm^{-3} was run for 200 ps, thus, the greater number

Figure 35. Computed Lifetime Distributions for HONO at ρ=1.20 g cm^{-3}. (a) *Cis→Trans*; (b) *Trans→Cis*..

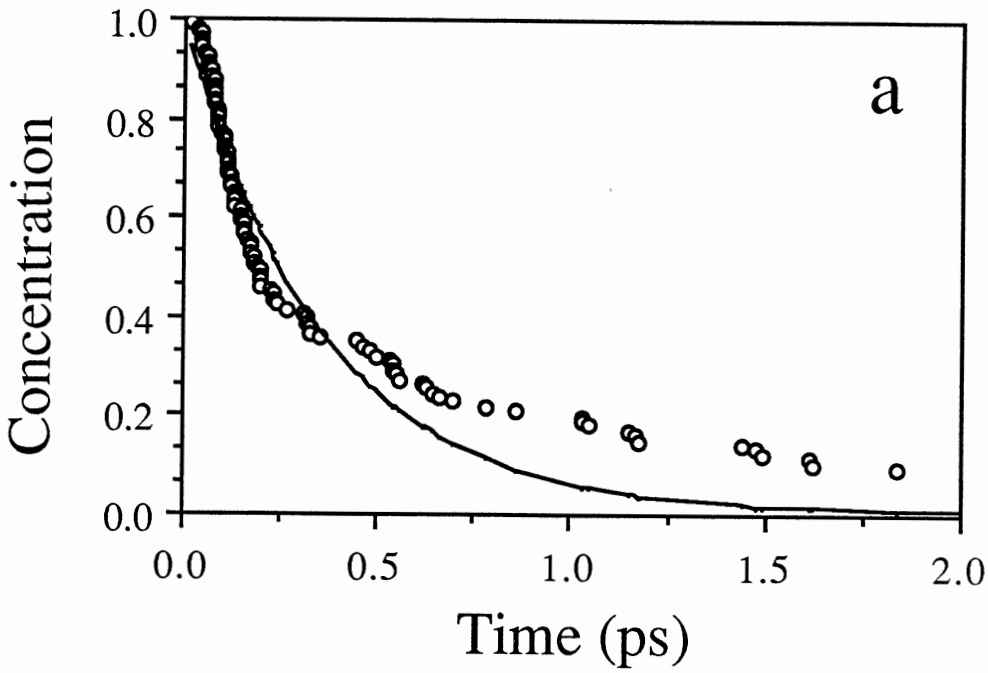
a
Concentration
1.0
0.8
0.6
0.4
0.2
0.0
0.0
0.5
1.0
1.5
2.0
Time (ps)

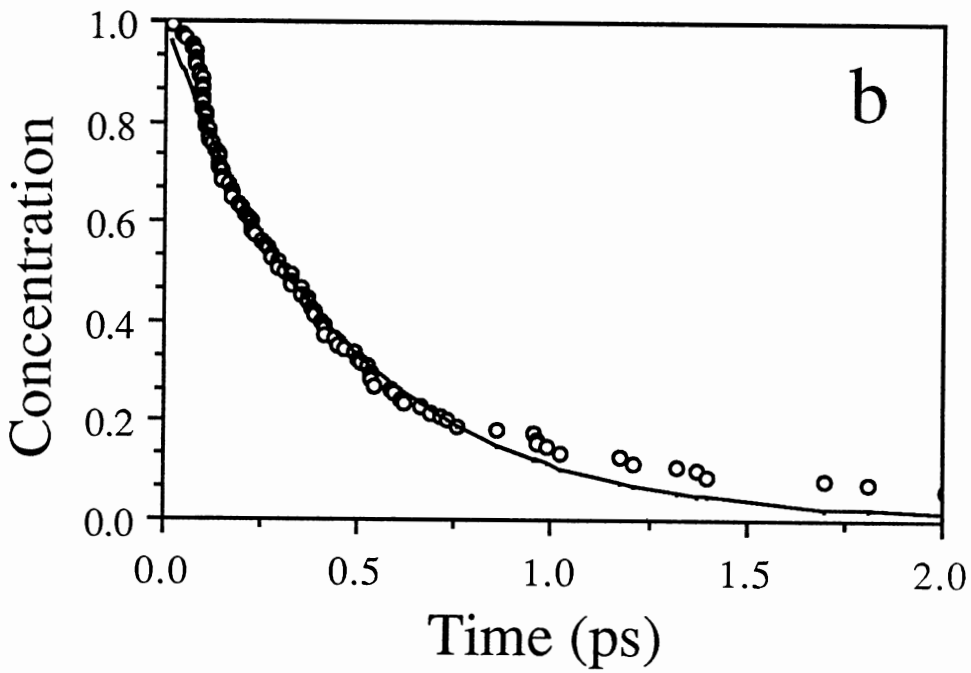
b
Concentration
1.0
0.8
0.6
0.4
0.2
0.0
0.0
0.5
1.0
1.5
2.0
Time (ps)

Figure 36. Computed Lifetime Distributions for HONO at ρ=1.50 g cm^{-3}. (a) *Cis→Trans*; (b) *Trans→Cis*..

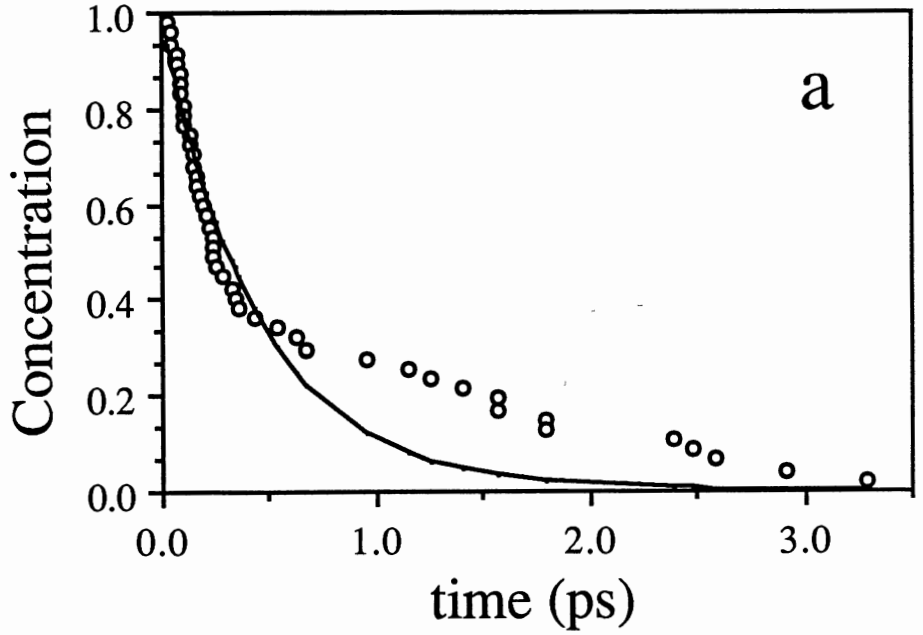
a
Concentration
1.0
0.8
0.6
0.4
0.2
0.0
0.0
1.0
2.0
3.0
time (ps)

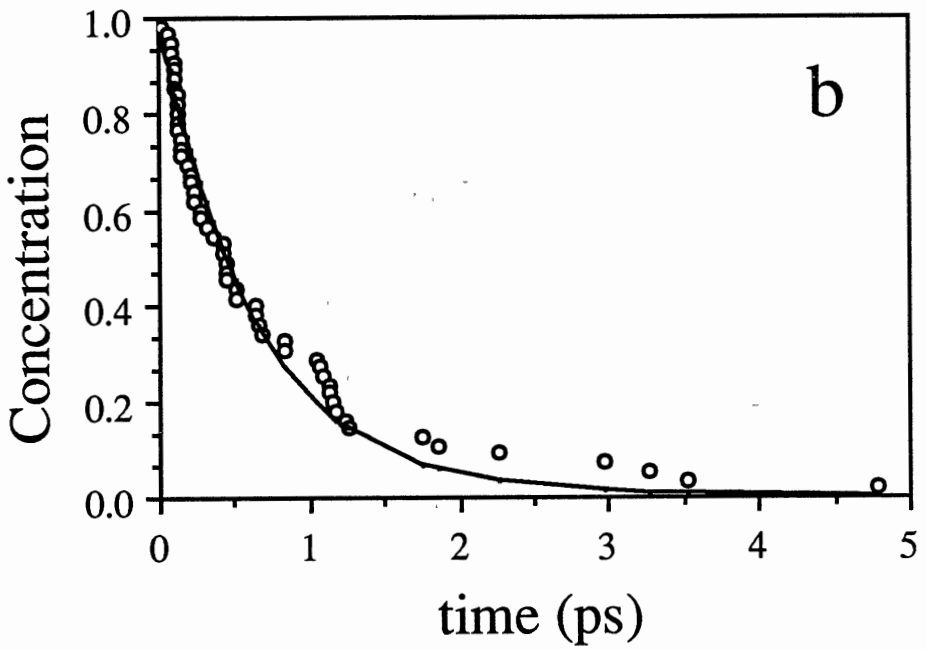
b
Concentration
1.0
0.8
0.6
0.4
0.2
0.0
0
1
2
3
4
5
time (ps)

TABLE XIX

RATE CONSTANTS FOR THE *CIS—TRANS* ISOMERIZATION OF HONO IN LIQUID ARGON

[Ar] g cm^{-3}	k (ps^{-1})	
	cis→trans	*trans→cis*
1.20	2.8 ± 0.1[a] (105)[b]	2.2 ± 0.1 (108)
1.50	2.2 ± 0.1 (47)	1.5 ± 0.1 (55)

a) The error represents the deviation from the exponential fit.
b) The numbers in parentheses are the number of lifetimes.

of lifetimes. As the results in Table XIX shows, the rate constants for both the *cis→trans* and *trans→cis* isomerization processes decrease with increasing density.

Transition-state theory rate constants To study the effects of the Ar solvent on the isomerization rate constants, we compare the rate constants obtained from the molecular dynamics simulations with those calculated using transition-state theory.

In classical transition-state theory, the rate constant is given as[106],

$$k_{TST} = (\beta h)^{-1} \frac{Q^{\dagger}}{Q} \exp[-\beta V_b] , \qquad \text{(IX.15)}$$

where $\beta = (\kappa T)^{-1}$, and κ and T are the Boltzmann constant and temperature respectively, h is plank's constant, Q and $Q^{\dagger}$ are the partition functions for the reactant and transition state geometries respectively, and V_b is the potential-energy barrier. In the classical limit[106], the vibrational partition functions are given as

$$Q = \prod_{i}^{n} \frac{\kappa T}{h\nu_i} , \qquad \text{(IX.16)}$$

where ν_i is the vibrational frequency of mode *i* in the reactant well, and

$$Q^{\dagger} = \prod_{i}^{n-1} \frac{\kappa T}{h\nu_i^{\dagger}} , \qquad \text{(IX.17)}$$

where $\nu_i^{\dagger}$ is the vibrational frequency of mode *i* in the transition-state structure. The partition function for the transition-state structure, $Q^{\dagger}$, includes all the degrees of freedom of the transition state structure except the reaction coordinate. The motion along the reaction coordinate is considered separately and its partition function included the factor $(\beta h)^{-1}$ in Eq. IX.15. The translational partition functions for the reactant and transition-state structure cancel since the mass of the molecule remains constant. If the geometry of

the transition state and reactant geometries are very different, the external rotational contribution to Q and $Q^{\dagger}$ might not cancel and the rate constant is multiplied by a factor[106]

$$\frac{I_A^{\dagger} I_B^{\dagger} I_C^{\dagger}}{I_A I_B I_C}, \qquad \text{(IX.18)}$$

where the I_A, I_B, and I_C and $I_A^{\dagger}$, $I_B^{\dagger}$, and $I_C^{\dagger}$ are the principle moments of inertia for the reactant and transition-state structures. For HONO, the ratio of the moments of inertia between the transition state and the *cis* isomer is 0.9 while that for the transition state and *trans* isomer is 1.1. The different parameters for the *cis* and *trans* isomers needed for Eq. IX.15 are listed in Table XX. The transition-theory rate constants have been multiplied by a factor of two to account for the periodicity of the potential-energy function, i.e., HONO can isomerize in both directions. The values of the transition-state theory rate constants are listed in Table XX. The rate constants obtained from the molecular dynamics simulations at ρ=1.20 g cm^{-3} are in good agreement with those calculated using transition-state theory. This suggest that the solvent plays a minor role in the barrier crossing dynamics for HONO at low density. The rate constants obtained from the molecular dynamics simulation at ρ=1.50 g cm^{-3} are somewhat smaller than those calculated using transition-state theory. Thus, at the higher density, the results suggest that solvent are important in the barrier crossing process. There are two possibilities for the deviation between the rate constants obtained from the molecular dynamics simulations and those calculated using transition-state theory: the solvent contribution to the potential of mean force increases with increasing density, thus, increasing the activation free-energy (equilibrium effect; see Eq. III.1) or the frequent collisions between HONO and the solvent during the barrier crossing process results in barrier recrossings (dynamical effect). The cause of the deviation between the rate constants obtained from the molecular dynamics simulations and those calculated from transition-state theory requires further study.

TABLE XX

TRANSITION-STATE THEORY RATE CONSTANTS FOR THE *CIS—TRANS* ISOMERIZATION OF HONO.

	$\frac{Q^{\dagger}}{Q}$ (ps^{-1})[a]	V_b(kcal mol^{-1})	k_{TST} (ps^{-1})
cis→trans	5.77	0.784	3.08
trans→cis	4.69	0.841	2.28

a) See text for definition.

Dynamical Structure

The internal flexibility of HONO during the isomerization process is studied. The average value of the internal coordinates during the molecular dynamics simulation are calculated as a function of the reaction coordinate. The results are shown in Figs. 37-38. The average bond lengths along the reaction coordinate are almost identical to their corresponding equilibrium values at both densities studied; ρ=1.20 g cm^{-3} (Fig. 37a) and ρ=1.50 g cm^{-3} (Fig. 38a). Also, the average value of the bending angles remain very close to their equilibrium values along the reaction coordinate; ρ=1.20 g cm^{-3} (Fig. 37b) and ρ=1.50 g cm^{-3} (Fig. 38b). The small fluctuations around τ=90° are probably statistical error due to the small sample sizes in the transition-state region. The "equilibrium" values of the internal coordinate change as a function of the torsional angle (Eq. IX.7), thus, the difference between the average value for the internal coordinate for the *cis* and *trans* conformations.

The root mean square (rms) deviation for the bending angles as a function of the reaction coordinate are shown in Fig. 39a and 39b for ρ=1.20 g cm^{-3} and ρ=1.50 g cm^{-3}, respectively. The increase in the fluctuations of the ONO and HON bending angles at ρ=1.20 g cm^{-3} (Fig. 39a) is probably due to the decrease in the bending force constant for the *trans* isomer compared with the *cis* isomer. The rms deviations for the ONO and HON angles at ρ=1.50 g cm^{-3} (Fig. 39b) are larger than the corresponding rms deviations at ρ=1.20 g cm^{-3} (Fig. 39a). At the higher density, the fluctuation for the two bending angles for *cis*-HONO are equal to the fluctuations for the corresponding bending angles for *trans*-HONO. The largest increase is in the HON bending angle.

The results show the average internal coordinates remain close to their equilibrium values along the reaction coordinate (Figs. 37-38) at both densities studied, but the flexibility of the internal coordinates, especially the bending angles, increases with increasing density. The largest increase is observed for the HON bending angle. Thus, at the high solvent density, flexibility seems to be important but for a quantitative study,

Figure 37. Mean Value of the Internal Coordinates as a function of the Reaction Coordinate at ρ=1.20 g cm^{-3}. (a) The different bonds are represented as follows: (triangles) O-N, (circles) N=O, and (squares) O-H; (b) the different angles are represented as follows: (empty circles) ONO, and (filled circles) HON.

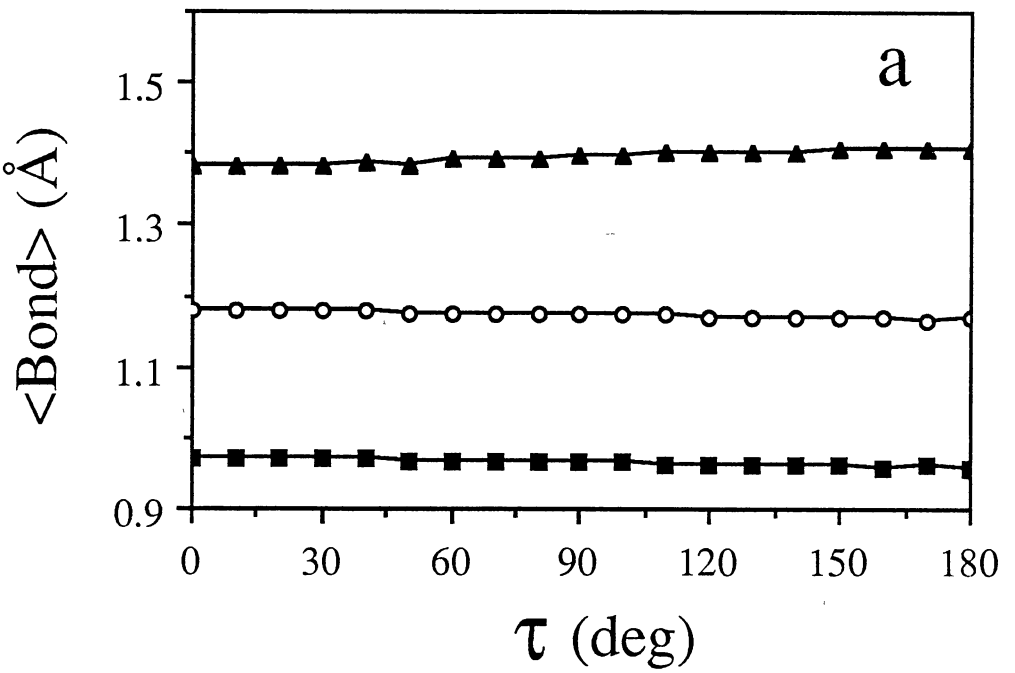
a
<Bond> (Å)
1.5
1.3
1.1
0.9
0
30
60
90
120
150
180
τ (deg)

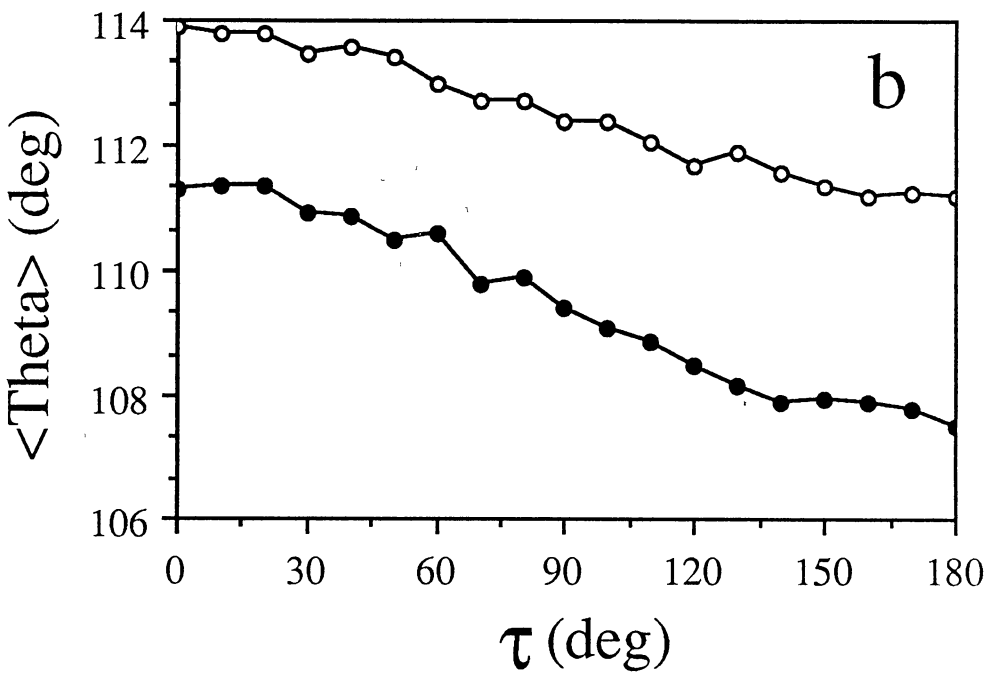
b
<Theta> (deg)
114
112
110
108
106
0
30
60
90
120
150
180
τ (deg)

Figure 38. Mean Value of the Internal Coordinates as a function of the Reaction Coordinate at ρ=1.50 g cm^{-3}. (a) The different bonds are bepresented as follows: (triangles) O-N, (circles) N=O, and (squares) O-H; (b) the different angles are represented as: (empty circles) ONO, and (filled circles) HON.

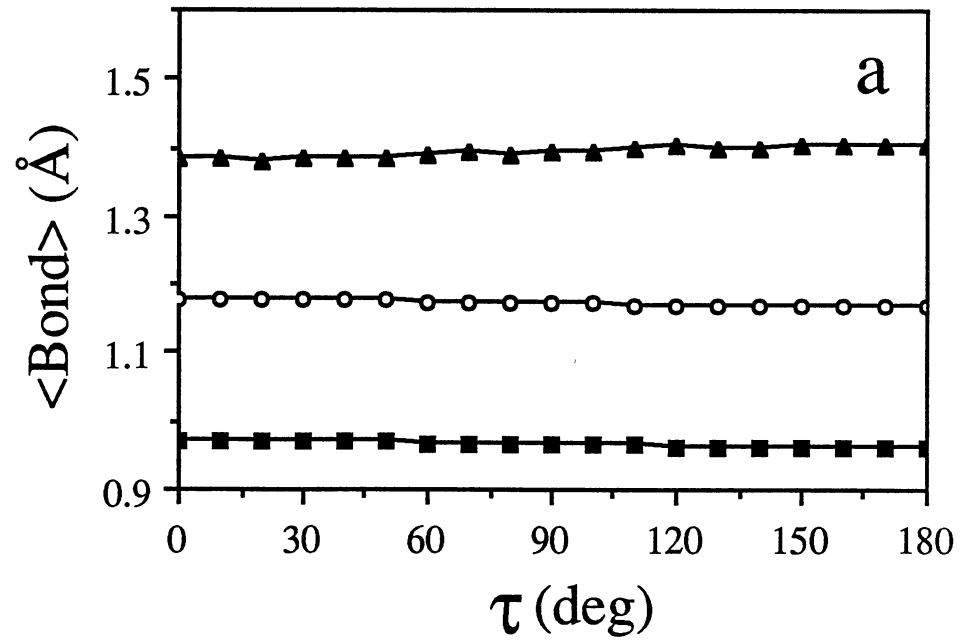
a
<Bond> (Å)
1.5
1.3
1.1
0.9
0
30
60
90
120
150
180
τ (deg)

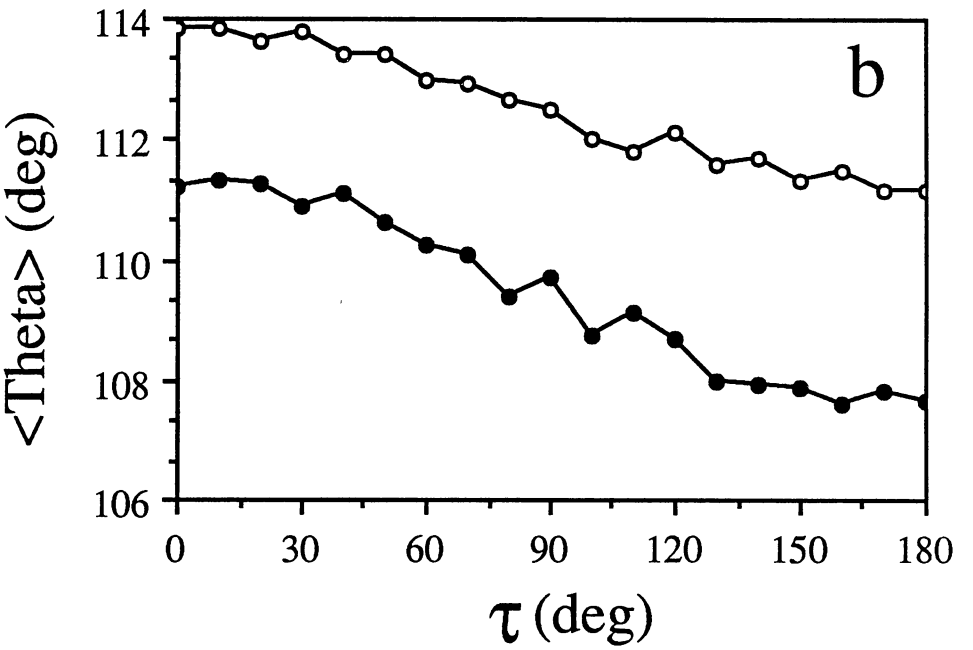
b
<Theta> (deg)
114
112
110
108
106
0
30
60
90
120
150
180
τ (deg)

Figure 39. Root Mean Square Deviation for the Bending Angles of HONO as a Function of the Reaction Coordiante. (a) ρ=1.20 g cm^{-3}; (b) ρ=1.50 g cm^{-3}. The angles are represented as follows: (empty circles) ONO angle, and (filled circles) HON angle.

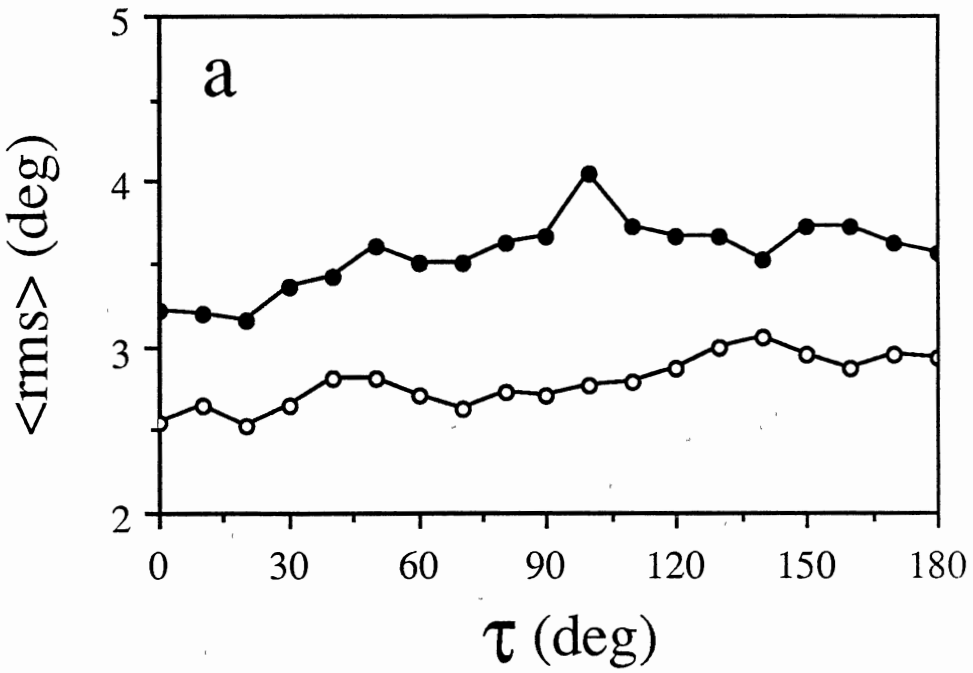
a
<rms> (deg)
5
4
3
2
0
30
60
90
120
150
180
τ (deg)

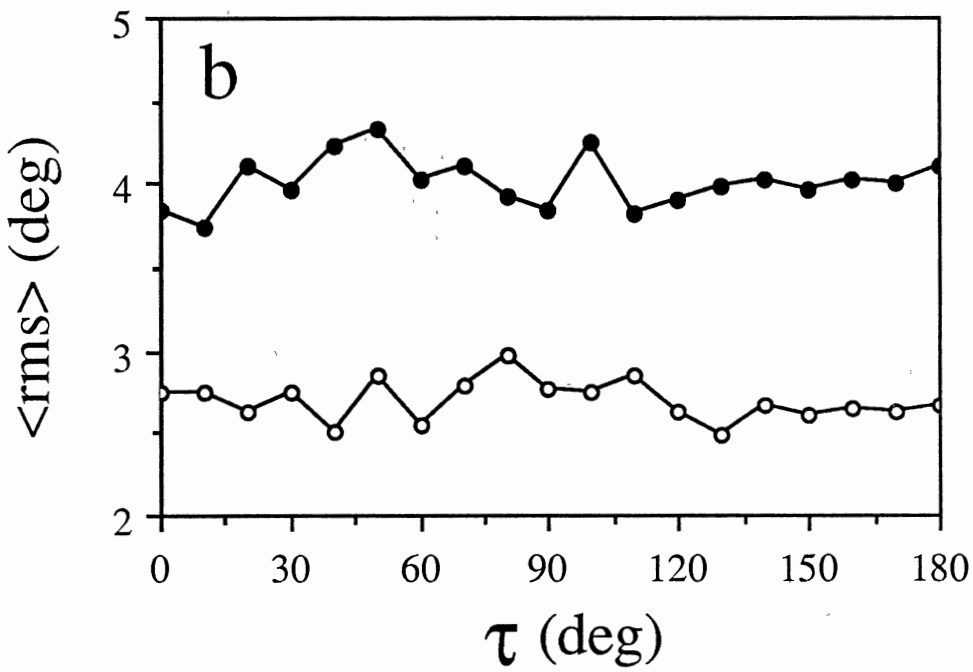
b
<rms> (deg)
5
4
3
2
0
30
60
90
120
150
180
τ (deg)

molecular dynamics simulations for HONO with constraints imposed on the internal coordinates should be performed.

Conclusions

We have performed a molecular dynamics simulation of the *cis—trans* isomerization of HONO in a liquid at two different densities employing a model potential-energy surface which incorporates internal flexibility and non-linear coupling[103]. At both densities studied, the configurational distributions are modeled well by the Boltzmann distribution. The rate constants for the *cis→trans* and *trans→cis* isomerization obtained from the molecular dynamics simulations are compared with those calculated using transition-state theory. The rate constants obtained from the molecular dynamics simulations at ρ=1.20 g cm^{-3} are in good agreement, while the rate constants at ρ=1.50 g cm^{-3} are too small. These results suggest that at the higher density, the solvent can affect the barrier crossing process. It is not clear whether the deviation from transition-state theory is due to equilibrium effects (increasing activation free-energy with increasing density) or dynamical effects (solvent induced recrossing of the barrier). Further study concerning this point is needed.

The flexibility of the internal coordinates was studied at the two different densities. The average values of the internal coordinates are all close to their equilibrium values along the reaction coordinate, but as the density increases, the rms deviation for the bending angles increases. The HON bending angle undergoes the largest fluctuations at both densities, but exhibits a marked increase in flexibility at the higher density. This suggests that flexibility in the internal coordinates is important in the *cis—trans* isomerization of HONO, although for a quantitative comparison, a molecular dynamics simulation incorporating constraints for the bond stretching and angle bending coordinates for HONO needs to be performed.

CHAPTER X

CONCLUSIONS

We have used molecular dynamics simulations and Monte Carlo methods to study the conformational dynamics of hexahydro-1,3,5-trinitro-1,3,5-triazine (RDX) and nitrous acid (HONO) in the gas and condensed phases. Molecular dynamics simulations are useful for studying both equilibrium properties of a system as well as time varying properties. Also, in molecular dynamics simulations, the solvent dynamics are calculated explicitly, thus, no assumptions concerning the solute-solvent interactions are needed.

Hexahydro-1,3,5-trinitro-1,3,5-triazine

Hexahydro-1,3,5-trinitro-1,3,5-triazine (RDX) is a member of a class of high energy compounds (nitramines) and is used as a component in solid rocket fuels. It can undergo both ring inversion and pseudorotation. Little is know about RDX either experimentally or theoretically. We have constructed a potential-energy surface which employed only harmonic interactions except for the ring torsional motion. This potential-energy surface yields a free energy change for the chair→boat/twist ring inversion of 0 ± 1 kcal mol^{-1} at 300 K. Also, the activation barrier for the pseudorotation between the different boat and twist isomers was calculated to be 0.8 kcal mol^{-1}.

We also use an anharmonic potential-energy surface. This potential included Morse potentials for the bond stretching terms and explicit couplings through non-bonded interactions (Lennard-Jones potential terms). This potential-energy surface yields a free energy change for the chair→boat/twist ring inversion of about 4.0 kcal mol^{-1} at 300 K.

Studies of the effects of a Xe solvent on the conformational dynamics of RDX illustrate that the solvent has a marked effect both on the equilibrium configurational distribution and also on the chair→boat/twist ring inversion rate constant. As the solvent density increases, the equilibrium constant shifts towards the boat/twist conformation by a factor of about 4.

The density dependence of the ring inversion rate constant obeys Lindemann theory at low solvent density. As the density increases, a maximum in the rate constant is observed after which it is a decreasing function of the solvent density (Kramer's turnover). We attribute this behavior to the bulky nitro groups which must sweep out a large volume for inversion to occur. At high solvent concentrations, the ring inversion rate constant again increases as a function of the solvent concentration which we attribute to an activation volume effect. The activation volume is a measure of the volume difference between the transition-state geometry plus solvent and the chair geometry plus solvent. The excluded volume of RDX at the transition-state is much smaller than that in the chair conformation, thus allowing the solvent to "pack" more efficiently about the transition-state geometry as opposed to the chair geometry. These results are in accord with experimental results on a similar system[147] (hexahydro-1,3,5-trimethyl-1,3,5-triazine) and theoretical studies on model systems[32,41-44].

Although the results for RDX look promising, this study does not constitute a complete analysis of the conformational dynamics of RDX. This is, though, to our knowledge, the first molecular dynamics study of the conformational dynamics of RDX either in the gas or condensed phase. Thus, we are on our way a more complete understanding of RDX on a molecular level. Some calculations that might be of interest are discussed below.

Nitrous Acid

Molecular dynamics simulations of *cis—trans* isomerization of nitrous acid (HONO) in liquid Ar at two different densities were performed. HONO is among the simplest of molecules to undergo isomerization and much is know about the potential-energy surface[87-104]. To date, most studies of barrier crossing processes have employed model potential-energy surfaces. In this study, a realistic potential-energy surface is employed which included bond stretching and angle bending potential terms and nonlinear couping between the internal coordinates and the reaction coordinate.

The results show that the solvent has little effect on the equilibrium configurational distribution which are modeled well by the Boltzmann distribution over the intramolecular energy of the gas-phase HONO.

The Ar liquid influences the rate of isomerization in HONO. The rate constants obtained from the molecular dynamics simulations for the *cis→trans* and *trans→cis* isomerization processes are compared with rate constants calculated using transition-state theory. At the lower density (ρ=1.20 g cm^{-3}), the rate constants obtained from the molecular dynamics simulations are in good agreement with those calculated using transition-state theory. At the higher density (ρ=1.50 g cm^{-3}), the rate constants obtained from the molecular dynamics simulations are smaller than those calculated using transition-state theory.

The internal flexibility of HONO increases as the density increases. The largest effect is on the HON bending angle. Thus, for HONO, it appears that internal flexibility is important. This is in accord with theoretical studies which suggest that flexible bonds and angle could influence the dynamics of barrier crossing[20,45-48].

Future Calculations

Some future calculations that could be useful for RDX would be to develop a model potential-energy surface in which the methylene (CH_2) groups were treated as

united atoms, i.e., a single atom of mass 14. This would reduce the number of atoms that are integrated and the step size for the integration could be increased by almost a factor of 2 since the high frequency CH stretches would be absent.

Also, it would be interesting (and of some value) to perform a study in which the gas-phase reaction dynamics calculation by Sewell and Thompson[78] is extended to the solvent phase, thus determining the effects of a solvent environment on the reaction dynamics. If a Xe solvent is employed (it has been suggested that RDX is soluble in Xe), the possibility of comparison between experiment and theory exists.

Two studies that would be very useful for HONO are: i) perform molecular dynamics simulations of HONO with constraints imposed on the bond stretching and angle bending coordinates; and ii) a more thorough analysis of the effects of the solvent on the isomerization, i.e., is the decrease in the rate of isomerization with increasing density an equilibrium effect (increasing activation free energy with increasing density) or a dynamical effect (solvent induces recrossings)?

The study of HONO with constraints imposed on the internal coordinates would be useful since neither HONO or model systems resembling HONO have been studied. This calculation would give a quantitative comparison of the effects of constraining the internal coordinates on the barrier crossing process for HONO.

BIBLIOGRAPHY

1. M. P. Allen and D. J. Tildesley, *Computer Simlation of Liquids*, Clarendon Press, Oxford (1987).

2. D. Chandler, *Introduction to Modern Statistical Mechanics*, Oxford University Press, NY, (1987).

3. D. W. Heermann, *Computer Simulation Methods in Theoretical Physics*, Springer-Verlag, NY, (1986).

4. M. L. Klein, Ann. Rev. Phys. Chem., 36, 525 (1985).

5. D. Fincham and D. M. Heyes, Adv. Chem. Phys., 63, 493 (1986).

6. B. J. Alder and T. E. Wainwright, J. Chem. Phys., 33, 1439 (1960).

7. A. Rahman, Phys. Rev. A, 136, 405 (1964); *ibid*, J. Chem. Phys., 45, 2585 (1966).

8. L. Verlet, Phys. Rev., 159, 98 (1967).

9. J. A. McCammon and S. C. Harvey, *Dynamics of proteins and Nucleic Acids*, University Press, Cambridge (1987).

10. J. A. McCammon, Rep. Prog. Phys., 47, 1 (1984).

11. J. A. McCammon, B. R. Gelin, and M. Karplus, Nature, 267, 585 (1977).

12. M. Karplus and J. A. McCammon, Nature, 277, 578 (1979).

13. B. Mao, M. R. Pear, J. A. McCammon, and S. H. Northrup, Biopolymers, 21, 1979 (1982).

14. R. M. Levy, R. P. Sheridan, J. W. Keepers, G. S. Dubey, S. Swaminathan, and M. Karplus, J. Biophys., 48, 509 (1985).

15. J. Kuriyan, G. A. Petsko, R. M. Levy, and M. Karplus, J. Mol. Biol., 190, 227 (1986).

16. C. B. Post, B. R. Brooks, M. Karplus, C. M. Dobson, P. J. Artymiuk, J. C. Cheetham, and D. C. Phillips, J. Mol. Biology, 190, 455 (1986).

17. S. C. Harvey, M. Prabhakaran, and J. A. McCammon, Biopolymers, 24, 1169 (1985).

18. M. Prabhakaran and S. C. Harvey, Biopolymers, 26, 1087 (1987).

19. W. F. van Gunsteren and M. Karplus, Biochemistry, 21, 2159 (1982).

20. W. F. van Gunsteren and M. Karplus, Macromolecules, 15, 1528 (1982).

21. P. J. Rossky and M. Karplus, J. Am. Chem. Soc., 101, 1913 (1979).

22. J. W. Brady, J. Am. Chem. Soc., 108, 8153 (1986).

23. J. W. Brady, Carbohydrate Research, 165, 306 (1987).

24. S. N. Ha, A. Giammona, M. Field, and J. W. Brady, Carbohydrate Resarch, 180, 207 (1988).

25. S. N. Ha, L. J. Madsen, and J. W. Brady, Biopolymers, 27, 1927 (1988).

26. J. W. Brady, J. Am. Chem. Soc., 111, 5155 (1989).

27. D. W. Noid, B. G. Sumpter, and B. Wunderlich, Macromolecules, 23, 664 (1990).

28. (a) B. G. Sumpter, D. W. Noid, and B. Wunderlich, J. Chem. Phys., 93, 6875 (1990); (b) D. W. Noid, B. G. Sumpter, and B. Wunderlich, Polymers Comm., 31, 304 (1990).

29. B. G. Sumpter, D. W. Noid, and B. Wunderlich, Polymers, 31, 1254 (1990).

30. (a) D. W. Noid and G. A. Pfeffer, J. Poly. Sci. B, 27, 2321 (1989); (b) B. G. Sumpter, D. W. Noid, and B. Wunderlich, J. Chem. Phys., 93, 6875 (1990); (c) R. Roy, B. G. Sumpter, D. W. Noid, and B. Wunderlich, J. Phys. Chem., 94, 5720 (1990); (d) B. G. Sumpter, G. A. Voth, D. W. Noid, and B. Wunderlich, J. Chem. Phys., 93, 6081 (1990); (e) B. G. Sumpter, D. W. Noid, B. Wunderlich, and S. Z. D. Cheng, Macromolecules, 23, 4671 (1990).

31. D. W. Noid, B. G. Sumpter, and B. Wunderlich, Anal. Chim. Acta., 235, 143 (1990).

32. D. W. Robertus, B. J. Berne, and D. Chandler, J. Chem. Phys., 70, 3395 (1979).

33. J. P. Bergsma, J. R. Reimers, K. R. Wilson, and J. T. Hynes, J. Chem. Phys., 85, 5625 (1986); *ibid*, 86, 1356 (1987).

34. J. P. Bergsma, P. M. Edelsten, B. J. Gertner, K. R. Huber, J. R. Reimers, K. R. Wilson, S. M. Wu, and J. T. Hynes, Chem. Phys. Lett., 123, 394 (1986).

35. I. Benjamer, B. J. Gerner, N. J. Tang, and K. R. Wilson, J. Am., Chem. Soc., 112, 524 (1990).

36. (a) K. R. Wilson, *Chemical Reactivity in Liquids*, ed. M. Moreau and P. Turq, Plenum Press, New York (1988); (b) Y. S. Li and K. R. Wilson, J. Chem. Phys., 93, 8821 (1990).

37. B. J. Gertner, K. R. Wilson, D. A. Zichi, S. Lee, and J. T. Hynes, Faraday Discuss. Chem. Soc., 85, 297 (1988).

38. D. Borgis and J. T. Hynes, J. Chem. Phys., 95, 3619 (1991).

39. D. Chandler and R. A. Kuharski, Faraday Discuss. Chem. Soc., 85, 329 (1988).

40. M. A. Wilson and D. Chandler, Chem. Phys., 149, 11 (1990).

41. D. Statman and G. W. Robinson, J. Chem. Phys., 83, 655 (1985).

42. (a) S. B. Zhu, J. Lee, and G. W. Robinson, J. Phys. Chem., 92, 2401 (1988); (b) *ibid*, J. Chem. Phys., 88, 7088 (1988).

43. (a) S. B. Zhu and G. W. Robinson, J. Phys. Chem., 93, 164 (1989); (b) *ibid*, 95, 2967 (1991); (c) *ibid*, Proc. International Supercomputing Inst., 1, 300 (1988).

44. J. E. Straub, M. Borkovec, and B. J. Berne, J. Chem. Phys., 89, 4833 (1988).

45. E. Helfand, Z. R. Wasserman, T. A. Weber, J. Skolnick, and J. H. Runnels, J. Chem. Phys., 75, 4441 (1981).

46. M. Fixman, J. Chem. Phys., 69, 1527 (1978); *ibid*, 69, 1538 (1978).

47. L. G. Dunfield and S. G. Whittington, J. Chem. Soc. Perkins Trans., 2, 654 (1977).

48. N. V. Joshi and V. S. Rao, Biopolymers, 18, 2993 (1979).

49. M. A. Schroeder, Proceedings of the 23rd JANNAF Combustion Meeting, CPIA Publication 457, Vol. II, pp.43-51, October 1984; and references therein.

50. R. J. Bahrens, Phys. Chem., 94, 6706 (1990).

51. R. Behrens and S. Bulusu, J. Phys. Chem., 95, 5838 (1990).

52. J. D. Cosgrove and A. J. Owens, Combustion and Flames, 22, 13 (1974); *ibid*, 22, 19 (1974).

53. F. J. Owens and J. Sharma, J. Appl. Phys., 51, 1494 (1980).

54. F. J. Owens and Z. Iqbal, J. Chem. Phys., 74, 4242 (1981).

55. J. C. Hoffsommer and D. J. Glover, Combustion and Flames, 59, 303 (1985).

56. S. Bulusu, D. I. Weinstein, J. R. Autera, and R. W. Velicky, J. Phys. Chem., 90, 4121 (1986).

57. X. Zhao, E. J. Hintsa, and Y. T. Lee, J. Chem. Phys., 88, 801 (1988).

58. W. C. McCrone, Anal. Chem., 22, 954 (1950).

59. C. S. Choi and E. Prince, Acta Cryst., B28, 2857 (1972).

60. I. F. Shishkov, L. V. Vilkov, M. Kolonits, and B. Rozsondai, Struct. Chem., 2, 57 (1991).

61. T. M. Haller, T. B. Brill, and A. L. Rheingold, Acta Cryst., C40, 517 (1984).

62. M. Rey-Lefon, C. Trinquecoste, R. Cavagnat, and M. T. Forel, J. Chim. Phys., 68, 1533 (1971).

63. M. Rey-Lefon, R. Cavagnat, C. Trinquecoste, and M. T. Forel, J. Chim. Phys., 68, 1573 (1971).

64. P. C. Trinquecoste, M. Rey-Lefone, and M. T. Forel, J. Chim. Phys., 72, 689 (1975).

65. R. J. Karpowicz, and T. B. Brill, J. Phys. Chem., 88, 348 (1984); *ibid*, 87, 2109 (1983).

66. Z. Iqbal, K. Suryanarayanan, S. Bulusu, and J. R. Autera, Techical report 4401, Picatinny Arsenal, Dover, NJ, Oct 1972.

67. J. M. Lehn, F. C. Riddell, B. J. Price, and J. O. Sutherland, J. Chem. Soc. (B), 387 (1967).

68. M. V. George and V. F. Wright, J. Amer. Chem. Soc., 80, 1200 (1958).

69. A. Weisbecker and A. M. Rouquie, C. R. Acad. Sci. Ser. C, 270, 572 (1970).

70. K. Calderbank and R. K. Pierens, J. Chem. Soc. Perkin Trans., 2, 869 (1979).

71. A. M. Rouquie, A. Weisbecker, and G. Richoux, J. Chim. Phys. Physicochim. Biol., 69,910 (1971).

72. *Numerical Approaches to Combustion Modeling*, Vol. 135, ed. E. S. Oran and J. P. Boris, American Institute of Aeronautics and Astronautics, Inc., Washington, DC (1991); and references therein.

73. J. J. Batten, Inter. J. Chem. Kinetics, 17, 1085 (1985); *ibid*, Aust. J. Chem., 24, 945 (1971).

74. C. F. Melius and J. S. Binkley, *Twenty-first Symposium (International) on Combustion/ The Combustion Institute,* p. 1953, (1986).

75. B. G. Sumpter and D. L. Thompson, J. Chem. Phys., 88, 6889 (1988).

76. A. Preiskorn and D. L. Thompson, J. Chem. Phys., 91, 2299 (1989)

77. B. M. Rice and D. L. Thompson, J. Chem. Phys., 93, 7986 (1990).

78. T. D. Sewell and D. L. Thompson, J. Phys. Chem. (1990).

79. M. K. Orloff, P. A. Mullen, and F. C. Rauch, J. Phys. Chem., 74, 2189 (1970).

80. A. Filhol , C. Clement, M. T. Forel, J. Paviot, M. Rey-Lefon, G. Richoux, C. Trinquecoste, and J. Cherville, J. Phys. Chem., 75, 2056 (1971).

81. P. Politzer, N. Sukumar, K. Jayasuriya, and S. Ranganathan, J. Am. Chem. Soc., 110, 3425 (1988).

82. J. S. Murray, P. C. Redfern, P. Lane, P. Politzer, and R. L. Willer, J. Mol. Struct. (Theochem), 207, 177 (1990).

83. T. Vladimiroff, (private communication).

84. U. Burkert and N. L. Allinger, In *Molecular Mechanics*; ACS, Washington, DC (1982).

85. J. M. Rosen and C. Dickinson, J. Chem. Eng. Data, 14, 120 (1969).

86. D. R. Stull, E. F. Westrum, and G. C. Sinke, *The Chemical Thermodynamics of Organic Compounds*, Wiley, N.Y. (1969).

87. G. E. McGraw, D. L. Bernitt, and I. C. Hisatsune, J. Chem. Phys. 45, 1392 (1966); *ibid*, J. Am. Chem. Soc., 92, 775 (1970).

88. P. A. Cox, A. H. Brittain, and D. J. Finnigan, Trans. Faraday Soc., 67, 2179 (1971).

89. D. J. Finnigan, P. A. Cox, and A. H. Brittain, J. Chem. Soc. Faraday Trans. 2, 68, 548 (1972).

90. R. Varma and R. F. Curl, J. Phys. Chem., 80, 402 (1976).

91. M. Allegrini, J. W. Johns, A. R. McKellar, and P. Pinson, J. Mol. Struct., 79, 446 (1980).

92. C. M. Deeley and I. M. Mills, J. Mol. Struct., 100, 199 (1983).

93. A. G. Maki and R. L. Sams, J. Mol. Struct., 100, 215 (1983); *ibid*, Mol. Phys., 54, 23 (1985).

94. S. Shaarup and J. E. Boggs, J. Mol. Struct., 30, 389 (1976).

95. P. Benioff, G. Das, and A. C. Wahl, J. Chem. Phys., 64, 710 (1976).

96. C. Larrieu, A. Dargelos, and M. Chaillet, Chem. Phys. Lett., 91, 465 (1982).

97. D. A. Kleier and M. A. Lipton, THEOCHEM, 109, 39 (1984).

98. J. G. Contreras and G. V. Sequel, THEOCHEM, 121, 137 (1985).

99. J. Murto, R. Markku, A. Aspiala, and T. Lotta, THEOCHEM, 122, 213 (1985).

100. A. G. Turner, J. Phys. Chem., 89, 4480 (1985).

101. J. A. Darsey and D. L. Thompson, J. Phys. Chem., 91, 3168 (1987).

102. Y. Guan, G. C. Lynch, and D. L. Thompson, J. Chem. Phys., 87, 6957 (1987).

103. Y. Guan and D. L. Thompson, Chem. Phys., 139, 147 (1989).

104. J. M. Coffin and P. Pulay, J. Phys. Chem., 95, 118 (1991).

105. S. Glasstone, K. J. Laidler, and H. Eyring, *The Theory of Rate Processes*, McGraw-Hill, New York (1941).

106. P. J. Robinson and K. A. Holbrook, *Unimolecular Reactions*, Wiley, London (1972).

107. W. Forst, *Theory of Unimolecular Reactions*, Academic Press, New York (1973).

108. R. van Eldik and J. Jonas, Ed., *High Pressure Chemistry and Biochemistry*, D. Reidel: Boston, MA (1987).

109. J. T. Hynes, *Theory of Chemical Reactions in Solution*, Ed. M. Baer, CRC Press, Boca Raton, FL (1985).

110. J. T. Hynes, Ann. Rev. Phys. Chem., 36, 573 (1985).

111. J. T. Hynes, J. Stat. Phys., 42, 149 (1986).

112. B. J. Berne, M. Borkovec, and J. E. Straub, J. Phys. Chem., 92, 3711 (1988).

113. J. Schroeder and J. Troe, Ann. Rev. Phys. Chem., 38, 163 (1987); (b) *ibid*, Chem. Phys. Lett., 116, 453 (1985).

114. H. A. Kramers, Physica, 7, 284 (1940).

115. R. F. Grote and J. T. Hynes, J. Chem. Phys., 74, 4465 (1981).

116. G. van der Zwan and J. T. Hynes, J. Chem. Phys., 77, 1295 (1982).

117. R. F. Grote and J. T. Hynes, J. Chem. Phys., 75, 2191 (1981); *ibid*, 73, 2715 (1980).

118. (a) T. Xiang, F. Liu, and D. M. Grant, J. Chem. Phys., 94, 4463 (1991); (b) S. A. Adelman and R. Muralidhar, J. Chem. Phys., 95, 2752 (1991); and reference therein.

119. D. A. McQuarrie, *Statistical Mechanics*, Harper and Row, New York (1973).

120. R. J Ouellette and S. H. Williams, J. Am. Chem. Soc., 93, 466 (1971).

121. B. M. Ladanyi and J. T. Hynes, J. Am. Chem. Soc., 108, 585 (1986).

122. (a) D. Bohm and E. P. Gross, Phys. Rev., 75, 1864, (1949); (b) P. L. Bhatnagar, E. P. Gross, and M. Krook, Phys. Rev., 94, 511 (1954).

123. D. Chandler, *Stochastic Molecular Dynamics*, NRCC Proceedings No. 6, ed. D. Ceperley and J. Tully, USDOE and NSF, Washington, DC (1971).

124. R. A. Kuharski, D. Chandler, J. A. Montgomery, F. Rabii, and S. J. Singer, J. Phys. Chem., 92, 3261 (1988).

125. D. Chandler, J. Stat. Phys., 42, 49 (1986).

126. F. H. Stillinger and A. Rahman, J. Chem. Phys., 60, 1545 (1974); *ibid*, 57, 1281 (1972).

127. S. H. Fleischman and C. L. Brooks, III, J. Chem. Phys., 87, 3029 (1987).

128. D. Chandler and L. R. Pratt, J. Chem. Phys., 65, 2925 (1976).

129. D. Chandler, J. Chem. Phys., 68, 2959 (1978).

130. L. R. Pratt, C. S. Hsu, and D. Chandler, J. Chem. Phys., 68, 4202 (1978).

131. C. S. Hsu, L. R. Pratt, and D. Chandler, J. Chem. Phys., 4213 (1978).

132. D. A. Cates and R. A. MacPhail, J. Phys. Chem., 95, 2209 (1991).

133. S. P. Velsko, D. H. Waldeck, and G. R. Fleming, J. Chem. Phys., 78, 249 (1983).

134. S. P. Velsko and G. R. Fleming, Chem. Phys., 65, 59 (1982).

135. S. P. Velsko and G. R. Fleming, J. Chem. Phys., 76, 3553 (1982).

136. G. Rothenberger, D. K. Negus, and R. M. Hochstrasser, J. Chem. Phys., 79, 5360 (1983).

137. D. P. Millar and K. B. Eisenthal, J. Chem. Phys., 83, 5076 (1985).

138. S. R. Flom, A. M. Brearley, M. A. Kahlow, V. Nagarajan, and P. F. Barbara, J. Chem. Phys., 83, 1993 (1985).

139. D. L. Hasha, T. Eguchi, and J. Jonas, J. Am. Chem. Soc., 104, 2290 (1982); *ibid*, J. Chem. Phys., 75, 1571 (1981).

140. B. D. Ross and N. S. True, J. Am. Chem. Soc., 105, 1382 (1983); *ibid*, 4871 (1983).

141. C. A. Spring and N. S. True, J. Am. Chem. Soc., 105, 7231 (1983).

142. J. P. Chauvel, C. B. Conboy, W. M. Chew, G. B. Matson, C. A. Spring, B. D. Ross, and N. S. True, J. Chem. Phys., 80, 1469 (1984).

143. J. P. Chauvel and N. S. True, J. Chem. Phys., 80, 3561 (1984).

144. S. H. Bauer and N. S. True, J. Phys. Chem., 84, 2507 (1980).

145. P. Chu and N. S. True, J. Phys. Chem., 89, 2625 (1985).

146. J. Chu and N. S. True, J. Phys. Chem., 89, 5613 (1985).

147. C. B. LeMaster, C. L. LeMaster, M. Tafazzoli, C. Suarez, and N. S. True, J. Phys. Chem., 92, 5933 (1988).

148. C. B. LeMaster, C. L. LeMaster, C. Suarez, M. Tafazzoli, and N. S. True, J. Phys. Chem., 93, 3993 (1989).

149. C. B. LeMaster, C. L. LeMaster, M. Tafazzoli, C. Suarez, and N. S. True, J. Phys. Chem., 94, 3461 (1990).

150. L. M. Jackman, Ed. F. A. Cotton, *Dynamic NMR Spectroscopy*, Academic Press: New York, 1975.

151. H. S. Gutowsky and P. A. Temussi, J. Am. Chem. Soc., 89, 4358 (1967).

152. H. M. Pickett and H. L. Strauss, J. Am. Chem. Soc., 92, 7281 (1970).

153. A. Nitzan, J. Chem. Phys., 82, 1614 (1985); *ibid*, 86, 2734 (1987).

154. B. Carmeli and A. Nitzan, Phys. Rev. Lett., 49, 423 (1982).

155. (a) P. J. Flory, J. Chem. Phys., 10, 51 (1942); (b) P. J. Flory, *Statistical Mechanics of Chain Molecules*, Wiley, New York (1969).

156. A. J. Marks, J. N. Murrell, and A. J. Stace, J. Chem. Phys., 94, 3908 (1991).

157. J. P. Valleau and S. G. Whittington, *Statistical Mechanics Part A. Modern Theoretical Chemistry*, ed. B. J. Berne, Plenum Press, New York (1977).

158. N. Metropolis, A. W. Rosenbluth, M. N. Rosenbluth, A. H. Teller, and E. Teller, J. Chem. Phys., 21, 1087 (1953).

159. D. L. Bunker and B. S. Jacobsen, J. Am. Chem. Soc., 94, 1843 (1972).

160. A. J. Stace and J. N. Murrell, Mol. Phys., 33, 1 (1977).

161. J. N. Murrell, A. J. Stace, and R. Dammel, J. Chem. Soc. Faraday Trans.II, 74, 1532 (1978).

162. A. J. Stace and J. N. Murrell, Int. J. Chem. Kinetics, 10, 197 (1979).

163. A. J. Marks, A. J. Stace, and J. N. Murrell, and H. Buscher, Mol. Phys., 65, 1153 (1988).

164. A. J. Stace, Chem. Phys. Lett., 55, 77 (1978); *ibid*, J. Chem. Soc. Faraday Trans. II, 75, 1657 (1979); *ibid*, 77, 2105 (1981).

165. J. E. Lennard-Jones and A. F. Devonshire, Proc. R. Soc. London A, 163, 53 (1937).

166. C. L. Brooks and M. Karplus, J. Chem. Phys., 79, 6312 (1983).

167. M. Berkowitz and J. A. McCammon, Chem. Phys. Lett., 90, 215 (1982).

168. M. Born and T. Von Karman, Physik. Z., 13, 297 (1912).

169. H. Goldstein, *Classical Mechanics*, Addison-Wesley, New York (1980).

170. GenDyn is a generalized classical mechanics trajectory program developed by this lab. For details, see K. L. Bintz, Master's Thesis, Oklahoma State University, 1986.

171. H. B. Schlegal, *Ab Initio* Methods in Quantum Chemisty, 1, 249 (1987).

172. J. P. Chandler, STEPIT , QCPE, Indiana University, Bloomington, Indiana.

173. Dennis Jr., J. E.; Schnabel, R. B. *In Numerical Methods for Unconstrained Optimization and Nonlinear Equations*, Prentic Hall; New Jersey, 1983.

174. J. W. McIver, Jr., and A. Komornicki, J. Am. Chem. Soc., 94, 2625 (1972).

175. S. Profeta, Jr. and N. L. Allinger, J. Am. Chem. Soc., 107, 1907 (1985).

176. D. Cremer and J. A. Popel, J. Am. Chem. Soc., 97, 1354 (1975).

177. D. Cremer, J. Phys. Chem., 94, 5502 (1990).

178. P. W. Atkins, *Physical Chemistry*, 2nd. edition, W. H. Freeman and Co., New York (1982), pg. 869.

179. H. G. Elias, *Macromolecules*, Plenum Press, N. Y., (1984), Vol. 1, pg.96.

180. M. Karplus and J. N. Kushick, Macromolecules, 14, 325 (1981).

181. D. W. Noid and R. A Marcus, J. Chem. Phys., 67, 559 (1977).

182. R. J. Wolf and W. L. Hase, J. Chem. Phys., 73, 3779 (1980).

183. W. L. Hase and R. J. Wolf, J. Chem. Phys., 75, 3809 (1981).

184. D. W. Noid, M. L. Koszykowski, and R. A. Marcus, Ann. Rev. Phys. Chem., 32, 267 (1981).

185. T. H. Holme and J. S. Hutchinson, J. Chem. Phys., 83, 2860 (1985).

186. N. Bloembergen and A. H. Zewail, J. Phys. Chem., 88, 5459 (1984).

187. S. K. Gray, S. A. Rice, and D. W. Noid, J. Chem. Phys., 84, 3745 (1986).

188. B. G. Sumpter and D. L. Thompson, J. Chem. Phys., 86, 2805 (1987).

189. T. Uzer, B. D. McDonald, Y. Guan, and D. L. Thompson, Chem. Phys. Lett., 152, 405 (1988).

190. B. G. Sumpter, C. C. Martens, and G. S. Ezra, J. Phys. Chem., 92, 7193 (1988).

191. C. Getino, B. G. Sumpter, J. Santamaria, and G. S. Ezra, J. Phys. Chem., 93, 3877 (1989).

192. M. Quack, Ann. Rev. Phys. Chem., 41, 839 (1990).

193. T. Uzer, G. A. Natanson, and J. T. Hynes, Chem. Phys. Lett., 122, 12 (1985).

194. B. G. Sumpter and D. L. Thompson, Chem. Phys. Lett., 153, 243 (1988).

195. W. J. Hoving and R. Parson, Chem. Phys. Lett., 158, 222 (1989).

196. N. L. Allinger, Y. H. Yuh, and J. H. Lii, J. Am. Chem. Soc., 111, 8551 (1989).

197. N. L. Allinger and D. Y. Chung, J. Am. Chem. Soc., 98, 6798 (1976).

198. G. M. Torries and J. P. Valleau, Chem. Phys. Lett., 28, 578 (1974); *ibid*, J. Comput. Phys., 23, 187 (1977); *ibid*, J. Chem. Phys., 66, 1402 (1977).

199. J. P. Valleau and D. N. Card, J. Chem. Phys., 57, 5457 (1972).

200. J. P. Valleau and G. M. Torrie, *Statistical Mechanics Part A. Modern Theoretical Chemistry*, ed. B. J. Berne, Plenum Press, New York (1977).

201. L. F. Shampine and M. K. Gordon, *Computer Solutions of Ordinary Differential Equations, The Initial Value Problem*; W. H. Freeman Co., San Fransico (1975).

202. S. Chandrasekhan, Rev. Mod. Phys., 15, 1 (1943).

203. C. Getino, B. G. Sumpter, and J. Santamaria, Chem. Phys., 145, 1 (1990).

204. R. Duchovic, W. L. Hase, and B. H. Schlegal, J. Chem. Phys., 88, 1339 (1984).

205. R. J. Wolf, D. S. Bhatia, and W. L. Hase, Chem. Phys, Lett., 132, 493 (1986).

206. W. J. Lemon and W. L. Hase, J. Phys. Chem., 91, 1596 (1987).

207. B. G. Sumpter and D. L. Thompson, J. Chem. Phys, 87, 5809 (1987).

208. T. Uzer, J. T. Hynes, and W. P. Reinhardt, J. Chem. Phys., 85, 5791 (1986).

209. L. M. Raff, J. Chem. Phys., 93, 3160 (1990); *ibid*, J. Phys. Chem., 91, 3266 (1987).

APPENDIX A

PRESSURE

The ideal pressure equation,

$$PV = nRT, \tag{A.1}$$

where P is the ideal pressure, V is the volume, n is the number of moles, R is the gas constant, and T is the temperature, is normally not valid since there are interactions between the atoms which are neglected in the ideal gas equation. The forces between the atoms must be taken into account in the calculation of the pressure.

The virial theorem, in generalized equipartion form, can be written[1],

$$\left\langle A\frac{\partial H}{\partial q_k}\right\rangle = \kappa T \left\langle \frac{\partial A}{\partial q_k}\right\rangle, \tag{A.2}$$

where **H** is the Hamiltonian of the system, q_k is a qeneralize coordinate, and the $\langle\ \rangle$ represent averages over phase space. Assuming the q_k's are Cartesian coordinates, substituting them for A and summing over all the atoms, Eq.(A.2) can be written

$$\frac{1}{3}\left\langle \sum_{i=1}^{N} \mathbf{r}_i \frac{\partial \mathbf{H}}{\partial \mathbf{r}_i}\right\rangle = N\kappa T, \tag{A.3}$$

where $r_i = \sqrt{x^2+y^2+z^2}$. The total force acting on ith atom can be calculated by,

$$-\mathbf{f}_i^{tot} = \frac{\partial \mathbf{H}}{\partial \mathbf{r}_i}. \tag{A.4}$$

Substituting Eq.(A.3) into Eq.(A.2), we obtain

$$-\frac{1}{3}\left\langle \sum_{i=1}^{N} \mathbf{r}_i \cdot \mathbf{f}_i^{tot} \right\rangle = N\kappa T, \tag{A.5}$$

where $\mathbf{f}_i^{tot} = \mathbf{f}_i^{ext} + \mathbf{f}_i^{int}$. The external force is given by the pressure exerted on the system by the walls,

$$-\frac{1}{3}\left\langle \sum_{i=1}^{N} \mathbf{r}_i \cdot \mathbf{f}_i^{ext} \right\rangle = PV, \tag{A.6}$$

while the internal pressure is due to the intermolecular forces. Using Newton's third law,

$$\sum_{i=1}^{N} \mathbf{r}_i \cdot \mathbf{f}_i^{int} = \sum_{i=1}^{N} \sum_{j>i}^{N} \mathbf{r}_{ij} \cdot \mathbf{f}_{ij}^{int} = -\sum_{i=1}^{N} \sum_{j>i}^{N} r_{ij} \cdot (\nabla_{r_{ij}} V(r_{ij})), \tag{A.7}$$

where $r_{ij} = r_i - r_j$ and

$$\mathbf{f}_{ij}^{int} = -\nabla_{r_{ij}} V(r_{ij}) = \sum_{i=1}^{N} \sum_{j>1}^{N} r_{ij} \cdot \frac{\partial V}{\partial r_{ij}} . \tag{A.8}$$

Incorporating Eq. (A.6-8) into Eq. (A.5), the pressure equation can be obtained,

$$P = \frac{N\kappa T}{V} - \frac{1}{3V}\left\langle \sum_{i=1}^{N} \sum_{j>i}^{N} r_{ij} \cdot \frac{\partial V}{\partial r_{ij}} \right\rangle, \tag{A.9}$$

where the term in the angular brackets is the intermolecular pair virial.

APPENDIX B

CREMER-POPLE PUCKER COORDINATES

For many years now, it has been known that cyclic molecules can exist in many different stable conformations, but trying to quantify these different conformations has been a problem. Cremer and Pople[176-177] have derived a set of generalized pucker coordinates that can be used to describe the different conformations that exist for cyclic molecules.

Initially, the positions of N atoms are located at Cartesian coordinates (X_i, Y_i, Z_i) or position vectors $\mathbf{R}_i$ (i=1...N) where N is the number of atoms in the ring portion of the molecule. The origin can be moved to the geometrical center such that,

$$\sum_{i=1}^{N} \mathbf{R}_i = 0. \qquad \text{(B.1)}$$

It is desirable to specify the displacement of each atom from a mean plane. A new set of Cartesian coordinates (x,y,z) with respect to the molecular axis can be chosen through a linear combination of the original Cartesian coordinates, such that the origin of the new Cartesian coordinates is at the geometrical center, the z-axis is perpendicular to the mean plane, and the y-axis passes through the projection of atom 1 onto the mean plane. Using Eq. (B.1) and the requirement that the new origin be at the geometrical center, it can be shown that

$$\sum_{i=1}^{N} z_i = 0. \qquad \text{(B.2)}$$

If the conditions,

$$\sum_{i=1}^{N} z_i \cos[2\pi(i-1) / N] = 0 \qquad \text{(B.3)}$$

and

$$\sum_{i=1}^{N} z_i \sin[2\pi(i-1) / N] = 0, \qquad \text{(B.4)}$$

are imposed, then the mean plane of the molecule will be uniquely fixed.

To determine the orientation of the mean plane from the position vectors $\mathbf{R}_i$, a new set of vectors is defined by,

$$\mathbf{R}' = \sum_{i=1}^{N} \mathbf{R}_i \sin[2\pi(i-1) / N] , \qquad \text{(B.5)}$$

and

$$\mathbf{R}'' = \sum_{i=1}^{N} \mathbf{R}_i \cos[2\pi(i-1) / N] = 0. \qquad \text{(B.6)}$$

A unit vector given by

$$\hat{\mathbf{n}} = \frac{\mathbf{R}' \times \mathbf{R}''}{|\mathbf{R}' \times \mathbf{R}''|} , \qquad \text{(B.7)}$$

will be defined as the z-axis and will be perpendicular to $\mathbf{R}'$ and $\mathbf{R}''$. Therefore, the positive direction along the z-axis will define the "topside" of the mean plane. The components of $\hat{\mathbf{n}}$ with respect to the space fixed Cartesian coordinates (X_i, Y_i, Z_i) can be obtained by

$$z_i = \mathbf{R}_i \cdot \hat{\mathbf{n}} \tag{B.8}$$

which will satisfy Eq. (B.2) - (B.4).

The generalized ring-puckering coordinates are given as follows: if N is odd and N >3, then

$$q_m \cos \phi_m = \sqrt{\frac{2}{N}} \sum_{i=1}^{N} z_i \cos[2\pi m(i-1) / N] \tag{B.9}$$

and

$$q_m \sin \phi_m = -\sqrt{\frac{2}{N}} \sum_{i=1}^{N} z_i \sin[2\pi m(i-1) / N]. \tag{B.10}$$

These generalized coordinates apply for m=2,3,... (N-1)/2. The correspond to a set of puckering coordinate with amplitude q_m and phase ϕ_m, where $q_m > 0$ and $0 \leq \phi_m \leq 2\pi$. If the number of atoms in the ring is even, then Eq. (B.9) and (B.10) apply for m=2,3,...,(N/2 -1). There is a single puckering amplitude

$$q_{N/2} = \sqrt{\frac{1}{N}} \sum_{i=1}^{N} z_i \cos[2\pi m(i-1) / N] \tag{B.11.a}$$

or

$$q_{N/2} = \sqrt{\frac{1}{N}} \sum_{i=1}^{N} (-1)^{i-1} z_i. \tag{B.11.b}$$

As can be seen from Eq. (B.11.b), this puckering amplitude can be either positive or negative. Using these equations, atom 1 will always be the apex atom and there will be

N-3 ring-puckering coordinates. The normalization factors in Eq. (B.9)-(B.11) are such that,

$$\sum_{i=1}^{N} z_i^2 = \sum_{j=2}^{m} q_i^2 = Q^2, \tag{B.12}$$

where Q represents a total puckering amplitude.

For RDX, there will be three ring-puckering coordinates, an amplitude-phase pair (q_2,Φ_2) and a single puckering coordinate q_3 given by Eq. (B.9) - (B.11). These three coordinates can be transformed to a set of " spherical polar " coordinates Q, Θ, and Φ by,

$$q_2 = Q \sin\Theta, \tag{B.13}$$

$$q_3 = Q \cos\Theta \tag{B.14}$$

and

$$\tan\Theta = \frac{q_2}{q_3} \tag{B.15}$$

where Q is defined by Eq. (B.12). In this representation of the ring-puckering coordinates, $Q \geq 0$, $0 \leq \Theta \leq \pi$, and $0 \leq \Phi \leq 2\pi$.

VITA 2

Eric Paul-Joseph Wallis

Candidate for the Degree of

Doctor of Philosophy

Thesis: CLASSICAL DYNAMICS STUDIES OF CONFORMATIONAL CHANGES IN POLYATOMIC MOLECULES IN THE GAS AND CONDENSED PHASES

Major Field: Chemistry

Biographical:

Personal Data: Born in Detroit, Michigan, June 5, 1964, the son of Daniel A. and Kayra A. Wallis.

Education: Graduated from Subiaco Academy, Subiaco, Arkansas, in May 1983; received Bachelor of Science Degree in Chemistry from Arkansas Tech University, Russellville, Arkansas, in May 1987; completed requirements for Doctor of Philosophy degree at Oklahoma State University in May, 1992.

Professional Experience: President, Alpha Chi (honorary society), 1985; Inducted into Who's Who, 1986; Teaching Assistant, Department of Chemistry, Arkansas Tech University, August, 1986 to May, 1987; Teaching Assistant, Department of Chemistry, Oklahoma State University, August, 1987 to May, 1989 and August, 1991 to December, 1991; president, Phi Lambda Upsilon (honorary society for chemistry and biochemistry), 1988-1989.